High resolution far- and near-infrared absorption spectroscopy of water vapor for atmospheric applications : lines and continuum

Aleksandra Zibarova

THÈSE

Pour obtenir le grade de

DOCTEUR DE L'UNIVERSITÉ GRENOBLE ALPES

École doctorale : PHYS - Physique
Spécialité : Physique appliquée
Unité de recherche : Laboratoire Interdisciplinaire de Physique

Spectroscopie à haute résolution de la vapeur d'eau dans l'infrarouge lointain et proche pour applications atmosphériques : raies et continuum

High resolution far- and near-infrared absorption spectroscopy of water vapor for atmospheric applications: lines and continuum

Présentée par :

Aleksandra ZIBAROVA

Direction de thèse :

Alain CAMPARGUE DIRECTEUR DE RECHERCHE, CNRS DELEGATION ALPES	Directeur de thèse
Mikhail TRETYAKOV SENIOR SCIENTIST, RUSSIAN ACADEMY OF SCIENCES	Co-directeur de thèse

Rapporteurs :

JEAN VANDER AUWERA
MAITRE DE RECHERCHE, FONDS DE LA RECHERCHE SCIENTIFIQUE
HA TRAN
DIRECTRICE DE RECHERCHE, CNRS DELEGATION ILE-DE-FRANCE SUD

Thèse soutenue publiquement le **5 octobre 2023**, devant le jury composé de :

JEAN VANDER AUWERA MAITRE DE RECHERCHE, FONDS DE LA RECHERCHE SCIENTIFIQUE	Rapporteur
HA TRAN DIRECTRICE DE RECHERCHE, CNRS DELEGATION ILE-DE-FRANCE SUD	Rapporteure
LAURENCE REGALIA MAITRE DE CONFERENCES HDR, UNIVERSITE DE REIMS - CHAMPAGNE ARDENNE	Examinatrice
AMANDA ROSS DIRECTRICE DE RECHERCHE, CNRS DELEGATION RHONE AUVERGNE	Examinatrice
ANTOINE DELON PROFESSEUR DES UNIVERSITES, UNIVERSITE GRENOBLE ALPES	Président

Abstract

Water vapor is the first absorber and the main greenhouse gas in the Earth's atmosphere. The general aim of this thesis is to contribute to a better characterization of the absorption spectrum of this key species. Our approach is mostly experimental. Two aspects of light absorption by water vapor are considered: the water monomer lines and the continuum absorption. The atmospheric continuum related to water comprises self- and foreign components, which are due to the interaction of water molecules with each other or with other molecules (N_2, O_2,..), respectively.

The experimental studies were performed at room temperature in the far- and near-infrared ranges (15-720 cm^{-1} and 8040-8633 cm^{-1}) using two different spectrometers. In the far-infrared, the high-resolution spectra were acquired with a commercial Fourier transform spectrometer equipped with a mulipass White-type gas cell (151 m absorption pathlength) and using the SOLEIL synchrotron radiation. In the near-infrared range, data were acquired using a highly sensitive cavity ring down spectrometer (absorption pathlengths of several tens of km).

The first chapter of this work presents the previously developed theoretical and experimental background. It includes the basics of water monomer lines modeling, the current understanding of the continuum nature and a review of the previous experimental studies of the continuum. A general description of the spectroscopic technique used in the present work is given in the first chapter.

The second chapter is entirely devoted to accurate measurement of the positions and intensities of the water lines both in the far- and in near-infrared ranges. Line positions and intensities were determined for about 3000 lines in the far-infrared and 5400 lines in the near-infrared range. 450 of these lines in the far-infrared and about one third of the assigned transitions in the near-infrared are newly measured. The first experimental determination of 79 rovibrational levels of $H_2{}^{16}O$, $H_2{}^{18}O$, $H_2{}^{17}O$, and $HD^{16}O$ are reported on the basis of the near-infrared measurements. The wide frequency and line intensity ranges (a few 10^{-26} - 10^{-19} cm/molecule in the far-infrared and a few 10^{-30} - 10^{-22} cm/molecule in the near-infrared) allow for validation tests of the line parameters provided by the current spectroscopic databases (HITRAN2020, W2020).

The third chapter presents the results of four series of measurements of the self- and foreign-continuum of water vapor. The expected continuum pressure dependences are observed. Self- and foreign-continuum absorption cross sections are retrieved at fixed frequencies in the transparency microwindows between strong H_2O lines. The first water continuum measurements are reported in the 200-350 and 8300-8500 cm^{-1} intervals (for self-continuum) and in the 90-330 cm^{-1} interval (for foreign-continuum). The agreement of the retrieved continuum cross sections with the known experimental data is demonstrated in the far-infrared range. Also, in this range our data resulted in a significant modification of the MT_CKD model for the self-continuum (30% decrease in the region of the continuum maximum where previous experimental studies were absent). The foreign-continuum results as well as the near-infrared continuum measurements generally agree with MT_CKD. The

obtained continuum data and known results of *ab initio* water dimer spectrum calculation allow suggesting a continuum model that considers all currently known continuum components in the far-infrared range. The results obtained in the near-infrared validate in general the MT_CKD model both for the self- and foreign-continuum. However, a spectral feature unaccounted for by the model was detected near 8450 cm^{-1}. It was tentatively interpreted as a spectral signature of bound dimers of water vapor.

Résumé

La vapeur d'eau est le principal gaz à effet de serre de l'atmosphère terrestre. L'objectif de cette thèse est de contribuer à une meilleure caractérisation du spectre d'absorption de cette molécule-clé. Notre approche est essentiellement expérimentale. Deux aspects de l'absorption de la lumière par la vapeur d'eau sont étudiés : les raies des monomères de l'eau et le continuum d'absorption. Le continuum atmosphérique lié à l'eau comprend une composante propre (self continuum) due à l'interaction des molécules d'eau entre elles et une composante due à l'interaction aux autres molécules (foreign continuum).

Les spectres ont été enregistrés à température ambiante dans l'infrarouge lointain et l'infrarouge proche (15-720 cm^{-1} et 8040-8633 cm^{-1}) à l'aide de deux spectromètres. Dans l'infrarouge lointain, les spectres à haute résolution ont été acquis avec un spectromètre à transformée de Fourier commercial équipé d'une cellule de type White (longueur d'absorption de 151 m) et en utilisant le rayonnement synchrotron SOLEIL comme source. Dans le proche infrarouge, un spectromètre « cavity ring » (CRDS) très sensible a été utilisé (longueur équivalente d'absorption de l'ordre de plusieurs dizaines de km).

Le premier chapitre de ce travail présente les fondements théoriques et l'état de l'art des dispositifs expérimentaux. Il comprend les bases de la modélisation des raies des monomères de l'eau, la compréhension actuelle de la nature du continuum et l'examen des études expérimentales antérieures du continuum.

Le deuxième chapitre est consacré à la mesure précise des positions et des intensités des raies de l'eau dans les domaines de l'infrarouge lointain et de l'infrarouge proche. Environ 3000 raies ont été déterminées dans l'infrarouge lointain et 5400 raies dans l'infrarouge proche. 450 des raies dans l'infrarouge lointain et environ un tiers des transitions assignées dans l'infrarouge proche ont été nouvellement mesurées. La première détermination expérimentale de 79 niveaux rovibrationnels de $H_2{}^{16}O$, $H_2{}^{18}O$, $H_2{}^{17}O$ et $HD^{16}O$ est rapportée sur la base des mesures dans le proche infrarouge. Les larges gammes de fréquences et d'intensités de raies (quelques 10^{-26} - 10^{-19} cm/molécule dans l'infrarouge lointain et quelques 10^{-30} - 10^{-22} cm/molécule dans l'infrarouge proche) ont permis de tester les paramètres de raies fournis par les bases de données spectroscopiques actuelles (HITRAN2020, W2020).

Le troisième chapitre présente les résultats de quatre séries de mesures du self continuum et du foreign continuum de la vapeur d'eau. Les dépendances de pression du continuum attendues sont validées par les observations. Les sections efficaces d'absorption du self-continuum et du foreign continuum ont été mesurées à des fréquences fixes dans les micro-fenêtres de transparence entre les raies fortes. Les premières mesures du continuum de l'eau sont rapportées dans les intervalles 200-350 et 8300-8500 cm^{-1} (pour le self-continuum) et dans l'intervalle 90-330 cm^{-1} (pour le foreign continuum). Dans l'infrarouge lointain, nos données ont entraîné une modification significative du

modèle MT_CKD pour le self-continuum (diminution de 30 % dans la région du maximum du continuum où les études expérimentales précédentes étaient absentes).

Dans le proche infrarouge, les résultats sont généralement en accord avec le modèle de référence MT_CKD. Les données de continuum obtenues et les résultats connus du calcul ab initio du spectre des dimères d'eau permettent de suggérer un modèle de continuum qui prend en compte toutes les composantes. Les résultats obtenus dans le proche infrarouge valident le modèle MT_CKD tant pour le self-continuum que pour le foreign continuum, bien qu'une structure spectrale inattendue ait été détectée près de 8450 cm^{-1}. Cette absorption pourrait être une signature spectrale des dimères liés de la vapeur d'eau.

Contents

INTRODUCTION

Water vapour absorbs the radiation in frequency ranges from microwave to ultraviolet and beyond and represents more than 70% of the total atmospheric absorption at short wavelengths (< 3 μm) in clear sky conditions and about 50% for cloudy conditions (**Fig. 1**). Water vapor is the main greenhouse gas in the Earth's atmosphere and has a major role in its radiative balance.

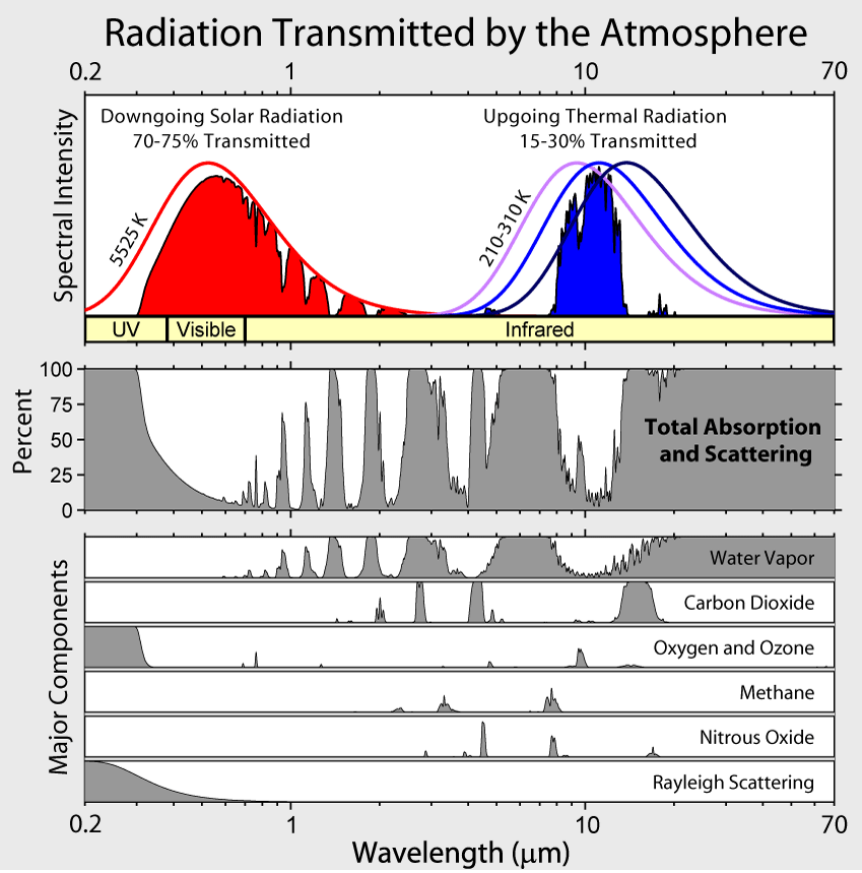

Fig. 1.

(from [https://commons.wikimedia.org/wiki/File:Atmospheric_Transmission.png]

Solar and thermal radiation transmitted by the Earth atmosphere (upper panel). Total absorption spectra and spectra of major components of the atmosphere (lower panels)

The absorption of water vapour consists of two contributions whose separation is somewhat arbitrary*: (i)* the water monomer local lines of rotational and vibrational–rotational bands due to the transition of molecules to higher rotational and vibrational energy levels and *(ii)* the continuum absorption corresponding to the difference between the measured ("true") absorption and that due to local lines calculated using a specified line shape model (**Fig. 2**). The physical origin of the continuum nature is not completely clear, there is no physically based continuum model, and in some spectral ranges the continuum has not been measured. In the atmosphere, the continuum decomposes into a self-continuum component due to interactions between water molecules (and thus varying quadratically with the water vapor number density) and a foreign continuum due to interaction between water molecules and other atmospheric species, mainly nitrogen or oxygen.

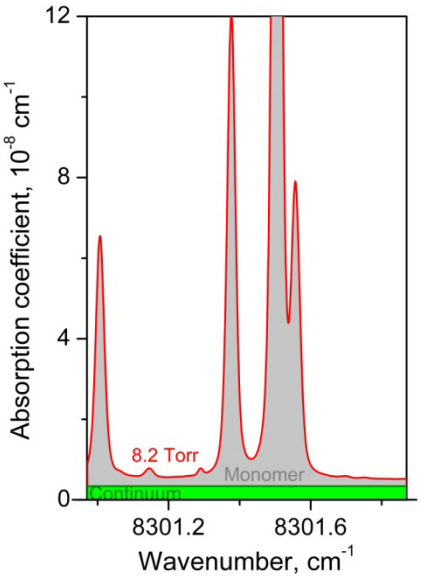

Fig. 2.

Example of an absorption spectrum of water vapor (recorded by CRDS at 8.2 Torr). Red line is total measured absorption. Grey area corresponds to water monomer lines contribution, green area is water continuum.

Theoretical calculations of monomer line positions from the first principles (*ab initio* calculations) do not yet compete with the experimental accuracy. The most accurate theoretical results on line positions are based on the analysis (fits) of experimental position values [Coudert2014, Furtenbacher2020]. As for the line intensities, modern *ab initio* calculations declare uncertainty of about 1% [Conway2020], but the results of experimental verification demonstrate that the uncertainty can be significantly larger and the difference between various "subpercent" calculations may exceed 1 % [Ovsyannikov2023] even for strongest lines within the ground vibrational state. For excited vibrational states the deviation of calculated line intensities of some bands can exceed 100% [Koroleva2023]. Possible mistakes in the identification of spectral lines may also lead to errors on line positions and intensities. These facts show the necessity of validation-tests and when necessary, improvements of our knowledge of the water monomer lines parameters.

The continuum has a relatively small value in comparison with the absorption of strong monomer lines nearby their centres, but in atmospheric transparency windows its contribution to the absorption of water vapor becomes significant and sometimes dominant (**Fig. 2**). In many frequency ranges, the absorption of water-related continuum is comparable to or exceeds the contributions of other atmospheric molecules. As for the continuum importance for the atmospheric research, the continuum of water vapour strongly impacts the Earth radiative balance and affects the radiation forcing of carbon dioxide [Firsov2023]. Also, the continuum affects propagation of laser radiation in the atmosphere and may interfere with the remote detection of atmospheric gases, aerosols and clouds by optical methods [Shine2012].

In this work, both water monomer lines and continuum absorption are studied experimentally using two different spectroscopic techniques (Fourier transform and cavity ring-down spectroscopy) in the far- and near-infrared range. Both spectral ranges are of importance for atmospheric science. They contain absorption spectra of many astrophysical, organic and atmospheric molecules such as O_2, NO_2, O_3, NH_3, CO_2 (**Fig. 3**).

The far infrared range is of particular importance because the maximum of the outgoing heat flux of the Earth falls in the THz range (0.1 – 10 THz or 3 - 333 cm^{-1}). But experimental study of water monomer line parameters and continuum are scarce in this frequency range due to the absence of wide-range radiation sources with sufficient spectral brightness and detectors with sufficient sensitivity (that is why this frequency range is called "terahertz gap"). However, using a synchrotron radiation is an option that allows wide-range spectrum recordings even in this frequency range. Previous measurements of ^{18}O enriched water spectrum [Mikhailenko2020-II] performed in SOLEIL synchrotron facility showed that experimental accuracy significantly exceeds the quality of available theoretical data and illustrates the need for additional measurements, in particular for the main isotopologue, $H_2{}^{16}O$. The importance of this region for the Earth's radiation budget is a major motivation of the Far-infrared-Outgoing-Radiation Understanding and Monitoring (FORUM) mission of European Space Agency. One of the identified goals of this mission is to "fill the observational gap across the far-infrared (from 100 to 667 cm^{-1} or 3-20 THz), never before sounded in its entirety from space" [https://www.forum-ee9.eu/].

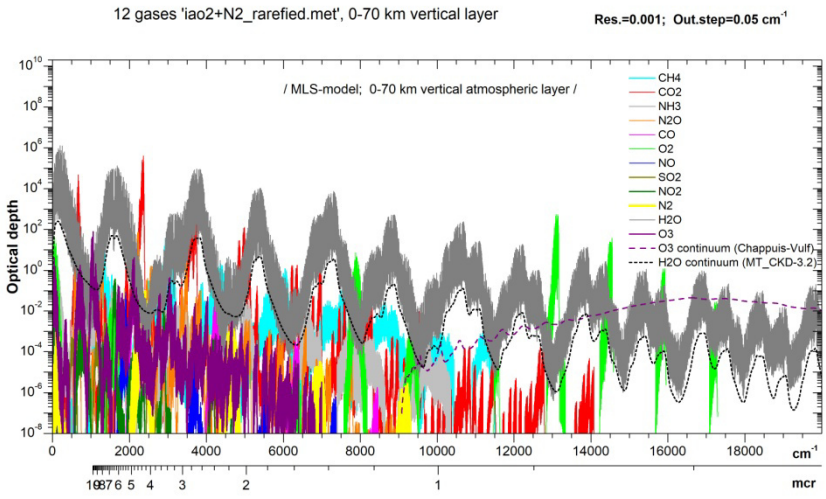

Fig. 3. (Courtesy of I. Ptashnik and A. Simonova)
Optical depth for the main atmospheric gases.

As for the near-infrared frequency range, a maximum of incoming Solar radiation entering the atmosphere is located close to this spectral range. The frequency range considered in this work corresponds to high energy edge of the *J* atmospheric transparency window (**Fig. 1**, 1.1-1.4μm) and is considered for air-mass determination in a number of satellite missions in the Earth atmosphere [Mendonca2019] and for greenhouse gas monitoring [Bertaux2020]. In order to achieve the necessary

accuracy in these measurements, the absorption of water vapor must be known with high accuracy. Although the continuum measurements were performed in the low-frequency part of the spectral range under consideration [Campargue2016], it had not been measured in the rest of the range (**Fig. 4**).

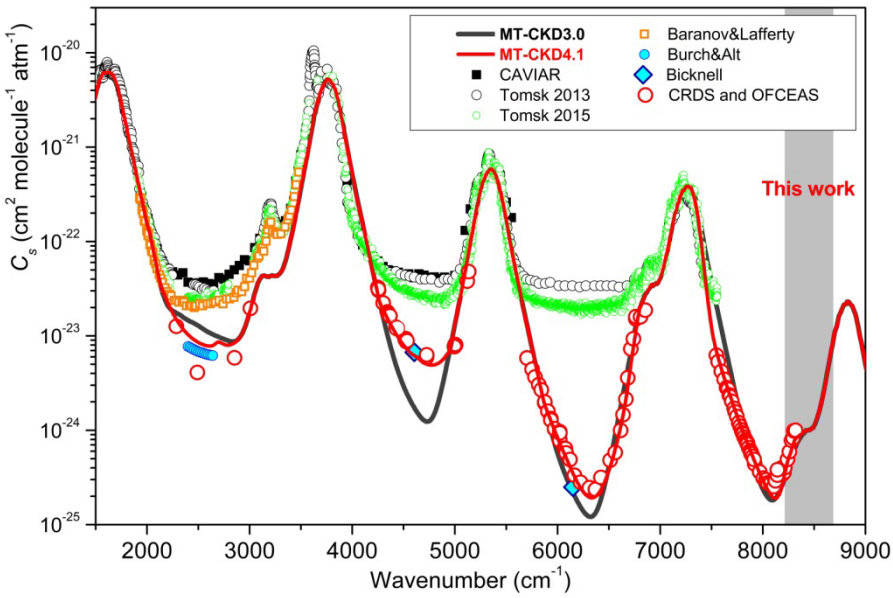

Fig. 4.

Overview of the near-infrared water vapour self-continuum measurements at close-to-room temperatures and MT_CKD model. Error-bars are not shown for clarity.

Note: the CAVIAR [Ptashnik2011] and Tomsk [Ptashnik2013,2015] room-temperature measurements had very high uncertainty in windows with error-bars varying from 50% (Tomsk) to 90% (CAVIAR) and so, were considered by the authors as very rough estimations of the continuum absorption in windows.

For calculation of water vapour absorption with the sub-percent accuracy required today for atmospheric applications in the wide spectral, pressures, and temperatures ranges, a physically based absorption model is required. The general goal of this work is to make another step towards building such model that correctly takes into account all the mechanisms contributing to water absorption. We will report new measurements of water resonance spectrum (central frequencies and line intensities) and continuum absorption in far- and near-infrared ranges. Spectra recordings for line parameters determination in the near infrared range are carried out for the first time using the CR-CRDS (comb-referenced cavity ring-down spectroscopy) technique, which allowed to increase the sensitivity by 3 orders of magnitude in comparison with previous studies [Régalia2014] and increase the accuracy of line positions determining by one order of magnitude, in comparison with previous CRDS measurements in the low-frequency part of this frequency range [Campargue2015].

By its definition, the retrieved continuum is inextricably linked to the resonance spectrum model that is subtracted from the measured absorption. Both of total absorption components will be

examined in this thesis. The first chapter presents the basics of molecular spectroscopy underlying the total atmospheric absorption modelling and description of experimental techniques used in this work. In addition, it contains a literature review of continuum measurements. The second chapter is devoted to experimental determination of water lines parameters (namely, line positions and intensities) and validation-tests of line parameters from reference line lists, such as HITRAN and W2020. This is limited by water with natural isotopic abundance, although the further analysis of spectra recorded with different H_2O isotopologues concentrations is planned (included ^{17}O-enriched water). The third chapter presents results of four series of continuous absorption measurements at a room temperature. The further research may be related to the study of the temperature dependence of the continuum in the near infrared. Also, the third chapter offers an approach for physically based continuum modelling. The development of theoretical calculations allows refining the proposed model and expanding it to other frequency ranges.

Chapter 1. Theoretical and experimental basis

The research objects of this work (water monomer lines and continuum) require different approaches to record and analyse the experimental data. However, all subsequent analysis is based on the general basic principles of total absorption modelling presented in the first part of this chapter. The theory presented in this chapter combines seemingly unrelated studies into a single research and emphasizes that the joint study of water lines and continuum is a step towards a global goal – the construction of a physically based total absorption model.

The second part of the first chapter is devoted to the description of the two (very different) spectrometers used in this work: Fourier transform spectrometer (FTS) (**Section 1.2.1**) and cavity ring-down spectrometer (CRDS) (**Section 1.2.2**). At first glance, the analysis of technical details may be out of the scope of this theoretical chapter, but this work is not devoted to the experimental setup development and both spectrometers were used as ready-made tools for obtaining data, and not as separate research objects. Therefore, experimental setups description is also considered as a part of theoretical basis.

1.1 Total absorption modelling approach

In the most general case, the absorption spectrum of a real gas in equilibrium state can be calculated on the basis of the Wiener-Khintchine theorem as a Fourier transform of a dipole moment autocorrelation function multiplied by number density of absorbers [Hartmann2008]. Thus, to calculate it accurately, non-instantaneous and inelastic collisional interactions between all the molecules should be taken into account (*i.e.* gas should not be considered as ideal).

For real pure gases at equilibrium thermodynamic conditions, the state equation can be written as a virial series $P(T)=A(T)\rho+B(T)\rho^2+C(T)\rho^3+\ldots$, where P is the pressure, ρ is a density of molecular states (molecule/cm^3), T is the temperature, $A(T)$, $B(T)$ and $C(T)$ are virial coefficients. The first virial coefficient $A(T)=RT/V_m$ corresponds to the ideal gas case (R is the ideal gas constant, V_m is the molar volume), the other coefficients reflect the interactions efficiency in the gas. Particularly, the second virial coefficient $B(T)$ characterises pair interactions.

Similarly, the total gas absorption coefficient $\alpha(\nu,\rho)$ in cm^{-1}, can be written as the following series [Serov2017]:

$$\alpha(\nu,\rho)=\alpha_1(\nu,\rho)\rho+\alpha_2(\nu,\rho)\rho^2+\alpha_3(\nu,\rho)\rho^3+\ldots, \quad (1.1)$$

where $\alpha_1(\nu,\rho)$ (cm^2/molecule), $\alpha_2(\nu,\rho)$ (cm^5/molecule^2), $\alpha_3(\nu,\rho)$ (cm^8/molecule^3) are normalized spectra of single, pair, triple molecules etc. (monomolecular, bimolecular and trimolecular absorption, correspondingly). Virial coefficients are implicit amplitude multipliers of the corresponding spectra.

Taking into account interactions between all molecules simultaneously is enormously hard. However, in the atmospheric air at a room temperature, the average distance between the molecules (30 Å) is about 10 times the mean molecular size. Thus, triple interactions are rare and the pair

interaction approximation is applicable [Hartmann2008] and all the terms except the first two can be neglected in the $P(T)$ and $\alpha(\nu,\rho)$ series.

Thus, the total absorption $\alpha(\nu,\rho)$ can be considered as a sum of mono- and bimolecular absorption. The origin and modelling of both of these parts are discussed in **Sections 1.1.1** and **1.1.2**, respectively. However, the more common way in experimental studies is to treat the total absorption as a sum of monomer lines and continuum absorption spectra. The relationship between these two approaches is examined in **Section 1.1.3. Section 1.1.4** presents continuum data review for far- and near-infrared spectral range.

1.1.1 Monomolecular absorption

Monomer is a single molecule moving between two sequential collisions in the field of the intermolecular interaction potential and absorbing the electromagnetic field radiation during mean free time. Monomolecular absorption can be defined as a gas averaged power spectrum of the monomer dipole moment train oscillations lasting until its total decorrelation due to a collision. Monomolecular absorption coincides with a total absorption if the gas is ideal, *i.e.* molecules do not interact between instantaneous collisions.

1.1.1.1. Monomer lines

Monomer lines occur due to transition of the molecule to a higher energy level, after absorption of a quantum of radiation. It is also called resonance (selective) absorption spectrum.

The internal kinetic energy of a molecule can be divided into components corresponding to its rotation as a whole, various vibrations of its atoms and the movement of electrons. Depending on the photon energy, absorption leads to rotational, vibrational or electronic transition in the molecule (within the framework of the Born-Openheimer approximation, the motion of nuclei is considered slow in comparison with the motion of an electron) that changes the corresponding movements. The energy of microwave and far-infrared radiation (3×10^8 to 2×10^{10} Hz, or 0.01 – 1 cm^{-1}) is sufficient to change the rotation of H_2O molecule, but not enough to cause vibrations or electronic transitions. Higher frequencies of the middle and near-infrared correspond the region of the vibration-rotational spectra of water molecule. To change the energy of valence electrons and observe electronic transitions, ultraviolet or visible radiation is needed (3×10^{14} to 3×10^{16} Hz, or 10^4 – 10^6 cm^{-1}). This leads to the appearance rotational, vibration-rotational and electronic spectral lines grouped into corresponding spectral bands.

Each energy level of a molecule is identified by a set of quantum numbers. The water molecule is an asymmetric top molecule. Its rotational states are characterized by a set of 3 quantum numbers corresponding to rotation around the three axis a, b and c denoted with increasing of the moment of inertia $I_a < I_b < I_c$ (**Fig. 1.1**). The first rotational quantum number is associated with the total angular momentum excluding nuclear spin J, the second K_a and the third K_c refer to the two largest projections

of angular momentum. Similarly, vibrational states are marked as ($v_1v_2v_3$) with three quantum numbers v_1, v_2, v_3 characterize vibrational states corresponding to three normal vibrational modes (two stretching modes with fundamental frequency ν_1 for symmetric and v_3 for asymmetric one and bending mode v_2, **Fig. 1.1**). Rotational transitions without changing vibrational state are denoted as follows: $J'_{K'_a,K'_c} \leftarrow J''_{K''_a,K''_c}$, prime and double primes refer to upper and lower states, respectively. Vibrational transitions are denoted as follows: $(v'_1v'_2v'_3) - (v''_1v''_2v''_3)$. To identify each ro-vibration transition (in certain electronic state), 12 quantum numbers are used: $v'_1v'_2v'_3\,J'K'_aK'_c \leftarrow v''_1v''_2v''_3\,J''K''_aK''_c$. Also, the set of ro-vibrational transitions belonging to one vibrational band (when the initial vibrational state is ground *i.e.* a cold band) is denoted as the sum of harmonics of fundamental oscillations $av_1 + bv_2 + cv_3$, where $\nu_{1,2,3}$ are fundamental oscillation frequencies and *a, b, c* correspond to the vibrational excitation of the upper vibrational level.

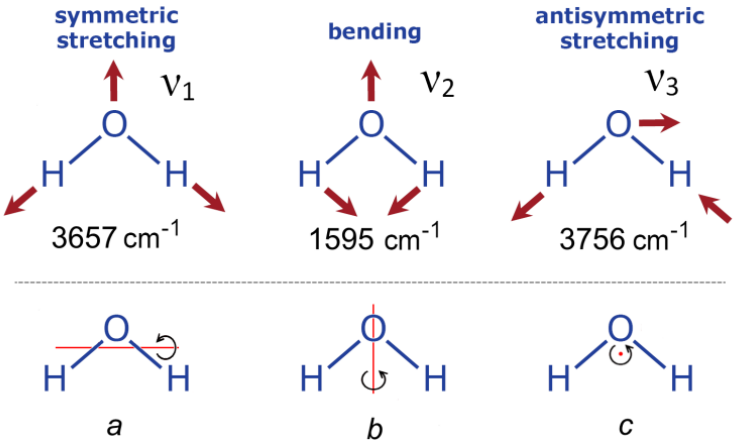

Fig. 1.1. (from [Vasilchenko2016])
Normal modes and fundamental frequencies of H_2O molecule.

The absorption coefficient for each line α_{line} is a product of concentration n (molecule/cm^3) of absorbing molecules, spectral line intensity S_{ij} (cm/molecule) and line profile (line shape function) *I(ν)* (cm):

$$\alpha_{line}(\nu) = nS_{ij}I(\nu), \qquad \int_{-\infty}^{+\infty} I(\nu)d\nu = 1 \tag{1.2}$$

Spectral line intensity is a characteristic of corresponding transition from energy level *i* to level *j*. It depends also on temperature. Hereafter, the units that are used in this work will be indicated in parentheses just after the first mention of a physical quantity despite that most formula are general.

In gases, the line shape is mostly determined by Doppler and pressure (collisional) broadening effects (assuming the natural line broadening due to the spontaneous transitions is negligible). Both mechanisms allow photons with an energy close to the transition energy to interact with molecule. The first one is caused by velocity distribution of the molecules resulting to a Doppler shift of the transition frequency and led to the Gaussian line shape:

$$I_D(\nu) = {}^{1}/_{\Delta\nu_D\sqrt{\pi}}\, e^{-(\frac{\nu-\nu_0}{\Delta\nu_D})^2} \tag{1.3}$$

$$\Delta\nu_D = {\nu_0}/{C}\sqrt{{2kT}/{M}}. \quad (1.4)$$

In this formula ν (cm^{-1}) is the frequency, ν_0 is the central frequency, C (2.9979·10^8 m/s) is speed of light, k is the Boltzmann constant (1.38×10^{-23} m^2 kg s^{-2} K^{-1}), M (18-21 g/mol depending on water isotopologue) is molecular mass. $\Delta\nu_D$ (cm^{-1}) is half width of Doppler line profile at the *1/e* level. It is on the order of 1.7·×10^{-4} cm^{-1} near 100 cm^{-1} and 0.014 cm^{-1} near 8300 cm^{-1}.

The pressure broadening is related to the reduction of the lifetime of a molecule in a state resonant with the field because of collisions between molecules. It is described by a Lorentzian line shape (for $\nu_0 >> \Delta\nu$):

$$I_L(\nu) = \frac{1}{\pi}\frac{\Delta\nu_L}{(\nu-\nu_0)^2 + {\Delta\nu_L}^2} \quad (1.5)$$

$$\Delta\nu_L = \Delta\nu_{H_2O} + \Delta\nu_{foreign} = P_{H_2O}\gamma_{H_2O} + P_{foreign}\gamma_{foreign}. \quad (1.6)$$

In this formula $\Delta\nu_L$ (cm^{-1}) is the collisional line halfwidth at half maximum consisting (in the case of H_2O spectrum) of self-broadening $\Delta\nu_{H_2O}$ and broadening by buffer (foreign) gas $\Delta\nu_{foreign}$. P_{H_2O} and $P_{foreign}$ are water and foreign gas partial pressures, correspondingly. γ_{H_2O} (cm^{-1}/atm) is self-broadening coefficient and $\gamma_{foreign}$ (cm^{-1}/atm) is foreign gas-broadening coefficient. In both frequency ranges under consideration, γ_{H_2O} is in order of 0.5 cm^{-1}/atm and $\gamma_{foreign}$ is in order of 0.06 cm^{-1}/atm both for far- and for near-infrared range without noticeable manifestations of dependence on vibrational excitation according to HITRAN database [Gordon2022].

In the case of $\nu_0 \sim \Delta\nu$ (microwave and far-infrared spectral ranges), the contribution of the resonance on the negative frequency ($-\nu_0$) cannot be neglected (it is resulted mathematically from equation of a harmonic oscillator with attenuation). Also, for wide lines modelling in the far-infrared spectral region, the dependence of the integral intensity S_{ij} on the magnitude of the quantum energy $h\nu_0$ and frequency dependence of the difference in population of transition levels should be considered. The latter occurs because the lower energy levels are usually more populated and transitions involving them are more probable. Thus, assuming that the distribution of molecules after each collision remains of Boltzmann-type, formula (1.5) transforms in the following way [Van Vleck1945]:

$$I_{VW}(\nu) = \frac{1}{\pi}\frac{\nu^2}{\nu_0^2}\left(\frac{\Delta\nu_L}{(\nu-\nu_0)^2 + {\Delta\nu_L}^2} + \frac{\Delta\nu_L}{(\nu+\nu_0)^2 + {\Delta\nu_L}^2}\right) \quad (1.7)$$

The more general line shape was suggested in [Van Vleck1977]:

$$I_G(\nu) = I_{VW}(\nu)\cdot R(\nu), \quad (1.8)$$

$$R(\nu) = \frac{\nu}{\nu_0}\frac{tanh\left({h\nu}/{2kT}\right)}{tanh\left({h\nu_0}/{2kT}\right)}, \quad (1.9)$$

where $R(\nu)$ is so-called radiation term.

Within the approximation that Doppler and collisional broadening work independently, the resulting line profile corresponds to a convolution (denoted as $*$) of the Doppler and Lorentzian line shapes (Voigt line profile (1.10)):

$$I_V(\nu) = \int_{-\infty}^{\infty} I_D(x) I_L(\nu - x) dx = I_D(\nu) * I_L(\nu) \quad (1.10)$$

However, the broadening mechanisms are not independent as collisions change velocity of molecules and collision frequency depends on molecule speed. It leads to distortion of a spectral line shape in the vicinity of its center in comparison with the model (1.10) (real line is slightly narrower and higher). Non-Voigt line-shape effects (e.g. Dicke narrowing and speed-dependent effects) becomes visible with signal to noise ratio higher than 100-1000 (depending on colliding partners) for isolated lines. For today, the most advanced line profile taking into account these effects is HTP (Hartmann-Tran profile, or partially-Correlated quadratic-Speed-Dependent Hard-Collision line profile, pCqSDHC) [Ngo2013]. Simpler models (including the Voigt profile) are the limits of the HTP.

Voigt line shape was used both for water vapor line parameters determination and for continuum retrieving in the frame of this work, except for continuum in the far-infrared where Eq. 1.7 was sufficient at the pressures under consideration. Although the deviations from this profile were visible in the CRDS spectra in the near-infrared range, their influence to retrieved parameters were much less than from other uncertainty sources. Also, this work does not consider line mixing (which is also known as line interference effect or spectral exchange). This effect impacts the line wings behaviour and thus can influence the continuum but it was shown that for most of the water lines at atmospheric conditions, this effect is negligible [Ma2014].

1.1.1.2. Monomer line wings

Line profiles mentioned in Chapt. 1.1.1.1. (Eqs. 1.5, 1.7, 1.8, 1.10) are derived using the impact approximation assuming that collisions are almost instantaneous and time between collisions τ_f is much longer than collision time, τ_c. However, molecules interact with each other during some finite time before and after collision.

The impact approximation works for frequency detuning from the line centre $\Delta\nu_c << 1/2\pi\tau_c$. At higher detuning, corresponding to far line wings) calculations using (Eqs. 1.5, 1.7, 1.8, 1.10) are not valid. Line wings can be either above or below the calculations, which is so-called super- and sub-Lorentzian behaviour, correspondingly [Clough1989, Serov2017].

The *ab initio* far line wings model has not been elaborated so far. Existing models beyond the impact approximation use asymptotic [Tvorogov1976, Klimeshina2013] or quasistatic [Tipping1995, Ma2008] approaches. The former is based on fitting intermolecular potential parameters using experimental data, the latter is an estimation of very far line wings magnitude corresponding to frequency detuning from the line centre $\nu_c >> 1/2\pi\tau_c$. Although an agreement with experiment is demonstrated for particular spectral bands [Rodimova2018, Ma2008], the accuracy of the continuum magnitude and its temperature dependence in a wider frequency range is questionable. Also, the use of asymptotic approach is characterized by a large number of empirical parameters.

Semi-classical trajectory-based formalism described in [Chistikov2019] looks promising for calculating the far line wings, but it requires proper solution for molecular angular momentum requantization problem during a collision.

In climate and weather prediction models the semi-empirical MT_CKD (Mlawer–Tobin–Clough–Kneizys–Davies) model [Mlawer2012] is commonly used. This is the only continuum model, which covers the whole frequency range 0-20000 cm^{-1}, of importance for the Earth radiation balance. The MT_CKD model is a successor of CKD model [Clough1989], the latter assumes that continuum is of exclusively monomolecular origin and occurs due to the monomer lines wings. CKD and MT_CKD is based on Van Vleck and Huber line shape (Eqs. (1.8-1.9), which is equivalent to Lorentzian in the infrared) with line wings modified by a χ-function. For a single line, the line wing absorption normalized to the number density of water molecules is written as

$$C(\nu) = R(\nu)S_{ij}\left(f_c(\nu-\nu_0)\chi(\nu-\nu_0) + f_c(\nu+\nu_0)\chi(\nu+\nu_0)\right) \tag{1.11}$$

$$f_c(\nu \mp \nu_0) = \begin{cases} \dfrac{1}{\pi}\dfrac{\Delta\nu}{\nu_{cut}^2 + \Delta\nu^2}, & |\nu \mp \nu_0| \geq \nu_{cut} \\ \dfrac{1}{\pi}\dfrac{\Delta\nu}{(\nu \mp \nu_0)^2 + \Delta\nu^2}, & |\nu \mp \nu_0| \leq \nu_{cut} \end{cases} \tag{1.12}$$

where ν_{cut} is a wing cut-off frequency equal 25 cm^{-1}.

This approach takes into account finite duration of collisions by empirical modification of line wings. The χ-function does not distort Lorentzian line shape at small detuning from line centre, reduces the line wings contribution in the transparency windows between water bands (sub-Lorentzian wings at very large detuning) and increases the contribution within water bands (super-Lorentzian wings at intermediate detuning), thus providing a better agreement with the experimental data. However, the χ-function method does not explain negative continuum temperature dependence.

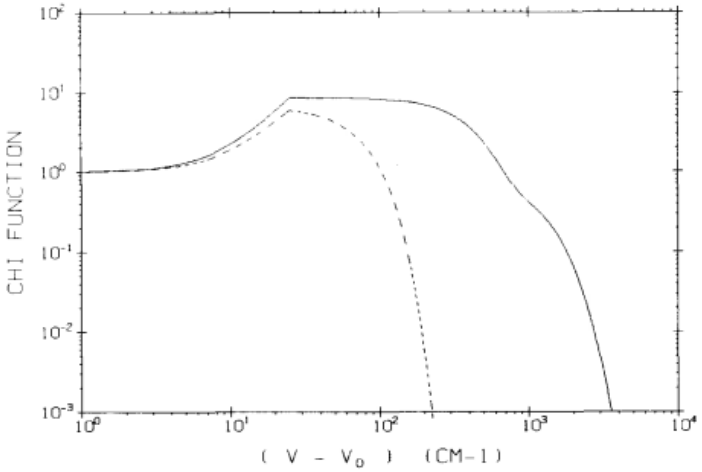

Fig. 1.2. (Fig.4 from [Clough1989])

The χ-function for water vapour lines depending on frequency detuning from the line centre at 296 K. The solid curve is for self-broadening; the dashed curve is for foreign-broadening .

The continuum modelling by MT_CKD model is based on the contributions from two components: a "weak interaction term" and an "allowed term". The former dominates in in-band regions and includes bimolecular absorption contribution in effective way (discussed in **Sect. 1.1.2**). The latter dominates in windows of transparency between water vapour absorption bands and corresponds to line wings contribution accounting by χ-function Numerical coefficients of the model are empirically adjusted according to latest laboratory or atmospheric data at disposal (most of laboratory measurements taken into account are listed in Table 1.1). These coefficients are different for each spectral region.

The most recent version of the model is presented on the HITRAN website [https://hitran.org/mtckd/, Mlawer2023]. It is adjusted to continuum measurements and is updated when new data becomes available. Due to that, different MT_CKD versions may differ by orders of magnitude (see **Fig. 4** and [Mlaver2023]). However, in the frequency ranges where continuum measurements are absent, the MT_CKD cross-sections result from long-range extrapolation which has to be validated.

1.1.2 Bimolecular absorption

This chapter is devoted to the contribution of paired molecules to total absorption ($\alpha_2(\nu,\rho)$ from Eq. (1.1)). It describes the types of paired states, the reasons why they arise and their contribution to the total absorption. This is mostly on the basis of general statements, which are specified for water vapor, as well as for nitrogen, oxygen and air. In addition, the different concentration of paired molecules in dry and humidified gases is explained.

Although the available information on theoretical calculations and modeling of bimolecular spectra is rather scarce, it is sufficient to evidence the contributions of bimolecular absorption both in far- and in near-infrared range (see Chapter 3.5).

1.1.2.1. Types of paired states and the shape of their spectra

When two colliding molecules are very close to each other, the molecular structure could be slightly changed under the short-range repulsive forces. It leads to the appearance of additional transient polarisation and dipole moment. Two (even initially non-polar) molecules form so-called bimolecular (or pair) state and absorb the radiation as a single object.

Qualitatively, radial motion of two interacting molecules around their centre of mass can be characterized using the effective potential of pair interaction (Eq. (5.22) from [Hirshfelder1954]) consisting in the first approximation on the Lennard-Jones pair interaction potential $U_{LJ}(r)$ and the energy of rotational motion of the interacting pair with respect to its centre of mass $U_r(r)$:

$$U_{eff}(r) = U_{LJ}(r) + U_r(r) = 4D_e\left[\left(\frac{r_e}{r}\right)^{12} - \left(\frac{r_e}{r}\right)^{6}\right] + \frac{1}{2}\mu v_r^2\frac{b^2}{r^2} \qquad (1.13)$$

where D_e is the depth of the potential well, r is the distance between the molecules, and r_e is the equilibrium distance where the potential reaches its minimum. $\mu = m_1 m_2/(m_1+m_2)$ is the reduced mass, m_1 and m_2 are the mass of colliding molecules, υ_r is their relative speed, b is an impact parameter.

Analysis of the shape of (1.13) at different rotational energies of the pair shows possible types of bimolecular states. As **Fig.1.3** illustrates, the function (1.13) presents a well at certain rotational energy values, so colliding molecular pair can tunnel through the barrier and end up inside the potential well, forming a double molecule called a dimer. This dimer is metastable (or quasibound) because the pair total energy is less than the energy of the maximum of effective potential, but greater than the "zero" energy (the interaction energy of two monomers separated by an infinite distance). This means that the energy of a metastable dimer is greater than the dissociation energy and it can dissociate spontaneously by tunnelling through a potential barrier. A metastable dimer can become stable after a successful collision with a third molecule, which takes out the energy excess above zero energy. When the effective potential (1.13) does not have a maximum (*i.e.* rotational energies of the pair are large), the formation of dimer is impossible (even metastable dimer). In this case, the pair of molecules flies apart after a single approach during collision. Such pair state is called a free pair.

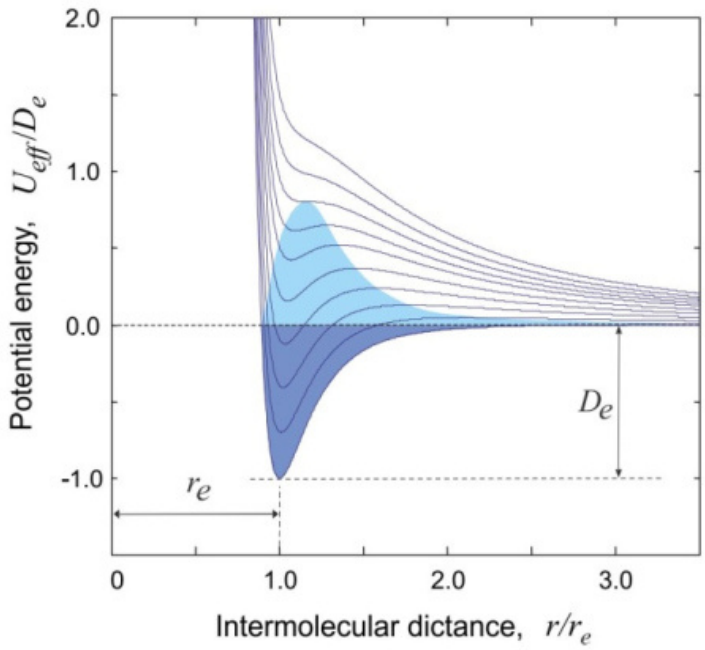

Fig. 1.3. (from [Tretyakov2022])
The set of effective intermolecular interaction potentials for different rotational energy of pair (the larger the energy, the higher the potential curve). The shaded areas correspond to bound (dark blue) and quasi-bound (light blue) dimers and free pairs (unshaded area above the light blue)

A short-term transient dipole moment is acquired due to a change of structure of molecules formed a free pair, and additional absorption appears. The “ro-vibrational” absorption bands of free pairs formed by nonpolar molecules are exactly at the positions where they would have been located if

these molecules had dipole moments. An additional absorption of polar molecules looks like a plinth under their resonance spectrum and qualitatively repeats the envelop of the resonance spectrum. Both for polar and non-polar molecules, free pair spectrum has smooth frequency dependence as free pair state lifetime is quite short.

The stable dimer has its own intermolecular (between two monomers) ro-vibrational structure and may have tunnelling degrees of freedom in addition to nuclear motion typical for each of two single monomers. It leads to more complex energy level system than for a single molecule and to a higher spectral congestion [Krupnov2009]. Stable dimer spectral bands corresponding to vibrational modes of monomers are located close to the same wavenumbers as a corresponding monomer vibrational bands. Dimer lines are unresolved at the atmospheric pressures and the dimer spectrum is formed by smooth subbands corresponding to different groups of vibrational transitions within particular absorption band [Ptashnik2011II].

Theoretical calculations of the dimer spectrum are very challenging. Only a few quantum-chemical calculations are available for the water dimer. Its complete (up to dissociation of a hydrogen bond) tunnelling-vibration-rotation spectrum in the millimeter and far infrared domains is presented in [Scribano2007, Salmi2008]. Water dimer vibrational frequencies and their relative intensities are calculated in [Kjaergaard2008]. These results allow confirming the dimer spectrum detection in the microwave [Tretyakov2013, Serov2014, Koshelev2018] and infrared in-band spectral ranges [Ptashnik2004, Paynter2007, Ptashnik2008, Ptashnik2011II, Birk2020, Simonova2022]. However, dimer spectrum cannot be resolved in experiments and its simulations on the basis of calculated vibrational modes in the middle- and near-infrared range are too approximate because the calculations do not take into account rotational and tunnelling motion of the dimer.

The metastable water dimer absorption spectrum has not been calculated yet because of the very high complexity of this system. The paper [Vigasin2010] proposes to consider the spectrum based on two boundary cases. In one extreme case (very short lifetime), metastable dimer looks like two monomers almost freely rotating near each other. Its spectrum is similar to the doubled spectrum of a monomer, homogeneously broadened by a short lifetime. This model of the metastable dimer spectrum was used in [Serov2017, Ptashnik2011II, Odintsova2013, Simonova2022] to derive water dimer spectral contribution to the in-band water vapour continuum in different spectral regions from mm- to near-visible. However, such consideration does not reproduce the spectral features arising from the rotation of the dimer around its center of mass. In another extreme case, a metastable dimer is close to a stable dimer with a shortened lifetime. Thus, the spectrum of a metastable dimer repeats the spectrum of a stable dimer broadened by lifetime as considered in [Odintsova2013, Serov2014]. In this case the free rotation of monomers is not fully reflected in the spectrum. The real spectrum of metastable dimer is something in between of these two extreme cases.

Collision-induced absorption (CIA) is part of bimolecular absorption consisting of free pairs or free pairs and metastable dimers spectra. CIA does not have any commonly accepted definition, as discussed in detail in [Vigasin2014]. It is “arising from the transient dipole created during

intermolecular collision" [Hartmann2008]. Non-polar diatomic molecules such as N_2 almost do not form dimers (see **Sect. 1.1.2.2**.) and for such simple molecules the CIA component could be calculated *ab-initio* [Karman2015] or using semi-classical trajectory-based formalism [Chistikov2019]. However, the development of both methods is required to apply them to a water molecule.

1.1.2.2. Pair states in dry and wet gases

At relatively low pressures, in the frame of binary collision approximation, the density of monomolecular states ρ_1 (molecule/cm^3) significantly exceeds the density of bimolecular states ρ_2 and following equations are valid: $\rho_1 = \rho - \rho_2 - ... \approx \rho$; $\rho_2 \approx K_2^{\rho} \rho^2$, and similarly $P_2 \approx K_2^P P^2$. K_2^{ρ} (cm^3/molecule) and K_2^P (atm^{-1}) are equilibrium constants of bimolecular states. (Note that in this chapter P is in atm).

As it was mentioned above, the virial coefficient $B(T)$ characterizes pair interactions and associated pair states concentration. It can be expressed as the sum of the coefficients related to the number of bound dimers $B_{BD}(T)$, quasibound dimers $B_{MD}(T)$ and free pairs $B_F(T)$ (all are in cm^3): $B(T) = B_{BD}(T) + B_{MD}(T) + B_F(T)$. Bimolecular states equilibrium constants $K_2^{\rho,P}$ also consist of equilibrium constants of stable dimers $K_{BD}^{\rho,P}$ and metastable dimers $K_{MD}^{\rho,P}$: $K_2^{\rho,P} = K_{BD}^{\rho,P} + K_{MD}^{\rho,P}$.

Equilibrium constants are characteristics of a corresponding states number: $P_{BD} = K_{BD}^P P^2 = K_{BD}^P (\rho kT)^2$ and $P_{MD} = K_{MD}^P P^2 = K_{MD}^P (\rho kT)^2$. Thus, 10 Torr H_2O contains about 0.1% of stable water dimers (with K_{BD}^P= 0.036 atm^{-1} from [Serov2014]). The connection between the second virial coefficient and the equilibrium constants is the following: $B_{BD}(T) = -K_{BD}^P RT$, $B_{MD}(T) = -K_{MD} RT$, $B_F(T) = b_0$. b_0 is excluded volume [Stogryn1959].

The cross-section of total absorption bimolecular component $C_p(\nu)$ (cm^2/molecule/atm) can be written as:

$$C_p(\nu) = \alpha_2(\nu) K_2 k_B T = K_{BD} BD(\nu) + K_{MD} MD(\nu) + K_F F(\nu) \qquad (1.14)$$

In this formula, K_F is the free pairs equilibrium constant, $BD(\nu)$, $MD(\nu)$ and $F(\nu)$ (in cm^{2}molecule^{-1}) are the spectra of dimers (stable and metastable) and of free pairs normalized by their number density

Let us note that the difference in the ratios of bimolecular states in the dry gases and in water vapor lead to different $B(T)$ value. In N_2, O_2 and dry air stable dimers are almost absent at typical for the Earth's atmosphere temperature, but a significant number of quasi-bound dimers and free pairs are present [Vigasin1991]. In contrast, a large number of stable and metastable dimers are present in water vapor (see Fig. 4 in [Vigasin1991]). This difference is caused by two reasons. The water molecule has more internal degrees of freedom to redistribute the excess energy of two monomers for forming a metastable dimer (a pair of molecules does not fly apart instantly). To form a stable dimer, the metastable pair needs to get rid of the excess energy but nitrogen and oxygen molecules lack a dipole moment and can interact with others only at shorter distances thus having less probability for the successive collision than polar water molecules.

The second virial coefficient in nitrogen [Whitmore1980] and oxygen [El-Kader2016] is negative, but close to zero, whereas it is much larger in absolute value in water vapor [Tretyakov2011], where the presence of a large number of stable dimers has been proven (**Fig. 1.4**) [Tretyakov2013].

In addition to the above–mentioned paired states, heterodimers H_2O–N_2 and H_2O-O_2 may be present in moist nitrogen, oxygen and air. However, the theoretical study of such complexes is difficult, and significantly less literature is available on then in comparison with the water vapor dimer $(H_2O)_2$.

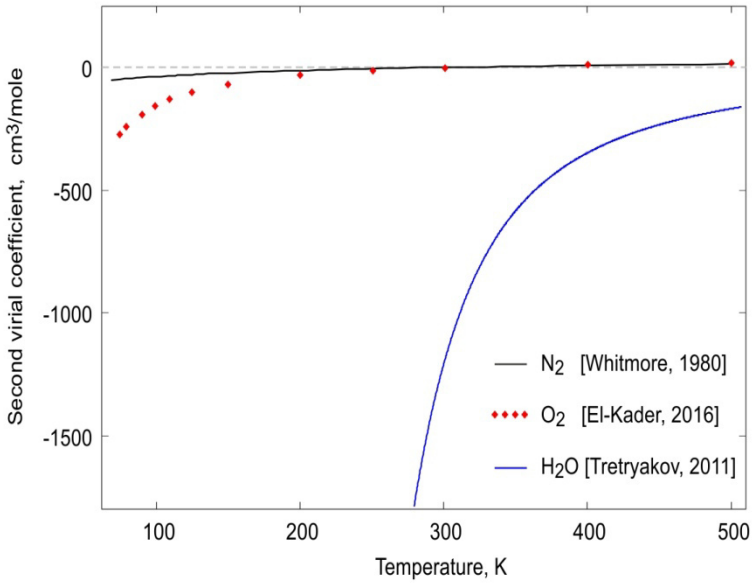

Fig. 1.4. (from [Tretyakov2018])

Second virial coefficients of water, nitrogen and oxygen in accordance with the data reported in [Whitmore1980], [El-Kader2016] and [Tretyakov2011], respectively.

Estimates of heterodimer presence in the atmosphere are difficult, since a significant part of the complexes are in short-lived metastable states [Kjaergaard2003]. Methods of statistical physics allow estimation of heterodimer concentrations in atmospheric air only with uncertainty of the order of magnitude. Nevertheless, according to estimates [Svishchev1998, Vaida2000, Robinson2003], the concentration of H_2O—N_2 and H_2O—O_2 heterodimers in atmospheric air significantly exceeds the concentrations of methane (CH_4), nitrogen oxide (N_2O), carbon monoxide (CO) and freon, which are important in calculating the greenhouse effect of the Earth. The contribution of the H_2O—N_2 and H_2O—O_2 heterodimers to the total absorption of solar radiation by the atmosphere is comparable to the contribution of the water dimer [Kjaergaard2003] and expected to be a contributor to water continuum (see below).

1.1.3 Continuum as an empirical part of the total absorption model

The description of the total absorption modelling described in **Sections 1.1.1**. and **1.1.2**. is physically based, but practically difficult to apply. Despite significant advances, at the moment, it is possible to calculate the total absorption taking into account the interaction of molecules only for relatively simple molecular pairs. (See, for example, ab initio calculation and results with semi-classical trajectory-based formalism for N_2-N_2 [Karman2015, Chistikov2019] and for CO_2-Ar [Chistikov2021]) Practically the total absorption coefficient, α_{total}, is considered semi-empirically as a sum of resonance spectrum $\alpha_{res}(\nu, P_{H_2O}, P_{foreign})$ and continuum $\alpha_{cont}(\nu, P_{H_2O}, P_{foreign})$.

$$\alpha_{total}(\nu, P_{H_2O}, P_{foreign}) = \alpha_{res}(\nu, P_{H_2O}, P_{foreign}) + \alpha_{cont}(\nu, P_{H_2O}, P_{foreign}), \quad (1.15)$$

However, continuum is not measurable by itself and its uncertainty should consider all the inaccuracies of the resonance spectrum model which are related to the line shape with corresponding parameters, line list and line wings approach, as well as the contribution of weak lines, possibly not considered in the calculation. This makes the subdivision of the total absorption into a resonant spectrum and the continuum somewhat arbitrary. Also, this obliges to use the retireved continuum data only in combination with the resonance spectrum model that was used to retrieve the continuum from experimental spectra. Inaccurate resonance spectrum subtraction prevents to identify the mechanisms of continuum formation as illustrated in [Tretyakov2018].

Water continuum can be divided on the part resulted of interactions between water molecules (water-related continuum which consists of self-continuum $\alpha_{self}(\nu, P)$) and of interactions between water molecules with molecules of other gases, in the atmospheric air, mostly nitrogen and oxygen (foreign-continuum $\alpha_{foreign}(\nu, P)$) [Bignel1970]. In a mixture of water with other gas, dry continuum $\alpha_{dry}(\nu, P)$ also should be considered (due to interactions between other molecules except water). $\alpha_{dry}(\nu, P)$ is contributed mostly by O_2 and N_2 CIA. Water self-continuum depends quadratically on water pressure and water foreign-continuum depends linearly on the product of water and foreign-gas pressures. Dry continuum is due to interactions between the rest molecules except water. It depends quadratically on the foreign gas pressure.

$$\alpha_{cont}(\nu, P) = \alpha_{self}(\nu, P) + \alpha_{foreign}(\nu, P) + \alpha_{dry}(\nu, P) = C_{self}(\nu)\frac{P_{H_2O}^2}{kT} + C_{foreign}(\nu)\frac{P_{H_2O}P_{foreign}}{kT} + C_{dry}(\nu)\frac{P_{foreign}^2}{kT}. \quad (1.16)$$

In this formula $C(\nu)$ ($cm^2 molecule^{-1} atm^{-1}$) are the self-, foreign-, and dry-continuum cross-sections. (see for instance **Fig. 4**). Usually water continuum exceeds dry continuum except when N_2 or O_2 band is located between H_2O bands as it will be demonstrated in Chapter 3 for O_2 continuum.

Both mono- and bimolecular absorption contribute to the continuum. The latter is included to the continuum as a whole, since it is not taken into account in monomer resonance spectrum models. Regarding monomolecular part, an “obvious” (and discussed from the beginning of continuum studies) continuum-related mechanism is far wings of the lines. Historically, the difference between the real line wing absorption and its model in the frame of the impact approximation is part of the continuum absorption. For the convenience of comparing continuum calculations with experimental

results obtained by different groups, for different foreign molecules and experimental conditions, a wing cut-off at 25 cm^{-1} frequency detuning from the line centre is typically used as standard. The pedestal (or "plinth") under the line (grey part in **Fig. 1.5**) is considered as a part of the continuum [Clough1989].

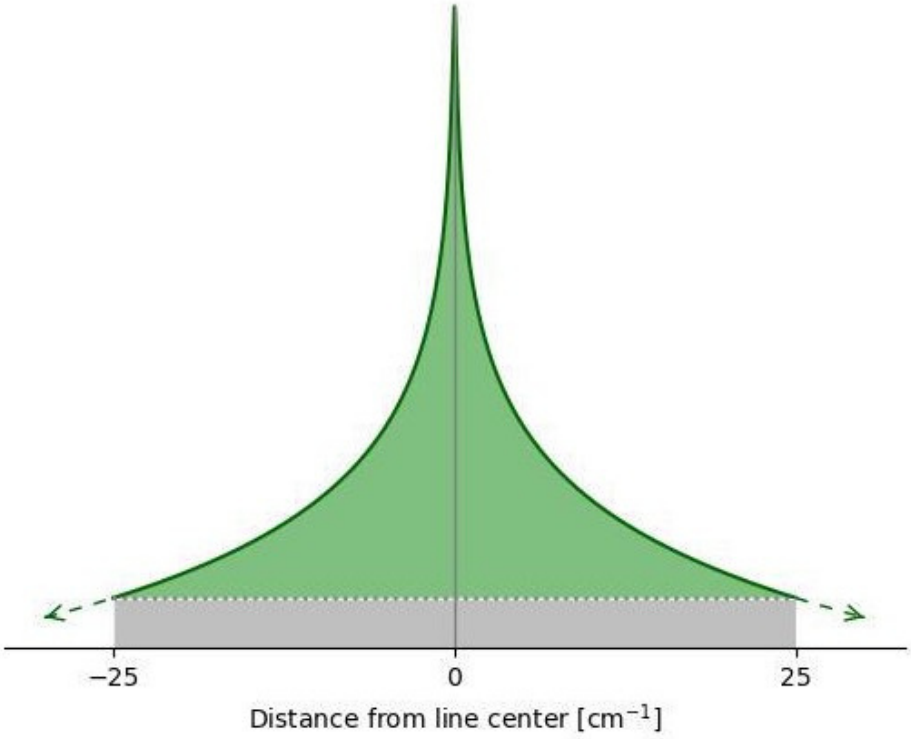

Fig. 1.5. (from [https://hitran.org/mtckd/])
Water line in a log scale. The part corresponding to resonance absorption is given by green area, "pedestal" shown by grey area.

Historically, "grass" of weak unknown resonance lines was discussed for a while as a possible continuum origin. This hypothesis was refuted with the advent of *ab initio* ro-vibrational spectra calculations with the precision similar to experimental measurements [Polyansky2012].

Thus, dominating mechanisms forming the continuum are known (resonance lines wings and bimolecular absorption, **Sections 1.1.1.2** and **1.1.2**). However, their relative contributions to the continuum are not yet calculated from first principles. In this sense, the nature of the continuum is still considered to be unclear.

1.1.4 Water continuum literature data review

Continuum absorption measurements are difficult due to its weakness, especially on the background of strong water monomer lines. This requires both highly sensitive spectrometers and a high stability of experimental conditions during measurements. Water vapour continuum measurements are especially challenging because of possible experimental biases due to surface

effects (adsorption, condensation) on optics and other parts of experimental setup and possible changing of water quantity during experiments.

The most relevant laboratory continuum studies are summarised in Table 1.1 (sorted in ascending order of the lowest frequency of the range of the measurements) with experimental technique, spectral range and temperature provided for each of them. Studies in the spectral range under consideration are highlighted by colour (red for far-infrared and blue for near-infrared) The measurements included in this thesis are highlighted in bold. It reflects a long history of continuum measurements from pioneering works by Liebe and Burch to large recent projects such as CAVIAR (Continuum Absorption at Visible and Infrared wavelengths and its Atmospheric Relevance) and series of work performed in Rutherford Appleton Laboratory (Didcot, UK) using FTS, Institute of Applied Physics RAS (Nizhny Novgorod, Russia) using resonator spectrometer with BWO (backward wave oscillator) and Laboratoire Interdisciplinaire de Physique in Grenoble by CEAS (cavity enhanced absorption spectroscopy).

Table 1.1

Previous experimental laboratory continuum studies

	Reference	Technique	T	Spectral interval, cm^{-1}	Subject
1	[Koshelev2011]	Resonator spectrometer	261–328	3.5–4.8	Self N_2-foreign
2	[Koshelev2018]	Resonator spectrometer	296	3.5–8.5	Self
3	[Liebe1987]	Resonator spectrometer	281-316	4.6	Self N_2, O_2, air foreign
4	[Kuhn2002]	Resonator spectrometer	296–356	5.1–11.7	Self N_2-foreign
5	[Bauer1998]	Resonator spectrometer	296-356	7.97	Self N_2-foreign
6	[Odintsova2017]	FTS	297	14–35 40–200	Self
7	[Burch1982]	Interferometer	296	14–50 350–800	Self
8	**[Odintsova2019]**	**FTS**	**296**	**15-35 50-500**	**Self**
9	[Podobedov2008]	FTS	293–333	20–90	Self N_2-foreign
10	[Podobedov2008II]	FTS	293–333	20–120	O_2-foreign
11	[Slocum2015]	Video-spectrometer	296	50	Self
12	**[Koroleva2021]**	**FTS**	**296**	**50-500**	**N_2-foreign O_2-foreign Air-foreign**
13	[Odintsova2020]	FTS	296, 326	70-700	Self
14	[Burch1984]	Interferometer	284, 296, 328	700-1200 2400-2800	Self N_2-foreign
15	[Baranov2012]	FTS	296-339	800-1230 2000-3300	Self N_2-foreign
16	[Baranov2008]	FTS	326, 339, 352, 363	800-1250	Self
17	[Cormier2002]	CRDS	294-297	931, 944, 969	Self

18	[Cormier2005]	CRDS	270–315	944	Self N_2-foreign
19	[Paynter2009]	FTS	296-351	1200-8000	Self Air-foreign
20	[Ptashnik2011II]	FTS	296-351	1200-8000	Self
21	[Ptashnik2013]	FTS	289, 318	1300-8000	Self
22	[Hartmann1993]	Spectrograph	500-875	1900-2600 3900-4600	Self
23	[Baranov2011]	FTS	311-363	1900-3500	Self
24	[Baranov2011II]	FTS	326-363	2000-3250	N_2-foreign
25	[Ptashnik2015]	FTS	287	2000-8000	Self
26	[Ptashnik2012]	FTS	350-430	2000-9000	Air-foreign
27	[Ptashnik2011]	FTS	293-472	2010-9550	Self
28	[Campargue2016]	CRDS, OF-CEAS	296-312	2283 4341-4367 4516-4532 7500-8300	Self
29	[Baranov2012II]	FTS	326-363	2400-2900	N_2-foreign
30	[Richard2017]	CRDS, OF-CEAS	296-325	2491 4435	Self
31	[Fleurbaey2022]	OF-CEAS	303-320	2853	Self
32	[Burch1985]	Interferometer		3000-4200	Self N_2-foreign
33	[Lechevallier2018]	CRDS, OF-CEAS	298-323 297.7	3007 4995-5007	Self
34	[Birk2020]	FTS	297, 342	3400-3900	Self
35	[Mondelain2015]	CRDS	297.5	4249-4257	Self Air-foreign
36	[Ventrillard2015]	OF-CEAS	296-323	4302-4723	Self
37	[Bicknell2006]	calorimetric-interferometry in air	298	4605	Self- and foreign (without separation)
38	[Vasilchenko2019]	CRDS	296	4720 5130	Self Foreign
39	[Ptashnik2004]	FTS	297. 342	5000-5600	Self
40	[Mondelain2013]	CRDS	296	5875-6450	Self
41	[Mondelain2014]	CRDS	302-340	5875-6665	Self
42	**[Koroleva2023II]**	**CRDS**	**294**	**8100-8500**	**N_2-foreign** **O_2-foreign** **Air-foreign**
43	**[Koroleva2022]**	**CRDS**	**294**	**8290-8620**	**Self**
44	[Simonova2022]	FTS	398, 431	8502-11100	Self
45	[Fulghum1991]	Calorimetric interferometry in N_2	303	9466	Self- and N_2-foreign (without separation)
46	[Reichert2007]	CRDS	278, 296	10611, 10685	N_2-foreign
47	[Aldener2005]	Pulsed CRDS	295	11495	Self- and N_2-foreign (measured upper limit)
48	[Tikhomirov2006]	Photoacoustic	295	14397 - 14401	N_2-foreign

These data revealed that the shape of the continuum represents the envelope of H_2O monomer spectrum with maxima within ro-vibrational bands and minima in the transparency windows between them (**Fig. 1.6**). Part of these studies performed at various pressures confirmed the self-continuum

quadratic pressure dependence and foreign-continuum linear pressure dependence on the product of water and foreign gas partial pressures. This was not the case of some studies which are led to the publication of conflictive results as illustrated by the disagreement of the CAVIAR cross-section values in the transparency windows, compared to other sources (**Fig. 4**).

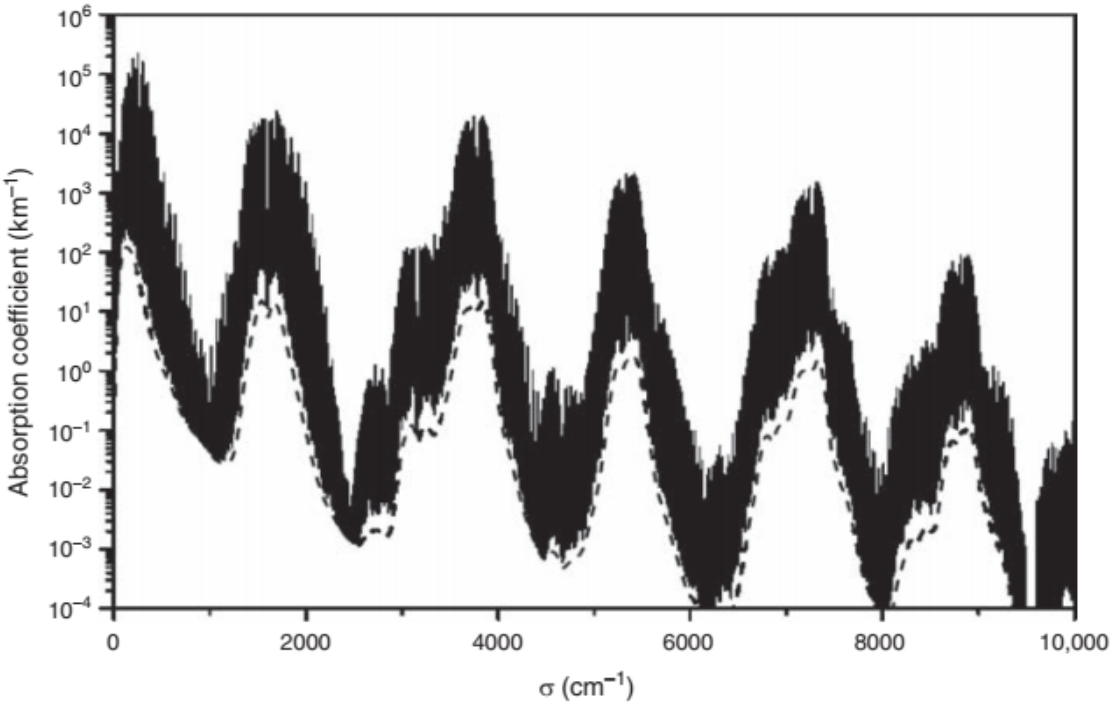

Fig. 1.6. (from [Hartmann2021])
Calculated absorption for 1% H_2O in air at 296K and 1 atm. Solid line is the total absorption, dashed line is the continuum for a cut-off distance of 25 cm^{-1}

Self-continuum has a strong negative temperature dependence which is approximated empirically by a power function of temperature $(T/T_0)^n$ where $T_0 = 296\ K$ and n is the temperature exponent [Liebe1987, Kuhn2002, Podobedov2008, Koshelev2011, Odintsova2020]. Also, a calculated water dimer temperature dependence $\exp(D_0/kT)$ [Leforestier2014] can be used assuming that the continuum is primarily due to the absorption of the water dimer. (D_0 is the dissociation energy of the water dimer, D_0 = 1105(10) cm^{-1} [Rocher-Casterline2011]). It works well in the 4.0 and 2.1 μm transparency windows for self-continuum measured by CEAS and CAVIAR [Richard2017, Lechevallier2018, Ventrillard2015], but dimer temperature dependence is not confirmed for the self-continuum in the 1.6 μm window [Mondelain2014].

Foreign continuum is known to be less sensitive to the temperature and in some frequency ranges it could be considered temperature independent [Vasilchenko2019, Mondelain2020]. In far-infrared range foreign-continuum temperature dependence could be approximated by a power function [Podobedov2008].

Most of the experiments were performed using either interferometers or cavity enhanced absorption spectroscopy techniques for continuum absorption measurements as will be discussed in **Section 1.2.**

Prior the work presented in this thesis, the continuum has been measured practically in the whole spectral range up to 8300 cm^{-1} at different atmospherically related temperatures (**Fig. 3**). The exceptions were the gap in the far-infrared (200-350 cm^{-1}) and the near-infrared range above 8300 cm^{-1}. This work fills these ranges with experimental data.

1.2 Experimental techniques

The absorption spectrum of water vapor was studied using a commercial high-resolution Fourier-transform spectrometer (FTS) with synchrotron radiation as a light source in the far-infrared range and state-of-art cavity ring down spectrometer (CRDS) in the near-infrared range. This chapter presents operational principles for these spectrometers both for water line parameters and continuum measurements. The details of each experiment are given in **Section 2.1** (for line parameters) and in **Section 3.2.1.** and **3.3.1** for continuum measurements.

Both FTS and CRDS provide absolute absorption coefficients. Absorption is measured as a difference of light intensity transmitted through the cell with and without gas of interest (with the same spectrometer alignment in both cases). However, the empty cell recordings are not necessary for line parameters measurements with CRDS as variations of such spectra are much wider than narrow water lines.

Cavity ring down spectroscopy (CRDS) with single-frequency CW laser (coherent radiation) is a highly sensitivity techniques developed in the 90's [Romanini1997, Romanini2014]. CRDS frequency range is thus limited by laser tuning range [Kassi2012]. FTS operates with wide-band radiation sources such as a tungsten lamp, a Xenon arc-lamp, etc. The specificity of this work is using a SOLEIL synchrotron radiation. This brings the FTS advantage of being capable of performing spectra recordings over a broad frequency range. Globar is used as an additional light source for foreign-continuum measurements. However, any changes in the light source intensity during interferogram recording could spoil FTS spectra while CRDS does not depend on fluctuations of light intensity.

The use of a multi-pass cell with an effective pathlength of about 150 m in the case of FTS and a resonator with super-reflective mirrors leading to equivalent path length of 10 km or more with CRDS allows achieving high sensitivity in both cases. (For CRDS, it is combined with the compactness of the setup). Spectrometer sensitivity is also affected by the noise level, which is much smaller in CRDS spectra. The combination of these factors leads to a sensitivity difference of 5 orders of magnitude in the two spectral ranges under consideration. The weakest lines which can be measured by FTS and CRDS have an intensity of about 10^{-26} and 10^{-31} cm/molecule, correspondingly. In addition, the necessity of frequency scale calibration and uncertain apparatus function complicate the data treatment in FTS.

Section 1.2 gives a general description both FTS and CDRS spectrometers, although monomer lines and continuum measurements required different conditions. These differences are given in more detail at the beginning of Chapters 2 and 3 for water lines and continuum, respectively. **Section 1.2** is thus divided in two parts. The first part (1.2.1.) is devoted to the FTS experimental setup used at SOLEIL synchrotron, the choice of optimal spectral resolution corresponding to experimental conditions and baseline stability problem. The second part (**Section 1.2.2.**) is dedicated to the CRDS spectrometer.

1.2.1 Far-infrared range

Despite the recent semiconductor devices progress, synchrotrons remain one of a few wide-range radiation sources operating in the "terahertz gap" region with sufficient spectral brightness to measure the continuum at usual conditions. Spectra were recorded using FTS spectrometer on the AILES beamline of the synchrotron SOLEIL facility located on the Plateau de Saclay in Saint Aubin, Essonne. Coupling FTS with synchrotron radiation allows increasing the spectrometer sensitivity up to 15 times compared to standard thermal radiation sources such as globar. Thus, synchrotron radiation with sufficient spectral brightness and a high sensitivity of the spectrometer in a wide frequency range makes the AILES beamline unique for studying the molecular spectra in the far infrared range.

Table 1.2 summarised all the performed series of measurements. Note that each series of measurements had several goals (for example, self-continuum temperature dependence was determined using spectra from series #2 [Odintsova2020] and water spectra with different isotopic abundances were recorded during series #3) but Table1.2 indicates only what was included in the presented work.

Table 1.2.

Experimental campaigns in SOLEIL

Series	Project №	Duration	Subject
#1	20180347	06.10.2017 – 11.10.2017 (6 days)	Self-continuum measurements for natural and ^{18}O-enriched water
#2	20180347	10.12.18 – 19.12.18 (9 days)	Water foreign-continuum measurements for humidified nitrogen, oxygen and air
#3	20210051	28.09.21 – 04.10.2021 (6 days)	Water line positions determinations.

1.2.1.1. Fourier transform spectrometer

Fourier transform spectroscopy is based on interferogram recording with a Michelson interferometer. The incoming wide-range incoherent light is divided by a beam splitter. Two resulted

beams are recombined and detected after one of beams passed through the gas cell. Spectra are obtained by taking a Fourier-transform of the recorded interferogram (**Fig. 1.7**).

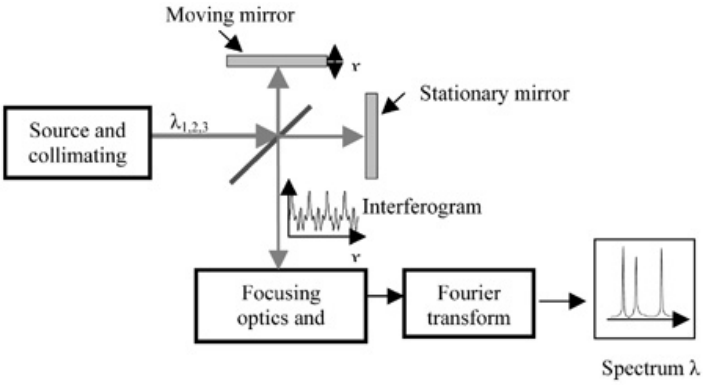

Fig. 1.7. (from [https://spie.org/publications/tt61_123_fourier_transform_spectrometers?SSO=1])
A Fourier transform spectrometer using Michelson interferometer.

Experimental data were acquired with Bruker IFS-125HR interferometer equipped with a multipass White type gas cell. The schematic view of the cell with interferometer is presented in **Fig. 1.8** [https://www.synchrotron-soleil.fr/en/beamlines/ailes]. This cell allows choosing total optical pathlength from about 10 to 150 m. To increase the spectrometer sensitivity for measuring very weak water lines with intensities about 10^{-26} cm/molecule and the continuum, the maximum available pathlength L = 151.75±1.5 m was chosen. It corresponds to 60 passes between mirrors separated by 2.52 m and about 0.5 m of space between the 50 μm thick polypropylene film windows.

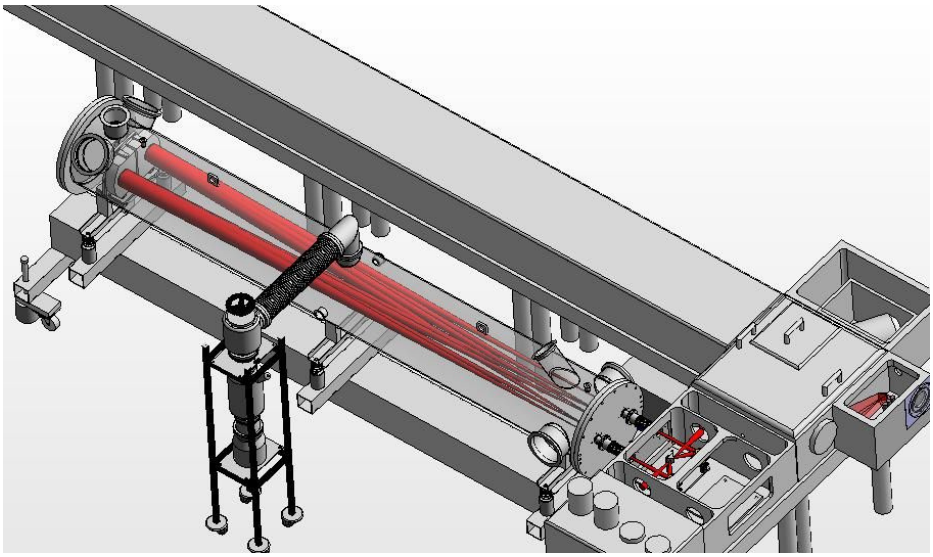

Fig. 1.8. (from [https://www.synchrotron-soleil.fr/en/beamlines/ailes])
Schematic view of the long pass White cell with the interferometer. The modulated by molecular absorption beam (in red) is undergoing multiple reflections before being redirected toward the detector.

Coherent (in the subterahertz frequency range 14-35 cm^{-1}) and incoherent (in the superterahertz range 50-700 cm^{-1}) synchrotron radiation modes were used. Globar was used as a complementary frequency source during the preparation stage of foreign-continuum measurements and for recording a series of spectra with wet nitrogen when synchrotron radiation was not available. 4 K cooled Si bolometer was used as a detector.

Figure 1.9 shows a comparison of the light power transmitted through the cell with water vapour or wet gas (studied spectrum) *I(ν)* and reference spectrum (baseline) with the empty cell or cell filled with non-absorbing gas $I_0(\nu)$ (to be discussed in **Section 1.2.1.3**). One order of magnitude difference between synchrotron and globar power illustrates the advantage of using synchrotron radiation. The experimental transmittance and absorption coefficient are given by:

$$Tr(\nu) = \frac{I(\nu)}{I_0(\nu)}. \tag{1.17}$$

$$\alpha(\nu) = -\frac{1}{L} ln\big(Tr(\nu)\big) \tag{1.18}$$

The pressure was measured just before and just after each spectrum recording by a capacitance gage (Pfeiffer 10, 100 and 1000 mbar full range with manufacturer stated uncertainty of 0.25% of reading). Temperature was permanently monitored by two thermo-sensors PT100 attached to the surface of the gas cell.

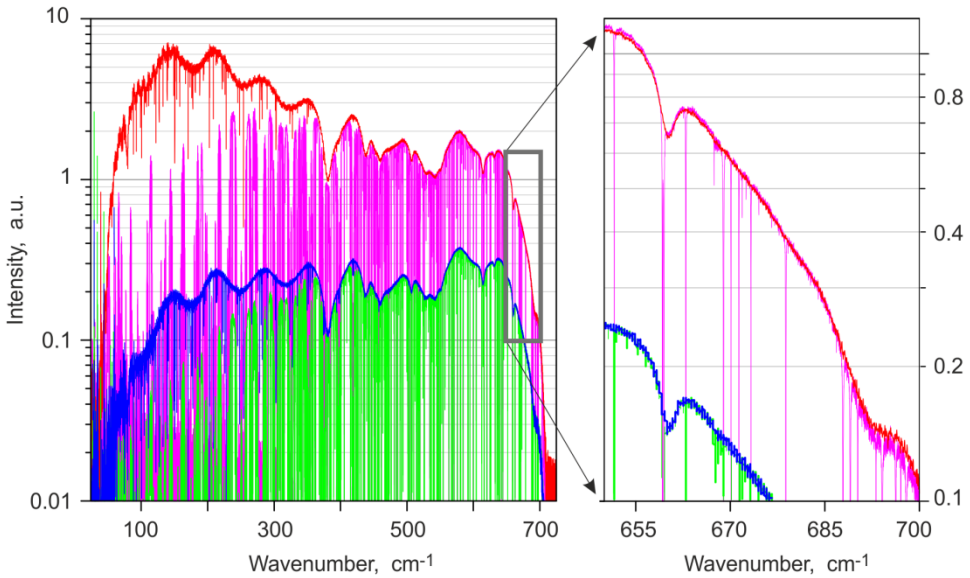

Fig. 1.9.

Typical example of raw FTS spectra for a mixture of 96 mbar of nitrogen and 4 mbar of water vapour (pink) recorded using the synchrotron radiation and corresponding reference spectrum recorded with 100 mbar of pure N_2 (red). Similar recordings with the globar source (green and blue, respectively). The right panel shows a zoom of the 655-700 cm^{-1} region.

1.2.1.2. Spectral resolution and choice of experimental conditions

The transmittance *Tr* and absorption coefficient *α(ν)* are related by:

$$Tr(\nu) = e^{-\alpha(\nu)L} \oplus f_{app}, \quad (1.19)$$

$$f_{app}(\nu) = 2 * MOPD * sinc(2\pi\nu * MOPD) \quad (1.20)$$

where f_{app} is apparatus spectral resolution function and *MOPD* is maximum optical path difference. Thus, the spectral resolution is limited by the apparatus function. Unperturbed spectrum from the Fourier transformed interferogram requires the infinite integration limits, *i.e.* for optical path differences varying from 0 to ∞. Real interferometers have finite boundaries. The movable mirror can be shifted only to the limited value of *MOPD*. The instrument-limited resolution represented by the *sinc* function in eq. (1.20) produces oscillations, which look like lines in dense spectra. The resolution R_{FTS} related to *MOPD* is defined as $R_{FTS}=0.9/MOPD$. In our recordings, the highest MOPD was 882 cm for a resolution of 0.001 cm^{-1} resolution. Therefore, scans with higher resolution take more time (for comparison, 200 scans at 0.02, 0.002 and 0.001 cm^{-1} resolution took about 15 minutes, 5 hours and 8 hours, correspondingly). At the same time, the signal-to-noise ratio increases with an increase the number of averaged spectra, $N_{sp,}$ as $\sqrt{N_{sp}}$. Thus, multiple repetition of scans is required to increase sensitivity.

In general, the spectral resolution is chosen based on the following*: (i)* sufficiently high to resolve the studied spectral features, *(ii)* as minimum as possible influence of the apparatus function (1.18), *(iii)* compromise between high sensitivity and recording time.

The change of line shape due to apparatus function is least noticeable when the width of the lines exceeds the width of the apparatus function. At low resolution, recorded lines look “blurry” and become broader with less peak height at low resolution. It requires more complicated line fit procedure considering apparatus function influence. That is why a high resolution of about 0.001 – 0.002 cm^{-1} is required for being able to resolve the shape of narrow water lines at pressures about several Torr. **Figure 1.10** shows the Doppler and collision line widths for three different pressures (0.1, 1 and 5 Torr). At the lowest pressure, the lines are much narrower than the highest possible resolution 0.001 cm^{-1}, and the line shape is determined mainly by the apparatus function. This limits the accuracy of line intensities retrieving (see **Section 2.3.2**). At 1 Torr pressure, the line widths become comparable to the spectral resolution 0.001 cm^{-1}. 5 Torr pressure allows you to choose a smaller resolution 0.002 cm^{-1}.

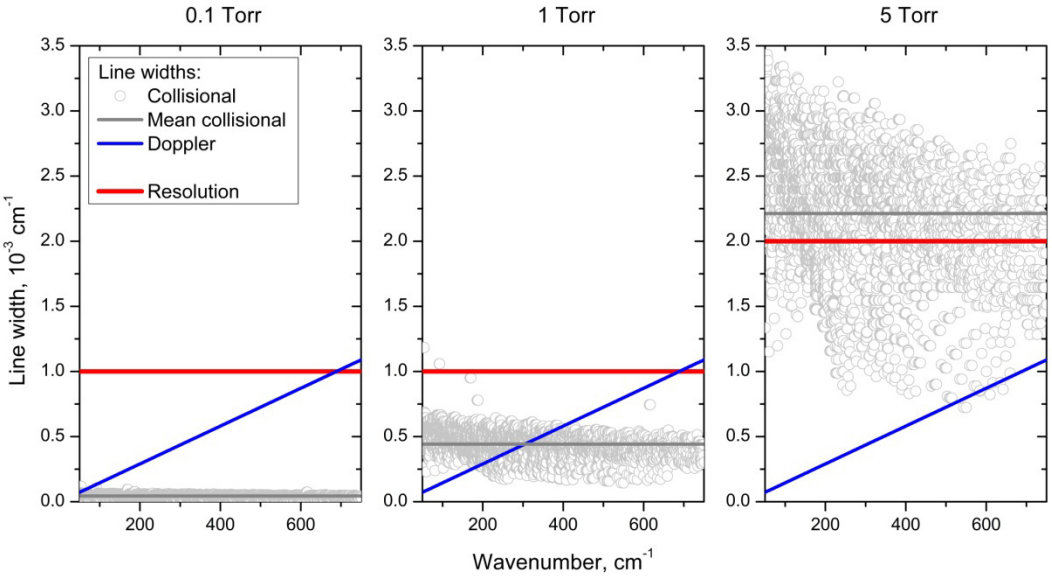

Fig. 1.10.

Relation between line width and spectral resolution for different gas pressures

Water continuum has smooth frequency dependence and was retrieved in microwindows of transparency between resonance lines. High resolution is not necessary and thus it was limited to 0.02 cm^{-1}. In that case it is much less than the characteristic width of the spectrum of the continuum and the apparatus function influence is negligible. Using a lower resolution of 0.02 cm^{-1} allowed increasing the number of averaged interferograms in order to increase sensitivity.

1.2.1.3. Baseline stability

Although not affecting the determination of water line parameters, even minor baseline variations during experiments could be a cause of significant errors in the retrieved (weak) continuum absorption. That is why the baseline stability is of crucial importance for the continuum absorption study. To check that, a number of additional reference spectra were recorded in both synchrotron modes.

For the coherent synchrotron mode, the FTS stability was tested from a detailed analysis of several reference spectra and with the 16 mbar water spectra recorded successively four times without any change in the spectrometer regime and data acquisition scheme. The very good coincidence of these series of recordings (down to the noise level, corresponding to absorption 10^{-6} cm^{-1}) confirmed the long-term (within at least 10-12 hours) stability of the experiment. For comparison, continuum absorption was in order of 10^{-5}-10^{-4} cm^{-1}.

In standard synchrotron mode, additional reference spectra recordings with an empty cell and nitrogen also showed excellent repeatability, but at pressures higher than 100 Torr a periodical spectral structure was observed at frequencies above 300 cm^{-1}. It could not be attributed to gas absorption. In this frequency range nitrogen does not have resonance lines and N_2 continuum is negligible. This

periodic structure appears because of the deformation of the input and output cell windows made of the 50-μm polypropylene film. The reproducibility of this deformation allows reducing its influence.

An additional check of the FTS stability at high pressures was performed during the experiment preparation with a globar as a light source. The pressure of dry gas was increased step-by-step to the maximum value (up to 1000 mbar) and then decreased with the same step. That was repeated several times for nitrogen, oxygen and air. (Typical spectra are shown in **Fig. 1.11.**)

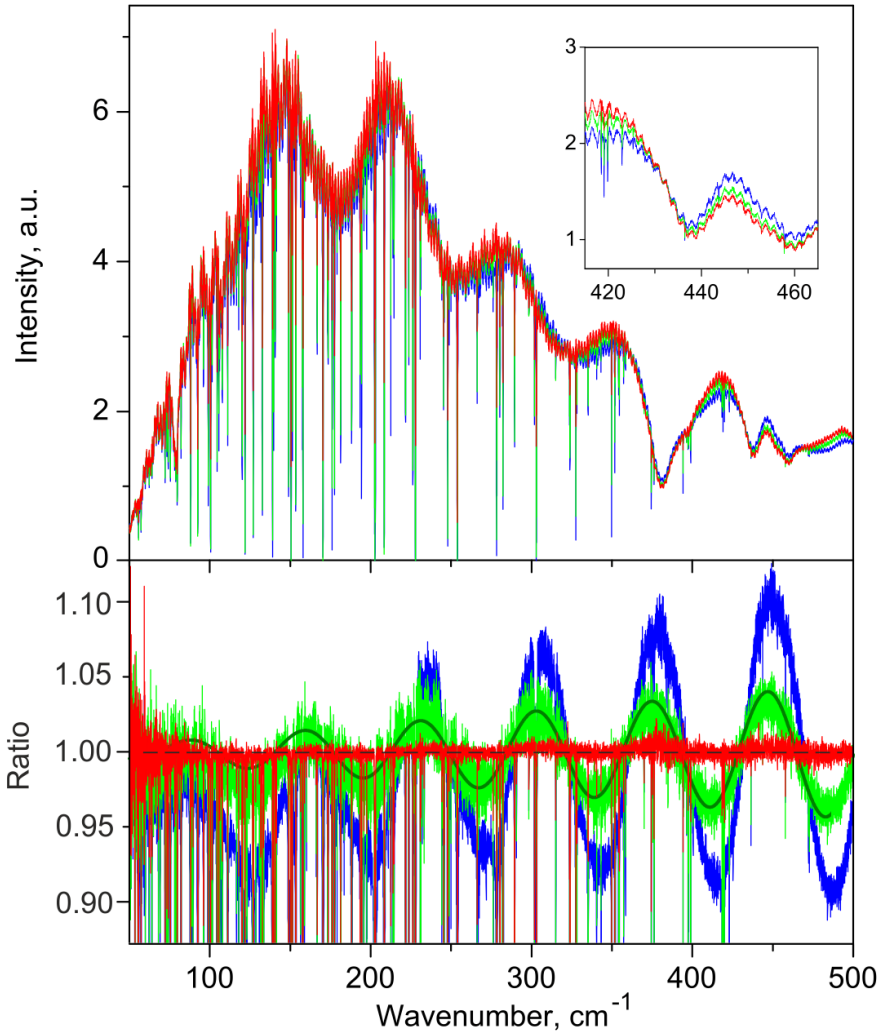

Fig. 1.11.

Upper panel: reference spectra recorded with a globar as a light source with dry nitrogen at pressures of 800 (blue), 300 (green) and 100 (red) mbar. Narrow lines are due to water vapour presence. The insert shows a zoomed-in fragment of the spectra. *Lower panel*: Ratio of reference spectra recorded at 800 and 0 mbar (blue), 300 and 0 mbar (green); ratio of spectra recorded at 100 mbar at filling and pumping stages of the experiment (red); smooth black curve represents fitted model function F_1.

The ratio of spectra recorded with non-zero pressure and for empty cell can be approximated by a following periodic function: $F_1=a_0 v\cos(a_1 v+a_2)$. a_0, a_1, a_2 are pressure dependent and behave similarly for different gases. At pressures less than 400 mbar, the film deformation is elastic and changes of baseline parameters a_0, a_1, a_2 are reproducible with consecutive filling and pumping the gas cell. At a higher pressure, the film deformation becomes inelastic that leads to unpredictable changes of a_1 and irreproducibility of a_0 changes with increasing and decreasing pressure, but after pumping a_0 slowly returns to initial value (see supplementary materials of [Koroleva2021] for more details). The maximum pressure value was limited to 400 mbar to reduce the influence of these deformations. Reference spectra were recorded before and after each series of wet gas spectra recording at the same total pressure as spectra with pure water vapor.

1.2.2 Near-infrared range. Cavity Ring-Down Spectrometer

In the near-infrared range (8040-8630 cm^{-1}) the Cavity Ring-Down Spectroscopy techniques [Kassi2012, Konefal2019] was used for spectra acquisition. This method based on measurements of purely exponential radiation decaying process (ring down) in a high finesse optical cavity (CRDS gas cell).

The sketch of experimental setup is presented in **Fig. 1.12**. This was applied both for line parameters and continuum measurements. An external cavity diode laser (ECDL, Toptica fiber-connected DL pro, 1200 nm) was used as a coherent light source. The laser light is injected to the 1.4 m long stainless steel optical cavity with 11.5 mm inner diameter through a mirror with a reflection coefficient R > 99.99 % by the single mode fiber maintained light polarization that provides better reproducibility. The reflectivity of the mirrors corresponds to empty cell ring down times varying from 120 to 360 μs depending on the wavelength. The frequency tuning of the laser and then the coincidence (resonance) between the laser frequency and one of the CRDS cavity modes are achieved by modulating the rear mirror of the cavity mounted on a piezoelectric transducer (PZT), over the free spectral range of the cavity (about half the wavelength). When the resonance is reached and the cavity is filled with photons, the injection of the laser light is interrupted by an acousto-optic modulator (FCM series from Intra Action, 40 MHz, 0.5 W RF). The decay of photons power leaking from the cavity proportional to $\exp(-t/\tau_r)$ is detected by an InGaAs PIN photodiode and ring-down time τ_r characterizing this exponent is fitted.

The ring-down time is determined by the radiation power losses associated with the resonator (including diffraction losses and losses for reflection and passage of radiation through mirrors) and losses due to the absorption of the gas filling the resonator. Also, in the frequency range under consideration, the losses due to Rayleigh scattering become significant.

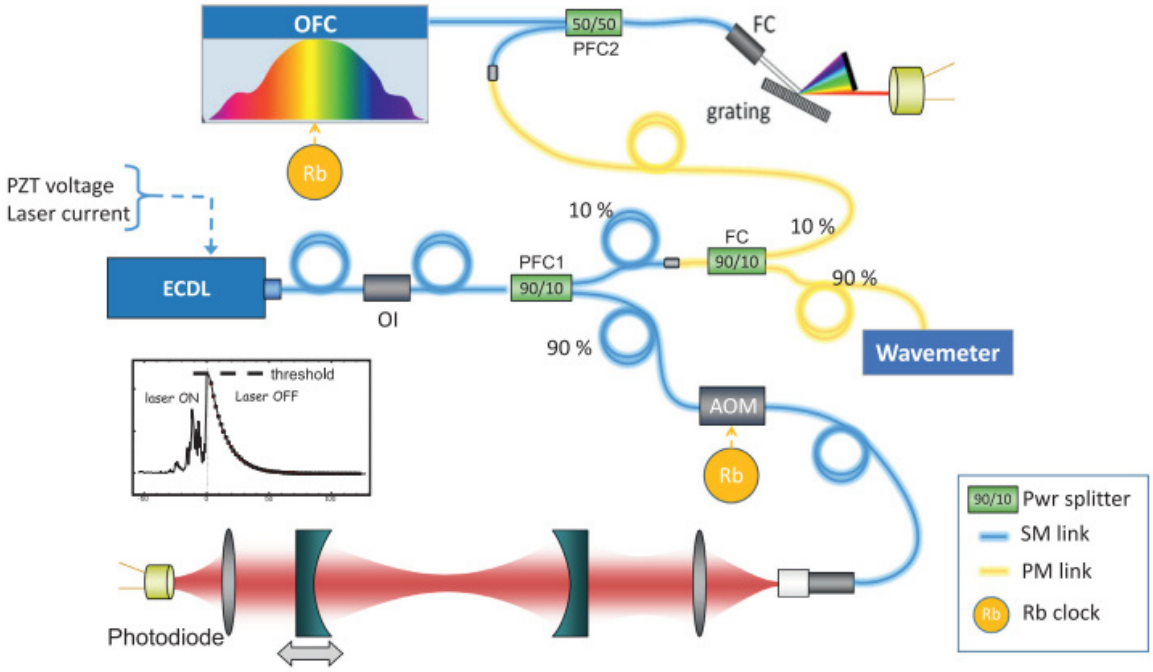

Fig. 1.12. (from [Konefał2019])

Scheme of the CRD spectrometer coupled with the self-referenced optical frequency comb (OFC). The different components include an external cavity diode laser (ECDL), an optical isolator (OI), a fiber coupler (FC), two polarization maintained fiber couplers (PFC1,2), the OFC and acousto-optic modulator (AOM) referenced to a GPS referenced rubidium (Rb) clock.

The absorption coefficient, *α(ν)*, is determined directly from fitted ring down time as a function of laser frequency through equation (1.21):

$$\alpha(\nu) = \frac{n}{c\tau(\nu)} - \frac{n_0}{c\tau_0(\nu)}, \tag{1.21}$$

where c is the speed of light, n is the refractive index of the gas, τ is the ring down time of cell with gas. n_0 and τ_0 reproduce the refractive index and ring down time of empty cell for all recordings except for foreign continuum measurements. In that case, n_0 and τ_0 correspond to the refractive index and ring down time of the cell filled with dry gas. It allows subtracting the impact of not only the cell, but also CIA and Rayleigh scattering. Thus, in all the cases under consideration $\alpha(\nu)$ corresponds to the water-related part of absorption only.

For resonance spectra recording the spectrometer was coupled with a self-referenced frequency comb (SRFC, Model FC 1500-250 WG from Menlo System) providing accurate frequency value for each ring down event. Water continuum has relatively smooth frequency dependence that enables using wavelength meter (HighFinesse WSU7-IR, 5 MHz resolution, 20 MHz accuracy over 10 hours) for direct frequency measurements (although with an accuracy two orders of magnitude lower than with the comb).

The gas cell made of stainless steel was covered with an insulating foam tube and installed in a protective Plexiglas enclosure to make the temperature in the cell more stable. One temperature sensor

(TSic 501 from IST, ±0.1 K accuracy) was fixed under the insulation on the external wall of the cavity. The temperature was measured continuously during all the measurement campaign and did not change more than by 1 K during each series of measurements.

Total gas pressure in the cavity was controlled incessantly by two pressure gauges (10 and 1000 Torr full scale, from MKS Instruments, 0.25% of reading uncertainty). All the measurements were performed in regime of (slow) flow adjusted manually with a downstream needle valve for minimizing the adsorption/desorption effects.

For foreign-continuum measurements, commercial water vapour generator from Omicron Technologies was used [Fleurbaey2022] to mix water vapor produced by a temperature regulated membrane system with nitrogen, oxygen or air. The water concentration was fixed at 10000 ppm (1%) and was monitored continuously by the drew point measurements with chilled mirror hygrometer (Model S8000 from Mitchell). The pressure and the speed of the gas flow was set up by the mass flow and pressure controllers (Area model, FC-R7800 series from Hitachi Metals Ltd. and Model IQP-700C from Bronkhorst, correspondingly).

Conclusions

In this first section of the chapter, the theoretical basis of this work has been presented It considers two main approaches to the total absorption modelling: physically based (as sum of mono- and bimolecular absorption) and empirical (as sum water lines and continuum). The connection between these approaches is discussed. The continuum measurements have been briefly reviewed. The empirical approach is used in next two chapters which presents water line parameters and continuum measurements. However, physically based approach is applied in **Sect. 3.5.1** for continuum absorption modelling in the far-infrared.

The importance of consistency of the resonant spectrum model (line list + line profile + line parameters + line wings approach) and the continuum is underlined for a correct total absorption modelling and for interpreting the physical origin of the continuum. More details about it are given in **Sect. 3.4.2**.

The second section of the chapter is devoted to experimental techniques used in this work, namely CRDS and FTS. The choice of these instruments is justified and principles of operation are described. Special attention is paid to the apparatus function and the baseline stability of the Fourier spectrometer as factors affecting the accuracy of determining the continuum and (in the case of an apparatus function) spectral lines parameters.

Chapter 2. The rovibrational spectrum of water vapor: new measurements and validation test of databases in the far- and near-infrared ranges

This chapter is devoted to the experimental study of H_2O line positions and line intensities in the far-and near-infrared ranges. This information is the basis for the resonance spectrum modelling and a prerequisite for the continuum retrieval from experimental spectra (together with the line profile parameters).

In the far-infrared range, the measurements were performed at SOLEIL synchrotron facility using a FTS spectrometer (see **Sect. 1.2.1**) in the frequency range 50-720 cm^{-1}. In the near-infrared (8040-8633 cm^{-1}) the data were recorded with CR-CRDS spectrometer (see **Sect. 1.2.2**).

Figure 2.1 presents the HITRAN2020 line list overview. It illustrates that water spectrum in far-infrared range is in several order of magnitude more intense than in near-infrared and thus intensity ranges are very different in these two regions. Despite the fact that the data were obtained using very different experimental techniques at different pressures, the results were processed in a similar way. This allows to combine two different studies into this chapter.

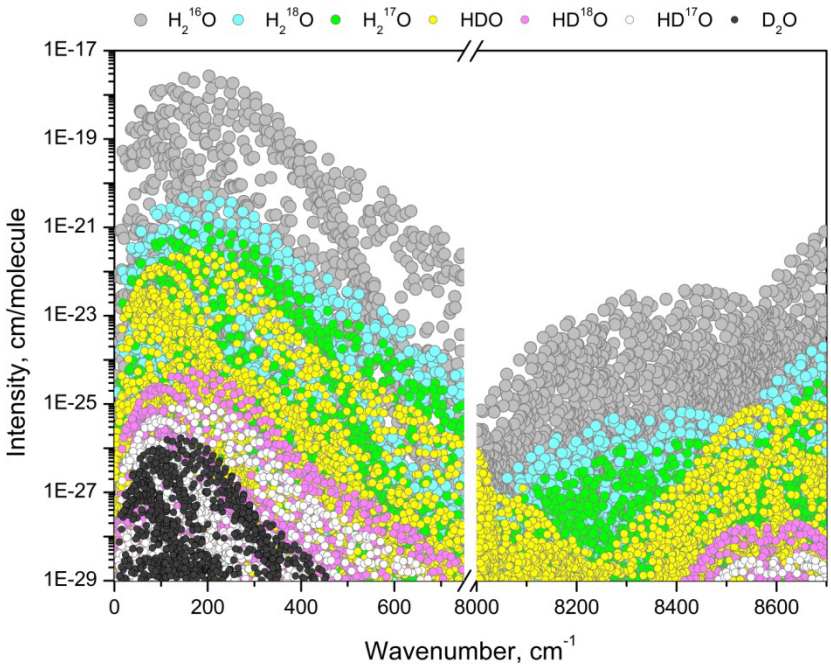

Fig. 2.1.

HITRAN2020 line list overview

HITRAN claimed accuracy of line positions is better than 10^{-5} cm^{-1} for some lines, which is close to standard uncertainty of FTS spectra in the far-infrared range, although some lines are given with 0.1

cm^{-1} uncertainty. As for the intensities, HITRAN guarantees its accuracy within 10% for 68% of the lines in frequency range 50-720 cm^{-1} (including the weakest lines). In the range of our CRDS measurements (8040-8633 cm^{-1}) it is the case for 62% of the lines with intensities higher than 10^{-28} cm/molecule. Nevertheless, even in the range of the H_2O rotational band, recent high sensitivity study of water vapor spectra [Mikhailenko2020II] have shown the possibility and necessity of significant refinement of the available information (**Fig. 2.2**). Measuring new (never observed before) lines and checking the accuracy of the positions of previously measured ones will allow for correcting of energy levels values (since part of them is determined on the basis of the Ritz principle using information about line positions). Note that the energy levels involved in the rotational band transitions in the far-infrared range belong to the ground or first vibrational states and are thus lower energy levels of a large fraction of transitions observed in higher energy spectral regions. The obtained results for this range thus impact spectroscopic databases far beyond the considered FIR spectral range.

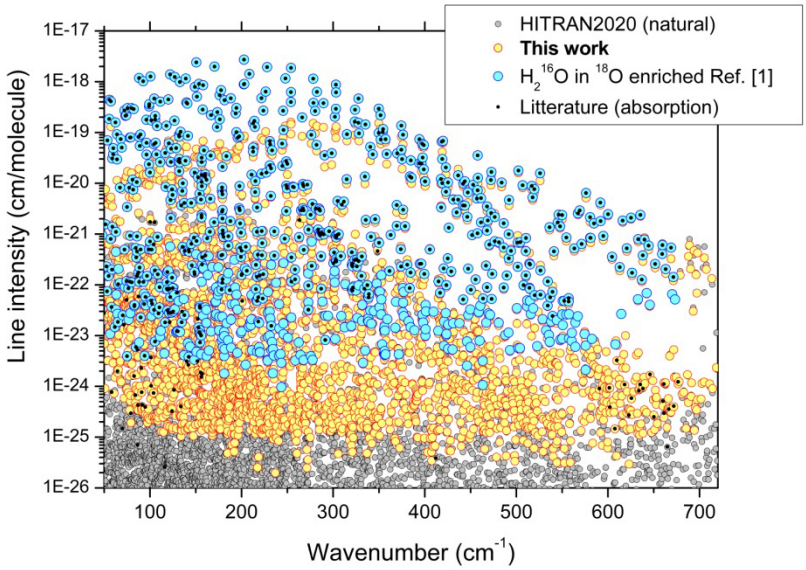

Fig. 2.2.

Overview of different line lists for water vapor between 40 and 720 cm^{-1}. Comparison of presented results (yellow dots) to (i) previous measurements available in the literature by absorption spectroscopy (black dots, see **Sect. 2.3.1**), (ii) $H_2{}^{16}O$ transitions identified in the spectrum of ^{18}O enriched water recorded at SOLEIL synchrotron in [Mikhailenko2020II] (blue dots), (iii) the HITRAN2020 line list (gray dots)

In the near-infrared range, previous H_2O resonance spectrum measurements [Campargue2015] were performed in the frequency range 7911-8337 cm^{-1} with a CRDS spectrometer but without the use of frequency comb (**Fig. 2.3**). New measurements with CR-CRDS is thus expected to increase the line positions accuracy. At the higher frequencies of the range of interest (8337-8633 cm^{-1}) only FTS measurements are available [Régalia2014], so a considerable number of new lines is expected to be detected thanks to the CRDS spectrometer high sensitivity in comparison with the FTS technique.

In both frequency ranges, the comparison with literature data provides a validation test of spectroscopic databases. Several line lists (HITRAN, W2020 and [Coudert2014] which is one of important source of $H_2{}^{16}O$ line positions for HITRAN and GEISA databases) will be considered.

The first part of this chapter outlines experimental details and conditions for spectra recordings in both frequency ranges. The second part is dedicated to the treatment of the recorded FTS and CRDS spectra including fit procedure and transition identification, which are very similar for both spectral ranges. The third part presents the comparison of obtained results with literature data.

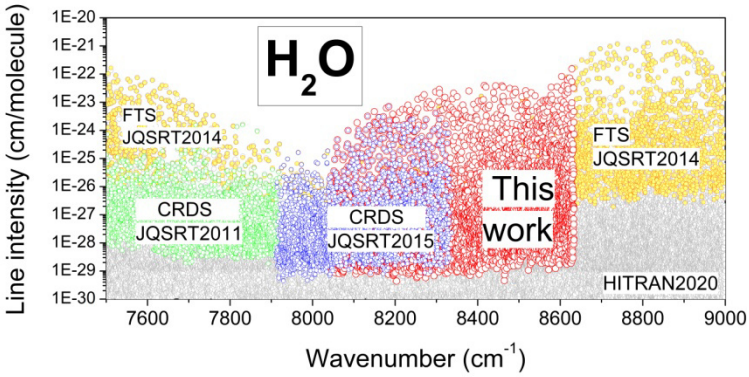

Fig. 2.3.

Overview of the water vapor spectrum between 7500 and 9000 cm^{-1}. Experimental observations are superimposed to the HITRAN2020 line list. The present study (red open circles) extends to higher energy our series of previous CRDS studies (alternate green and blue circles) [Mikhailenko2011, Campargue2015]. The line list elaborated by Régalia et al. from a series of FTS spectra [Régalia2014] is also plotted for comparison (yellow dots).

2.1 Experimental conditions

The spectra of water vapour with natural isotopic abundance were recorded at a room temperature. Far-infrared spectra (50-720 cm^{-1}) were recorded on the AILES beamline of the synchrotron SOLEIL facility in late September 2021 (experimental campaign #3 in **Table 1.2**) with help of Olivier Pirali and Alain Campargue.

Near-infrared spectrum was recorded by Samir Kassi at Laboratoire Interdisciplinaire de Physique in Grenoble, prior to my arrival at LIPhy. Note that during the course of my PhD, I performed myself very similar CRDS recordings with water highly enriched in ^{17}O. The analysis of such spectra is very time consuming. This is why in my thesis, only the results of the analysis of the natural water CRDS spectra is presented. The analysis of the ^{17}O enriched spectra remains to be done.

For minimizing the impurities influence the double distilled natural water sample was frozen and liquefied several times prior to measurements. The high sensitivity of the used CRDS spectrometer

allows to detect lines of minor H_2O isotopologues ($H_2{}^{18}O$, $H_2{}^{17}O$, HDO, $HD^{18}O$, $HD^{17}O$) in both frequency ranges.

In the far-infrared range FTS recordings were performed at five pressures up to 7 mbar with maximum available optical pathlength of 151.75 m. The experimental setup description is given in **Sect. 1.2.1**. Experimental conditions are summarised in Table 2.1. Spectra were recorded at the maximum available resolution of 0.00102 cm^{-1}, except the 7-mbar spectrum, where pressure broadening allowed to use a 0.002 cm^{-1} resolution. The number of co-added spectra ranges between 200 and 480 (200 spectra corresponds to about 10 hours acquisition time at 0.001 cm^{-1} spectral resolution or 5 h at 0.002 cm^{-1} resolution). The baseline spectra have smooth frequency dependence and were recorded with a resolution of 0.05 cm^{-1}.

Table 2.1 Experimental conditions for obtaining five FTS spectra of natural water under analysis recorded at temperature 295.5 K in the frequency range 50-720 cm^{-1}.

Spectrum nb	Sample	Pressure	Resolution, cm^{-1}	Nb of scans
#1	Empty cell	≈ 1.28 mTorrr	0.001	320
#2	Baseline **Sample**	Pumping on the cell **≈ 0.060 Torr**	0.05 0.001	200 400
#3	Baseline **Sample**	Pumping on the cell **≈ 0.86 Torr**	0.05 0.001	200 480
#4	Baseline **Sample**	Pumping on the cell **≈ 5.25 Torr**	0.05 0.002	200 280
#5	Empty cell	≈ 0.12 mTorr	0.001	220

Examples of "raw" FTS spectra recorded with empty cell (reference spectra) and spectra #3 and #4 are shown on **Fig. 2.4**. This figure illustrates the large dynamics of intensities of lines visible on recorded spectra. Lines visible at empty cell recordings (#1 and #5 spectra) become saturated at 5.25 Torr, but the weaker lines are visible at high pressure.

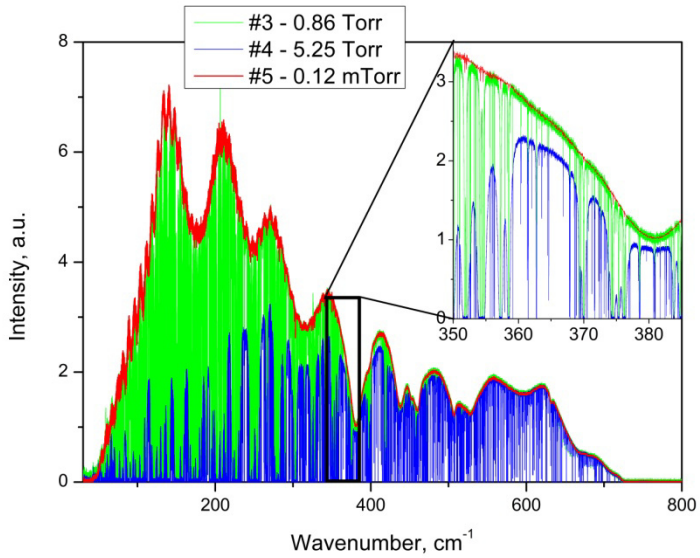

Fig. 2.4.

"Raw" FTS spectra #3, #4 and #5.

Transmittance was calculated from these spectra using formula (1.17). An example of the experimental transmittance is presented in **Fig. 2.5**. The noise equivalent absorption is on the order of 10^{-7} cm^{-1}.

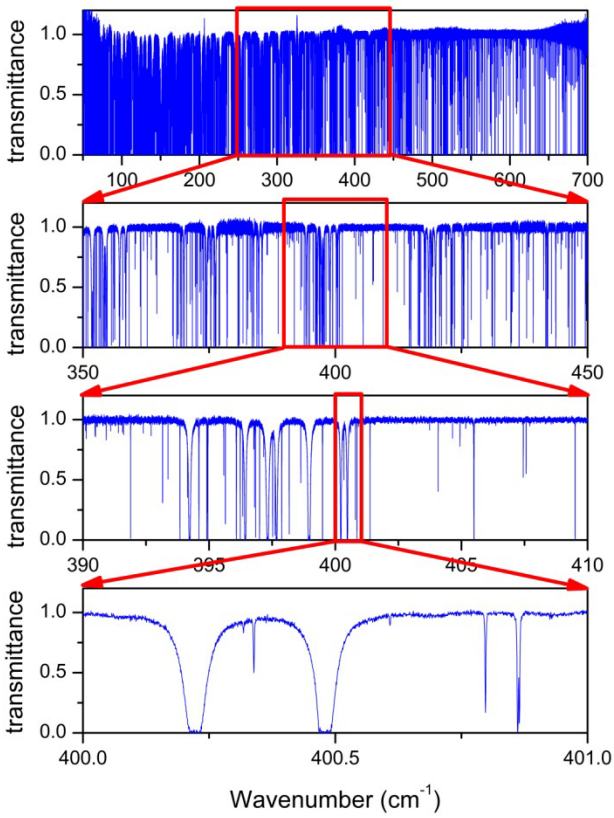

Fig. 2.5.

Successive zooms of the FTS spectrum #3 of natural water vapor recorded at SOLEIL synchrotron at room temperature between 50 and 720 cm^{-1} (P = 0.86 Torr).

To calibrate the frequency and to check the calibration stability, the first and the last spectra were recorded at very low pressure after pumping the cell. Only the strongest lines with the intensities more than 10^{-18} cm/molecule remained in the observed spectrum and were retrieved from these spectra

In the near-infrared range, a single spectrum was recorded at a pressure of 1 Torr maintained by a computer based Proportional/Integral controller. All the CRDS recordings were acquired in the slow flow regime (**Sect. 1.1.2**) at 1 Torr pressure. The spectrum is shown in **Fig. 2.6** with three successive zooms illustrating the recording quality. The noise equivalent absorption is lower than 10^{-11} cm^{-1}.

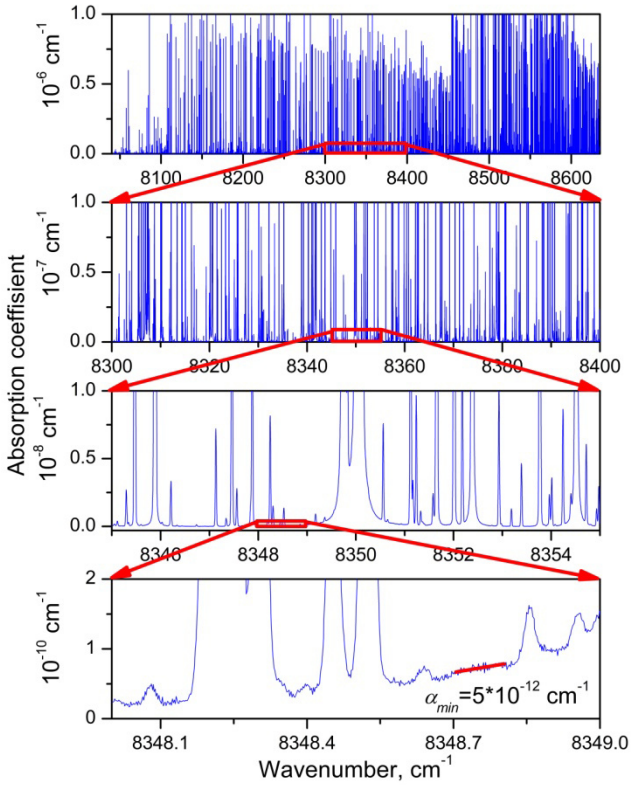

Fig. 2.6.

Room temperature CRDS spectrum of natural water vapor around 8348 cm^{-1}. The sample pressure was about 1.0 Torr. The successive enlargements illustrate the high dynamic range of the recordings and the noise level on the order of $\alpha_{min} \sim 5\times10^{-12}$ cm^{-1}.

2.2 Data treatment method

2.2.1 Fit procedure

Line parameters were retrieved using a homemade multiline fitting program written in LabVIEW and C++ both for far- and near- infrared spectra. The HITRAN2020 line list was the starting point of the fit (reference line list) in the far-infrared. For near-infrared range, we used a variational vibration-rotational (VR) line lists [https://spectra.iao.ru/molecules/simlaunch?mol=1] based on the results of Schwenke and Partridge [Partridge1997, Schwenke2000] with empirically corrected line positions by Semen Mikhailenko based on empirical values of vibrational-rotational energy levels known from previous studies.

The Voigt line profile was adopted in both frequency ranges. In the far-infrared range, the line fit was performed by M. Toureille during her master internship. The lines were additionally broadened by the instrumental function of FTS spectrometer (see **Sect. 1.2.1.2**). An accurate account of its influence requires complicate treatment using Eq. (1.17) that makes the fit procedure much more difficult. To

avoid that, the influence of instrumental function was just roughly compensated by fixing the width of the Gaussian component to an "effective" value, which was determined as follows. The fit of 10 single well resolved lines was performed adjusting their area, position and both Lorentzian and Gaussian widths for each spectrum. The resulted Gaussian width was found to be expectedly larger than calculated Doppler broadening due to the instrumental function contribution. The average value of these fitted Gaussian widths was adopted as default "effective" value for all other fitted lines of the recorded spectrum. **Figures 2.7** illustrates the result of the fit procedure in a narrow spectral interval. Although this approach does not affect the accuracy of line position determination, it limits the accuracy of line intensity determination (see **Sect. 2.3.2**). Let us underline that the main purpose and output of the far-infrared spectra are the line positions, *ab initio* intensities of the rotational transitions being very accurate in the existing databases.

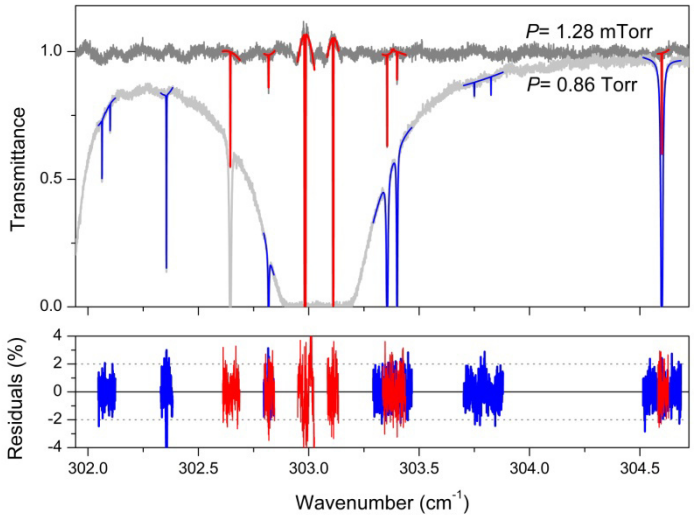

Fig. 2.7. Line parameter retrieval from the FTS spectra of water vapor near 303 cm^{-1}. The line profile fit was performed in narrow spectral intervals around the lines which are not too saturated.

Upper panel: Recorded spectra #1 (1.6 μbar) and #3 (0.91 mbar) (grey and light grey, respectively) with corresponding best fit spectra (red and blue, respectively).

Lower panel: Corresponding (exp. – fit) residuals in % .

In the near-infrared range, spectra were recorded in Doppler regime. Line widths mainly defined by the Doppler broadening (about 0.014 cm^{-1} near 8300 cm^{-1}) and do not depend on pressure (pressure broadening HWHM is about 5×10^{-4} cm^{-1} at 1 Torr pressure). For most of lines, positions and intensities only were retrieved. The width of the Gaussian component was fixed to the calculated Doppler broadening. The width of collisional component was fixed to 5×10^{-4} cm^{-1} and line intensities are proportional to the integrated absorption coefficient. The exception was the strongest lines for which the adjustment of collisional width improved fit residuals in about 10 times. **Figures 2.8** presents fit examples for small pieces of spectra recorded with CRDS.

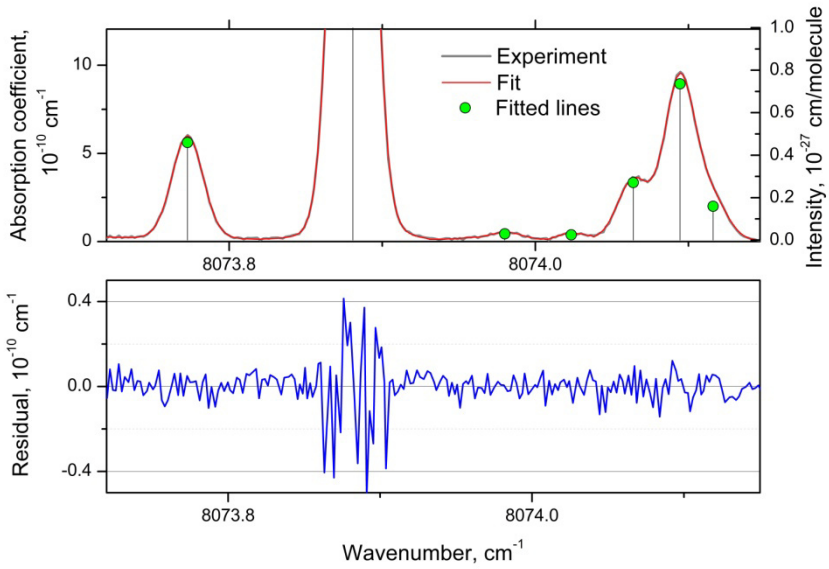

Fig. 2.8

Example of spectrum reproduction for the CRDS spectrum of water vapor near 8074 cm^{-1}. The obtained line list is superimposed as a stick diagram (marked by green dots). The two weak lines around 8074 cm^{-1} have an intensity of about 2×10^{-29} cm/molecule

A difference in fit procedure between far- and near-infrared spectra was in treatment of unresolved lines (in particular, doublets). In FTS spectra recorded at pressures 0.91 and 7 mbar, doublets were omitted (see an example on **Fig. 2.7**). The centres of lines in doublets were determined from spectrum #1. Water spectrum in the near-infrared range is more complicated (it contains more than 5500 lines while far-infrared spectra have about 3000 lines in total taking into account the repeated measurements) and there is a significant number of strongly overlapping groups of more than 2 lines. In order to retrieve the parameters of a line in such group, the less intense lines were included into the fit with fixed line shape parameters from the reference line list. These 1213 "frozen" lines were included in the experimental line list with the tag "F" indicating that they should be avoided in the discussion and comparison because their parameters rely from literature values.

In both frequency ranges, the parameters of single lines (if they are well resolved) were obtained from the local fit even if such line was located on the wing of strong neighbouring line. Experimental line lists are provided in supplementary materials of [Toureille2022] for far-infrared range and [Koroleva2023] for near-infrared. For each fitted line, it includes the line position and line intensity with their uncertainty as provided by the fit, the empirical value of the lower state energy, rotational and vibrational quantum numbers together with the comparison with the line parameters provided by the HITRAN database [Gordon2022] and the W2020 list [Furtenbacher2020, Furtenbacher2020II] (see next section), when available. In the far-infrared range, the presented global line list is a combination of fit results from 5 datasets (spectra #1-#5 from **Table 2.1**). It includes 2867 lines with intensities between $2 \times 10^{-26} – 2 \times 10^{-19}$ cm/molecule. This line list overview is presented on **Fig. 2.9**.

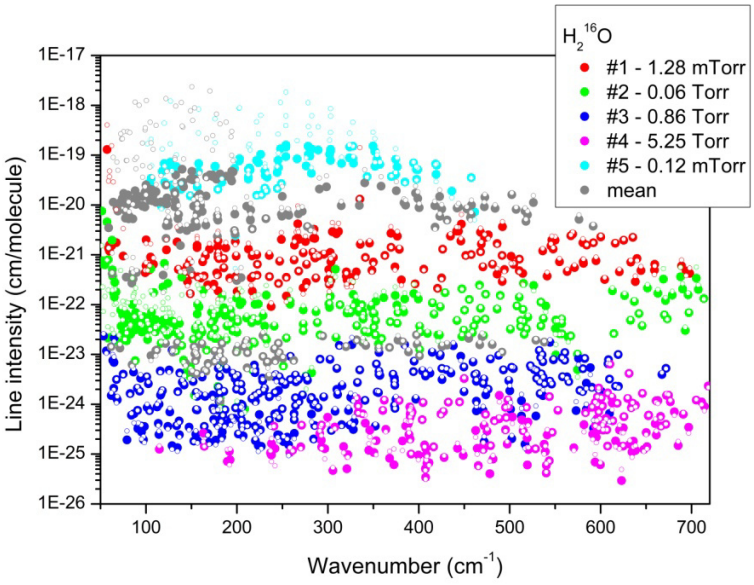

Fig. 2.9

Global line list constructed in this work from spectra #1 - #5. Different colours are used for the spectrum chosen as source of the line parameters. Grey symbols mark the lines for which the position and intensity correspond to values averaged from two spectra. Small open circles correspond to the HITRAN list.

Near-infrared line list consists of 5430 lines of six water isotopologues. Their intensities range between 3.6×10^{-30} and $1.5 \cdot \times 10^{-22}$ cm/molecule.

2.2.2 Frequency calibration

While CR-CRDS provides the absolute frequency (see **Sect. 1.1.2**), FTS spectra need to be calibrated. That is why this chapter is devoted to the far-infrared range only. However, the checking of frequency scale on the near-infrared range was performed by comparison with accurate CO line positions (see **Sect. 2.3.1**).

Frequency calibration in the far-infrared range was made by comparison of fitted positions of isolated lines with good signal-to-noise ratio with the most accurate HITRAN2020 line positions with declared accuracy better than 10^{-5} cm^{-1}. Although spectra #1 and #5 are the most suitable for calibration, lines with a high signal-to-noise ratio were also selected from spectra #2 and #3 to increase sampling and obtain a more accurate frequency correction. (The 7 mbar spectrum #4 was excluded as lines positions can be shifted by pressure up to $\pm 4 \times 10^{-4}$ cm^{-1}, which is larger than lines positions determination uncertainty). About 700 lines in total were selected and matched to the chosen HITRAN most accurate lines. The differences between these experimental line centres and the HITRAN values depend linearly on wavenumber and independent on the spectrum (**Fig. 2.10**, left panel). The resulted *rms* deviation of position difference from fitted linear function is 2.42×10^{-5} cm^{-1} (at least 2 times better than declared uncertainty of HITRAN lines used for comparison). On the basis

of this analysis the following empirical correction of frequency was applied: $+8.4(6)\times10^{-5}-6.30(7)\times10^{-7}\sigma$, where σ is the wavenumber in cm^{-1}.

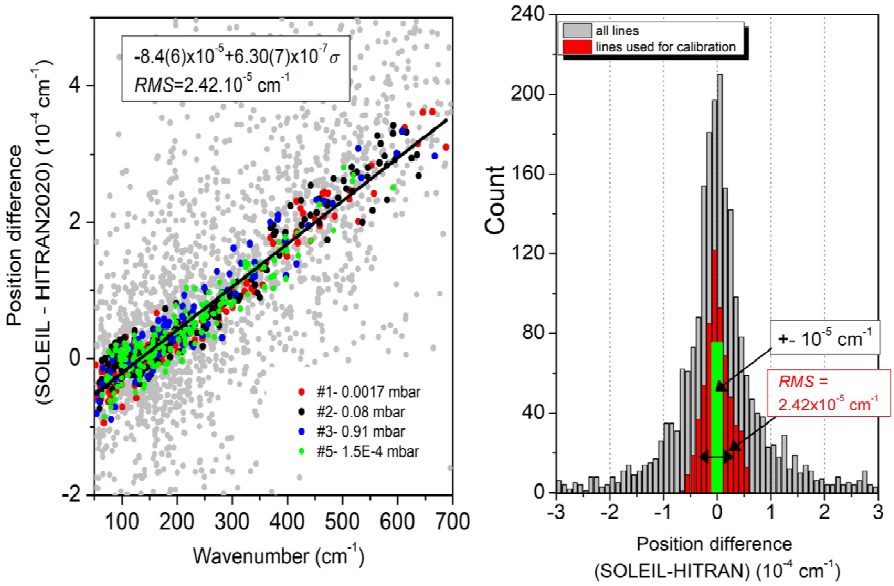

Fig. 2.10.

Frequency calibration of the FTS spectra.

Left panel: The colored symbols correspond to the differences between the line centers retrieved from the different recorded spectra and reference line positions provided with an uncertainty better than 10^{-5} cm^{-1} in the HITRAN database. The solid line is a linear function fitted to the calibration dataset. Gray symbols correspond to all line positions.

Right panel: Histograms of the (meas. – HITRAN) position differences for the lines used for the frequency calibration (red) and for the whole set of measurements. The green bars correspond to the HITRAN uncertainty of the used reference lines ($\pm10^{-5}$ cm-1).

The value of 5×10^{-5} cm^{-1} appears as a reasonable estimation for the position uncertainty (see **Fig. 2.10**) for isolated and unsaturated lines caused by applied frequency calibration although for a large fraction of such lines uncertainty provided by fit is smaller. For these lines, the line position uncertainty was replaced to 5×10^{-5} cm^{-1}. It is believed to be an overestimation of the real uncertainties. However, for weak or highly blended lines the uncertainty could reach 1×10^{-3} cm^{-1}.

The histogram in the right panel of **Fig. 2.10** presents the difference between observed and tabulated in HITRAN2020 positions for all fitted lines. For many lines it is larger than experimental error bars, indicating possible inaccurate HITRAN position values that will be a discussed in **Sect. 2.3**.

2.2.3 Lines assignment and energy levels determination

Most of lines could be straightforwardly assigned by comparison of their fitted positions and intensities with the reference line lists. This is so-called “trivial assignment”. It was performed by S.N. Mikhailenko in the far-infrared range and checked by him in the near-infrared.

Overall, a non-trivial identification with known experimental energy levels was needed for 5 lines in the far-infrared range with incomplete HITRAN assignment and for less than 300 lines in the near-infrared with either new or inaccurate upper state energy level. At the end of the assignment procedure, 20 lines were left unassigned in the near-infrared spectral range.

Statistical information for rovibrational assignment is summarised in Table 2.2 and Table 2.3 for FTS and CRDS spectra, correspondingly.

Table 2.2
Statistics of the rovibrational assignments of lines observed in natural water spectra in the far-infrared range.

Molecule	NT [a]	NT_{new} [b]	J	K_a	Range, cm^{-1}
$H_2{}^{16}O$	1310	96(385)	22	14	51.43 – 718.43
$H_2{}^{18}O$	564	3(3)	18	12	53.57 – 702.59
$H_2{}^{17}O$	407	3(3)	17	10	53.51 – 694.38
$HD^{16}O$	674	46(63)	19	12	50.27 – 591.88
$HD^{18}O$	42	0	10	7	78.51 – 310.10
$HD^{17}O$	4	0	6	4	168.17 – 255.19
Total	3001	148(454)	22	14	50.27 – 718.43

Notes
[a] Number of assigned transitions
[b] Number of newly observed transitions. The first number considers previous studies by absorption and emission. The number in parenthesis considers only absorption studies.

Overall 454 transitions in the far-infrared range and more that 1600 lines in the near-infrared range were newly measured (see **Fig. 2.3**). (Note, that 306 of the far-infrared lines were measured before only by emission spectroscopy whit significantly larger parameters uncertainty). Part of these transitions was used to correct or to derive new energy levels.

Table 2.3

Statistical overview of the assigned water transitions previously reported and retrieved in the present study by CRDS in the near-infrared range.

Molecule	This study				Published data (see **Sect. 1.1.1.2**)				
	N_{TW}[a]	Region, cm^{-1}	J_{max}	$K_{a\,max}$	$N_{Lit.}$[b]	Region, cm^{-1}	J_{max}	$K_{a\,max}$	N_{new}[c]
$H_2{}^{16}O$	3237	8041.4 – 8633.4	19	10	2508	8041.4 – 8633.4	20	10	980[d]
$H_2{}^{18}O$	911	8043.9 – 8632.5	15	8	869	8043.9 – 8632.5	14	7	208
$H_2{}^{17}O$	540	8042.5 – 8632.5	15	7	282	8042.6 – 8632.3	13	6	291
$HD^{16}O$	707	8041.6 – 8631.1	15	9	785	8041.6 – 8633.5	16	8	170
$HD^{18}O$	32	8443.0 – 8633.2	8	5	382	8042.7 – 8633.2	13	8	
$HD^{17}O$	3	8538.3 – 8595.3	3	2	30	8469.3 – 8629.8	7	4	

Notes

[a] N_{TW} – number of transitions assigned in the present work

[b] $N_{Lit.}$ – number of transitions reported in previous absorption studies

[c] N_{new} – number of new transitions reported in this work. Note that N_{new} is not equal to N_{TW}– $N_{Lit.}$ because due to very high optical depth for some of the strong lines or spectral gaps in our CRDS spectrum, some of previously reported transitions ($N_{Lit.}$) cannot be measured in the current study.

[d] This number does not consider the (less accurate) measurements by emission spectroscopy [Zobov2008].

In the near-infrared range values of 81 rovibrational levels of four water isotopologues ($H_2{}^{16}O$, $H_2{}^{18}O$, $H_2{}^{17}O$, and $HD^{16}O$) were newly determined. 140 energy levels are differing from the literature by more than the measurement uncertainty (5×10^{-3} cm^{-1}).

2.3 Comparison with literature data

In this paragraph, the comparison of the obtained line parameters with HITRAN2020 [Gordon2020] and W2020 [Furtenbacher2020, Furtenbacher2020II] line lists as well as with previous theoretical calculations and experimental measurements is discussed for the two spectral ranges. The line lists supplemented to [Toureille2022, Koroleva2023] also contain HITRAN2020 and W2020 line parameters and the deviation from the measurements (see line lists samples in **Fig. 2.11**)

Section 2.3.1 presents brief review of denoted literature sources while the two next sections are devoted to the comparison of the experimental line positions and energy levels (**Sect. 2.3.2**) and line intensities (**Sect. 2.3.3.**)

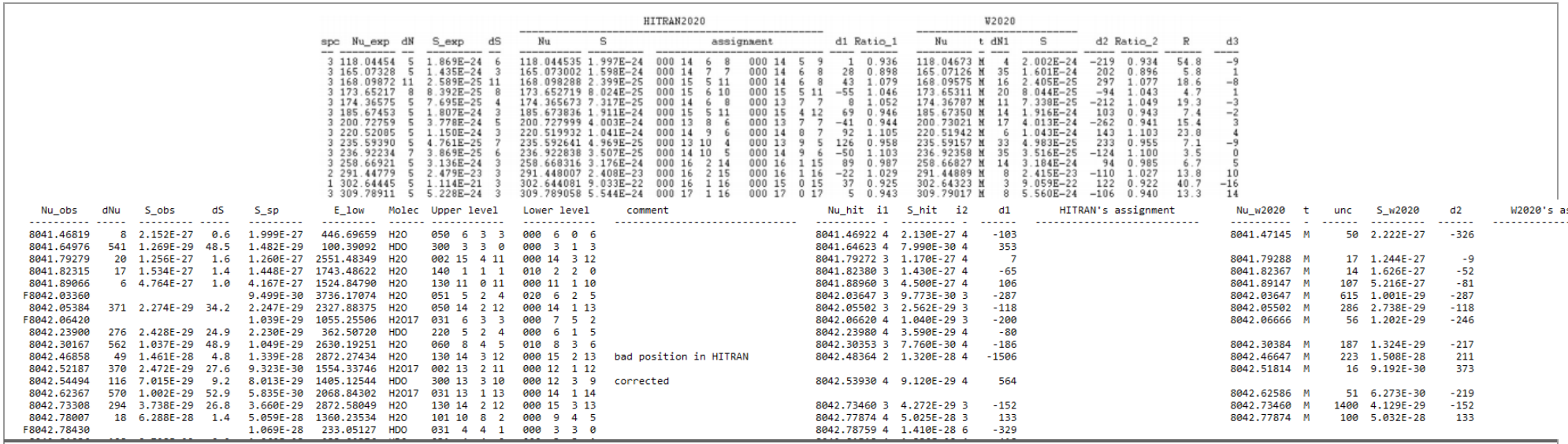

						HITRAN2020								W2020							
spc	Nu_exp	dN	S_exp	dS	Nu	S	assignment			d1	Ratio_1	Nu	t	dN1	S	d2	Ratio_2	R	d3
3	118.04454	5	1.869E-24	6	118.044535	1.997E-24	000 14 6 8	000 14 5 9		1	0.936	118.04673	M	4	2.002E-24	-219	0.934	54.8	-9
3	165.07328	5	1.435E-24	3	165.073002	1.598E-24	000 14 7 7	000 14 6 8		28	0.898	165.07126	M	35	1.601E-24	202	0.896	5.8	1
3	168.09872	11	2.589E-25	11	168.098208	2.399E-25	000 15 5 11	000 14 6 8		43	1.079	168.09575	M	16	2.405E-25	297	1.077	10.6	-8
3	173.65217	8	8.392E-25	8	173.652719	8.024E-25	000 15 6 10	000 15 5 11		-55	1.046	173.65311	M	20	8.044E-25	-94	1.043	4.7	1
3	174.36575	5	7.695E-25	4	174.365673	7.317E-25	000 14 6 8	000 13 7 7		8	1.052	174.36707	M	11	7.338E-25	-212	1.049	19.3	-3
3	185.67453	5	1.807E-24	3	185.673836	1.911E-24	000 15 5 11	000 15 4 12		69	0.946	185.67350	M	14	1.916E-24	103	0.943	7.4	-2
3	200.72759	5	3.778E-24	5	200.727999	4.003E-24	000 13 8 6	000 13 7 7		-41	0.944	200.73021	M	17	4.013E-24	-262	0.941	15.4	3
3	220.52085	5	1.150E-24	3	220.519932	1.041E-24	000 14 9 6	000 14 8 7		92	1.105	220.51942	M	6	1.043E-24	143	1.103	23.8	4
3	235.59390	5	4.761E-25	7	235.592641	4.969E-25	000 13 10 4	000 13 9 5		126	0.958	235.59157	M	33	4.983E-25	233	0.955	7.1	-9
3	236.92234	7	3.869E-25	6	236.922838	3.507E-25	000 14 10 5	000 14 9 6		-50	1.103	236.92358	M	35	3.516E-25	-124	1.100	3.5	0
3	258.66921	5	3.136E-24	3	258.668316	3.176E-24	000 16 2 14	000 16 1 15		89	0.987	258.66827	M	14	3.184E-24	94	0.985	6.7	5
2	291.44779	5	2.479E-23	3	291.448007	2.408E-23	000 16 2 15	000 16 1 16		-22	1.029	291.44889	M	8	2.415E-23	-110	1.027	13.8	10
1	302.64445	5	1.114E-21	3	302.644081	9.033E-22	000 16 1 16	000 15 0 15		37	0.925	302.64323	M	3	9.059E-22	122	0.922	40.7	-16
3	309.78911	5	5.228E-24	3	309.789058	5.544E-24	000 17 1 16	000 17 0 17		5	0.943	309.79017	M	8	5.560E-24	-106	0.940	13.3	14

Nu_obs	dNu	S_obs	dS	S_sp	E_low	Molec	Upper level	Lower level	comment	Nu_hit	i1	S_hit	i2	d1	HITRAN's assignment	Nu_w2020	t	unc	S_w2020	d2	W2020's a
8041.46819	8	2.152E-27	0.6	1.999E-27	446.69659	H2O	050 6 3 3	000 6 0 6		8041.46922	4	2.130E-27	4	-103		8041.47145	M	50	2.222E-27	-326	
8041.64976	541	1.269E-29	48.5	1.482E-29	100.39092	HDO	300 3 3 0	000 3 1 3		8041.64623	4	7.990E-30	4	353							
8041.79279	20	1.256E-27	1.6	1.260E-27	2551.48349	H2O	002 15 4 11	000 14 3 12		8041.79272	3	1.170E-27	4	7		8041.79288	M	17	1.244E-27	-9	
8041.82315	17	1.534E-27	1.4	1.448E-27	1743.48622	H2O	140 1 1 1	010 2 2 0		8041.82380	3	1.430E-27	4	-65		8041.82367	M	14	1.626E-27	-52	
8041.89066	6	4.764E-27	1.0	4.167E-27	1524.84790	H2O	130 11 0 11	000 11 1 10		8041.88960	3	4.500E-27	4	106		8041.89147	M	107	5.216E-27	-81	
F8042.03360				9.499E-30	3736.17074	H2O	051 5 2 4	020 6 2 5		8042.03647	3	9.773E-30	3	-287		8042.03647	M	615	1.001E-29	-287	
8042.05384	371	2.274E-29	34.2	2.247E-29	2327.88375	H2O	050 14 2 12	000 14 1 13		8042.05502	3	2.562E-29	3	-118		8042.05502	M	286	2.738E-29	-118	
F8042.06420				1.039E-29	1055.25506	H2O17	031 6 3 3	000 7 5 2		8042.06620	4	1.040E-29	3	-200		8042.06666	M	56	1.202E-29	-246	
8042.23900	276	2.428E-29	24.9	2.230E-29	362.50720	HDO	220 5 2 4	000 6 1 5		8042.23980	4	3.590E-29	4	-80							
8042.30167	562	1.037E-29	48.9	1.049E-29	2630.19251	H2O	060 8 4 5	010 8 3 6		8042.30353	3	7.760E-30	4	-186		8042.30384	M	187	1.324E-29	-217	
8042.46858	49	1.461E-28	4.8	1.339E-28	2872.27434	H2O	130 14 3 12	000 15 2 13	bad position in HITRAN	8042.48364	2	1.320E-28	4	-1506		8042.46647	M	223	1.508E-28	211	
8042.52187	370	2.472E-29	27.6	9.323E-30	1554.33746	H2O17	002 13 2 11	000 12 1 12								8042.51814	M	16	9.192E-30	373	
8042.54494	116	7.015E-29	9.2	8.013E-29	1405.12544	HDO	300 13 3 10	000 12 3 9	corrected	8042.53930	4	9.120E-29	4	564							
8042.62367	570	1.002E-29	52.9	5.835E-30	2068.84302	H2O17	031 13 1 13	000 14 1 14								8042.62586	M	51	6.273E-30	-219	
8042.73308	294	3.738E-29	26.8	3.660E-29	2872.58049	H2O	130 14 2 12	000 15 3 13		8042.73460	3	4.272E-29	3	-152		8042.73460	M	1400	4.129E-29	-152	
8042.78007	18	6.288E-28	1.4	5.059E-28	1360.23534	H2O	101 10 8 2	000 9 4 5		8042.77874	4	5.025E-28	3	133		8042.77874	M	100	5.032E-28	133	
F8042.78430				1.069E-28	233.05127	HDO	031 4 4 1	000 3 3 0		8042.78759	4	1.410E-28	6	-329							

Fig. 2.11.

Beginning of Tables provided as a Supplementary Material of [Toureille2022] (upper panel) and [Koroleva2023] (lower panel) listing measured absorption lines parameters in comparison with HITRAN2020 and W2020.

The (exp-HITRAN2020), (exp-W2020) and (exp.-14CoMaPi) position differences are given in 10^{-5} cm^{-1} units in columns, d1, d2 and d3, respectively.

The ratio R= |d2|/dN1compares the absolute deviation of the W2020 position to the W2020 position uncertainty (dN1)

2.3.1 Line parameters data sources

Nowadays, there is a number of spectroscopic databases supplying information on spectral line parameters for atmospheric and astrophysical applications in a wide range of frequencies and thermodynamic conditions, such as HITRAN [https://hitran.org/], GEISA [https://geisa.aeris-data.fr/], ExoMol [https://www.exomol.com/], Koeln's database [https://cdms.astro.uni-koeln.de/], Spectra [https://spectra.iao.ru/], AER [https://github.com/AER-RC]. Within the frames of this work, it was decided to use only HITRAN database for comparison with experimentally observed line parameters as it is the most popular and frequently updated. However, the data provided by HITRAN were expanded by using some of its sources.

The goal of HITRAN is to provide the set of the most accurate and self-consistent parameters for atmospheric applications. It is a compilation of the best theoretical and experimental results (as usually theoretical calculations are more complete but experimental one sometimes more accurate). HITRAN presents it as line list containing line profile parameters (central frequencies, intensities, self- and air-broadening coefficients) together with transition characteristics (quantum numbers, Einstein-A coefficient, lower-state energy of the transition) supplemented with their uncertainties and information source for each monomer line. It also contains information on the absorption cross-sections, continuum absorption, aerosol properties. The information is updated as a new more accurate data become available. Major updates are summarised in related publication, which occurs every 4 years, the last version is HITRAN2020 [Gordon2022].

One of the important line position sources used in HITRAN2020 is theW2020 line list [Furtenbacher2020, Furtenbacher2020II]. This line list is available for $H_2{}^{16}O$, $H_2{}^{18}O$ and $H_2{}^{17}O$ lines only. The calculations are based on the xMARVEL procedure that allows calculating line positions from energies of molecular levels with experimental accuracy even for transitions which were not previously measured. This procedure was applied to an exhaustive set of absorption and emission measured line positions collected in the literature, in order to derive accurate sets of empirical energy levels of $H_2{}^{16}O$, $H_2{}^{18}O$ and $H_2{}^{17}O$ [Furtenbacher2020, Furtenbacher2020II]. Based on it, line positions are obtained and supplemented by *ab initio* calculated line intensities from [Polyansky2018]. Although complete and self-consistent, the W2020 line positions shows deviation from measured ones largely exceeding claimed uncertainties due to difficulties in filtering data by xMARVEL procedure. It will be discussed in details in **Sect. 2.3.2**.

The review of previous experimental works aimed at determining the best line positions and intensities in the far-infrared range by absorption spectroscopy includes studies [Kauppinen1978, Kauppinen1982, Johns1985, Paso1995, Matsushima1995, De Natale1997, Toth1998, Chen2000, Horneman2005, Matsushima2006, Cazzolli2009, Drouin2011, Yu2012, Mikhailenko2020-II] for the five lowest vibrational states – (000), (010), (020), (001), and (100) – up to a maximum value of the rotation quantum number Jmax = 17. The experimental emission spectra in the far-infrared range are

presented in [Polyansky1996, Polyansky1997, Polyansky1997II, Coudert2004, Coheur2005, Yu2012, Coudert2014]. These works contain assignment of more than 6000 transitions involving 14 vibrational states with J_{max} = 41 [Coheur2005] for the ground state (000).

An additional source of calculated line positions for the water main isotopologue for rotational quantum number up to J_{max} = 30 in the far-infrared range is [Coudert2014] calculations (denoted as 14CoMaPi hereafter). It is based on the effective Hamiltonian with parameters determined from a weighted least-squares fitting based on a 24461 set of literature data including rotational energy levels, microwave, far infrared, and infrared measured transition frequencies.

In the near-infrared range, high-resolution absorption spectra measurements were reported in [Flaud1979, Mandin1988, Bykov2001, Hu2001, Naumenko2004, Tolchenov2005, Liu2006, Mikhailenko2009, Mikhailenko2010, Oudot2010, Régalia2014, Campargue2015] containing the data for six most abundant water isotopologues ($H_2{}^{16}O$, $H_2{}^{18}O$, $H_2{}^{17}O$, $HD^{16}O$, $HD^{18}O$, $HD^{17}O$). An analysis of high-temperature emission spectra was published in [Zobov2008] with resulting vibration-rotation transitions of $H_2{}^{16}O$.

In both frequency ranges, experimental line positions and intensities are compared with HITRAN2020 and W2020 line lists. In addition, experimental $H_2{}^{16}O$ line positions are compared with 14CoMaPi the far-infrared range. As for near-infrared range, the determined line positions and intensities are compared the most sensitive study by FTS with absorption pathlengths up to 1203 m [Régalia2014] (hereafter denoted as FT2014), and with previous CRDS measurements in overlapping frequency range [Campargue2015] (CRDS2015, recall that these measurements were performed using the same setup but with different laser and without self-referenced frequency comb).

2.3.2 Line positions and energy levels

Our results show an overall good agreement with literature data both in the far- and near-infrared ranges. In the far-infrared range, the *rms* deviation on new and the literature line positions observed by absorption spectroscopy [Kauppinen1978, Kauppinen1982, Johns1985, Paso1995, Matsushima1995, De Natale1997, Toth1998, Chen2000, Horneman2005, Matsushima2006, Cazzolli2009, Drouin2011, Yu2012, Mikhailenko2020-II] for each isotopologue is between 4.02×10^{-5} and 3.66×10^{-4} cm^{-1}. In the near-infrared range, the *rms* deviation between new and previous line positions is 2.05×10^{-3} cm^{-1} and 1.96×10^{-3} cm^{-1} for FTS2014 and CRDS2015 (including all outliers), respectively.

Figure 2.12 illustrates the agreement of presented line positions in far-infrared range with HITRAN2020, W2020 and 14CoMaPi line lists for the main water isotopologue. A Gaussian function was fitted to histograms of W2020 and 14CoMaPi deviations (**Fig 2.12**, right panel). Their centres were found to be at about $\times10^{-6}$ cm^{-1} for 1310 transitions with the profile width of 5×10^{-5} cm^{-1}, corresponding to our claimed position uncertainty of the "good" (isolated, unsaturated and not too weak) lines. It confirms that positions of lines are not biased in average in both line lists. However, for

some lines the deviation from W2020 and HITRAN2020 is significant and reaches 3×10^{-3} cm^{-1}. The difference from 14CoMiPa is smaller (**Fig 2.12**) and does not show so many outliers.

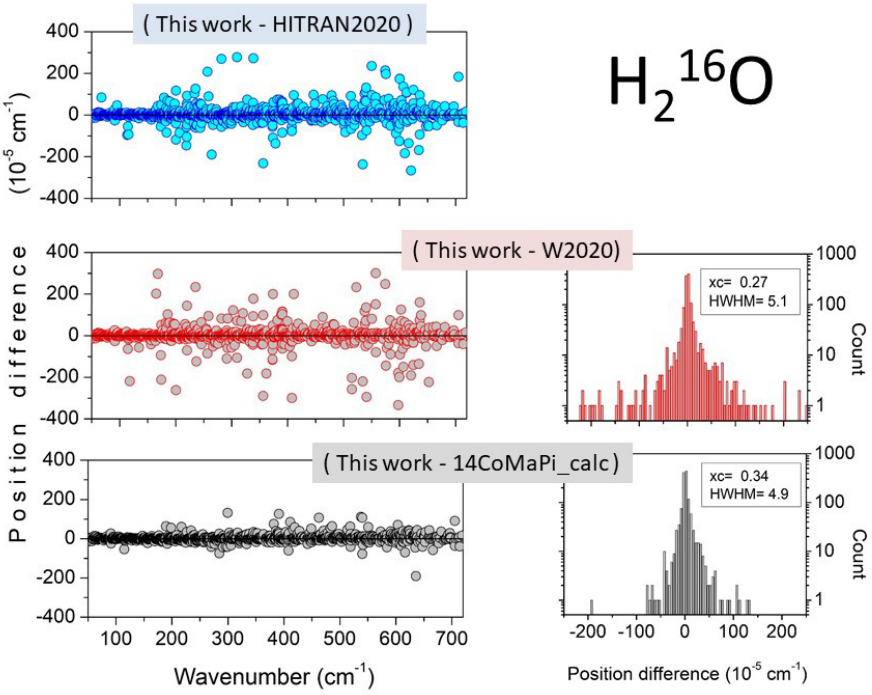

Fig. 2.12.

Position comparison of the $H_2{}^{16}O$ lines in the 50–720 cm^{-1} range.

Left panels: Differences between the FTS experimental values and previously known data.

Right panels: Histograms of the deviations between the experiment and the W2020 and 14CoMaPi positions. The centre (xc) and width (HWHM) obtained from a Gaussian fit to the histograms are given in the plot (in 10^{-5} cm^{-1} units).

Some of these problematic cases are presented on **Figs. 2.13 and 2.14** for HITRAN2020 and W2020 by direct comparison with observed spectra. **Figure 2.13** presents the transitions with both W2020 and HITRAN2020 positions disagreement with experimental spectra. Note that W2020 is one of the major sources for HITRAN2020 positions both in far- and in near-infrared range. However, disagreement between these two databases is observed, in particular, some of HITRAN positions does not coincide with W2020 positions indicated as their source (see examples in [Toureille2022, Koroleva2023]).

Figure 2.14 shows examples of W2020 line position deviation both from observed line position and HITRAN2020 position (given with W2020 source!) In total, for about 60 lines the difference between experimental and W2020 line position is larger than the stated W2020 position uncertainty, including 21 lines with 10 times bigger difference than W2020 stated uncertainty (for the pure rotational transition $15_{5\ 11} - 14_{4\ 10}$ at 388.70559 cm^{-1}, the difference is 459 times bigger, probably because of misassignment of the transition).

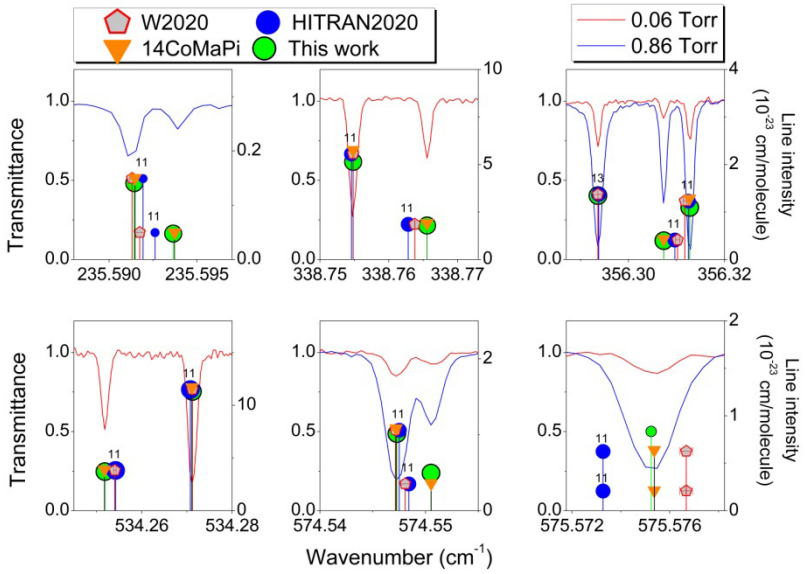

Fig. 2.13.

Comparison of water vapour FTS spectra (solid curves) with corresponding line positions from different sources (vertical bars with symbols). All the displayed examples correspond to inaccuracies of both the W2020 and HITRAN2020 positions. All the problematic lines correspond pure rotational transitions of $H_2{}^{16}O$ (assignments are given on each panel). The isotopologue number in HITRAN format is added for each transition.

For all the cases shown in **Fig. 2.13** and **2.14,** 14CoMaPi positions are in excellent agreement with experimental spectra. It is important to note that the accuracy of the previous measurements used in [Coudert2014] was not perfect, but using a large set of spectroscopic data extending beyond the spectral range under consideration and the use of the effective bending-rotation Hamiltonian fitted to experimental data made the calculation accuracy better than the position accuracy of the input data.

The only measured line which is absent in HITRAN is the pure rotational $H_2{}^{16}O$ doublet, $22_{\ 1\ 22} - 21_{\ 0\ 21}$ and $22_{\ 0\ 22} - 21_{\ 1\ 21}$, assigned to the line measured at 407.74639 cm^{-1} (intensity of 1.313×10^{-25} cm/molecule). It is in satisfactory agreement with W2020 position and intensity (407.74939 cm^{-1} and 1.04×10^{-25} cm/molecule, respectively).

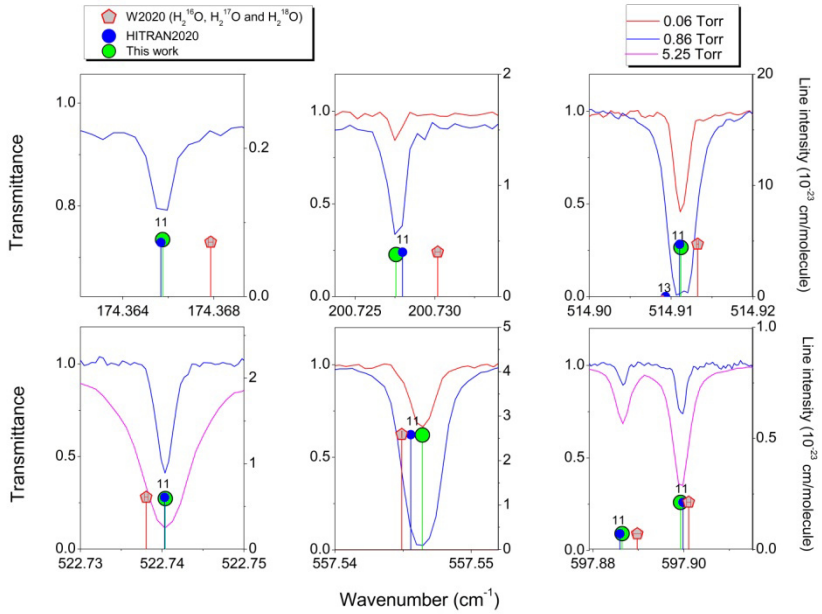

Fig. 2.14.

Comparison of water vapour FTS spectra (solid curves) with corresponding line positions from different sources (vertical bars with symbols). All the displayed examples correspond to inaccuracies of the W2020 positions. All the problematic lines correspond pure rotational transitions of $H_2^{16}O$ (assignments are given on each panel). The isotopologue number in HITRAN format is added for each transition.

As for the near-infrared range, **Fig. 2.15** illustrates the overall reasonable agreement between the CRDS line positions with line positions provided by FTS2014, CRDS2015, HITRAN2020 and W2020. All previously reported line positions seem to be systematically higher than new values. As in **Fig. 2.12** for the far-infrared, the differences between newly observed positions and FTS2014, CRDS2015 and W2020 were plotted as a histogram and Gaussian function was fitted to the obtained distributions. The fitted value of the center of the Gaussian was found to be -8.2×10^{-4}, -7.4×10^{-4}, and -3.4×10^{-4} cm^{-1}, respectively. This disagreement largely exceeds uncertainty of line positions in the CRDS spectrum provided by a self-referenced frequency comb (see discussion in **Sect. 2.2.2.-B.**). The source of this systematic shift could be the absence of sufficiently accurate reference lines for frequency calibration of spectra used for the FTS2014 line list (the uncertainty of the calibration is not reported in Ref. [Régalia2014]). The frequency values in CRDS2015 were provided only roughly by wavelength meter and then refined using the FTS2014 line positions. That is the reason why average deviation between the FTS2014 and CRDS2015 line positions is small.

For checking the accuracy of the frequency scale in the near infrared range provided by using a frequency comb, the comparison of fitted line positions with previously measured by the same setup water lines recorded as impurities in CO spectra [Borget2021] were performed. Line positions for the set of 34 lines (excluding two outliers) were found to be in agreement (with mean average difference of -2.9×10^{-5} cm^{-1} with a standard deviation of 1.4×10^{-4} cm^{-1}). An additional independent verification of

the the accuracy of our frequency scale was performed. The accurate upper state energy levels shared by 26 transitions observed in this region was determined from the set of 70 isolated lines positions measured in the 7710-7920 cm^{-1} range [Sironneau2015]. Most of these lines are weak (intensities are in the range of 10^{-29} - 5×10^{-27} cm/molecule), so the comparison was limited to four lines with intensities greater than 10^{-27} cm/molecule. Average position difference was found to be 2.2×10^{-5} cm^{-1} with a standard deviation of 7.5×10^{-5} cm^{-1}, confirming the correctness of the frequency scale.

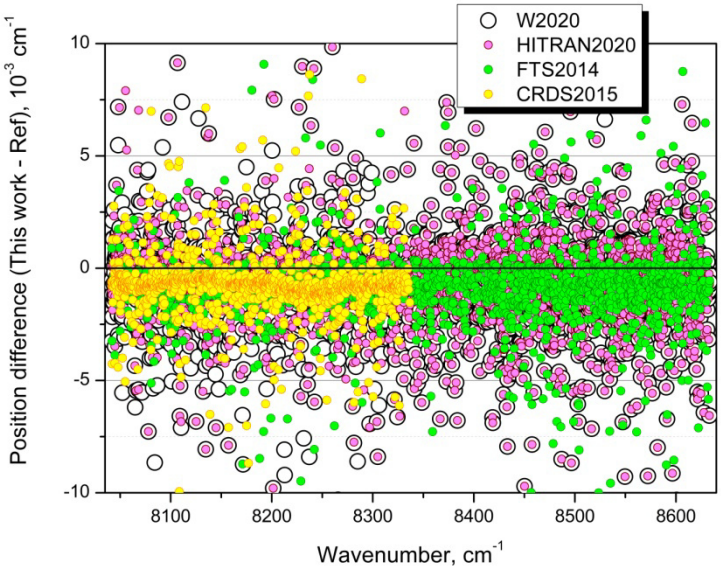

Fig. 2.15.

Position differences of the water vapor lines measured by CRDS between 8040 and 8620 cm^{-1} compared to various literature sources.

In [Régalia2014], water spectrum was studied by Fourier transform spectroscopy in the range 6450 - 9400 cm^{-1} at pressures ranging within 1-21 mbar using a pathlength varying from 0.29 to 1203 m. The multifit procedure was used to retrieve line positions, intensities and self-broadening coefficients for more than 11000 lines. In the frequency range under consideration, the FTS2014 list includes 2008 lines attributed to 2225 transitions of four water isotopologues ($H_2{}^{16}O$, $H_2{}^{18}O$, $H_2{}^{17}O$, and $HD^{16}O$) with minimum intensity values of a few 10^{-27} cm/molecule. The comparison of line positions from this work with FTS2014 shows a good agreement although in [Régalia2014] some of the doublets were fitted as a single line (the mean position difference is -9.6×10^{-4} cm^{-1} with a standard deviation 2×10^{-3} cm^{-1}).

In [Campargue2015], water spectrum was recorded in the frequency range 7911-8337 cm^{-1}. In the common with presented work frequency range, the CRDS2015 spectrum and the present study count 2163 and 2176 lines assigned to 2284 and 2262 water transitions, respectively. The coincidence between these two datasets is very good (the mean position difference is -7.3×10^{-4} cm^{-1} with a standard deviation 1.9×10^{-3} cm^{-1}). The minor deviations could be explained mostly by the presence of ammonia

as an impurity in different concentrations (20 times less in the presented work), the assignment problems and the weak doublets fit difficulty.

W2020 line list is based on the spectroscopically modified potential energy surface. This surface was optimized using empirical energy levels from multiple experimental sources (see **Sect. 2.3.1**) and has up to 2 times smaller average shift from the presented experimental results. The comparison with the most reliable line positions from W2020 (about 1400 lines with stated uncertainty smaller than 5×10^{-4} cm^{-1}) gives a centre of the corresponding histogram at -1.7×10^{-4} cm^{-1} (-3.4×10^{-4} cm^{-1} if the whole W2020 dataset consisting of 5616 lines is used).

As in the far-infrared range, in the near-infrared, W2020 line list is the source of many HITRAN2020 line positions. This explains that the difference of presented line positions with these two datasets looks similarly. However, 40 line positions of $H_2{}^{18}O$ and 12 line positions of $H_2{}^{17}O$ marked as taken from W2020 do not coincide with W2020 line positions.

HITRAN2020 includes 11650 transitions of seven most abundant water isotopologues in the near-infrared frequency range under consideration with intensity cut off 10^{-30} cm/molecule for all the isotopologues except for the $D_2{}^{16}O$ species with minimum intensity 10^{-32} cm/molecule. Note that 1124 transitions of $H_2{}^{16}O$, $H_2{}^{18}O$ and $H_2{}^{17}O$ species do not have complete vibration-rotation assignment. In the present work 5429 transitions are reported in 8041-8633 cm^{-1} range including 49 transitions missed in HITRAN (45 of them have intensity close to the HITRAN cut-off and correspond to minor isotopologues and 4 lines belong to the main isotopologue and have much larger intensities than the cut off). Two of these lines missing in HITRAN are shown in **Fig. 2.16**.

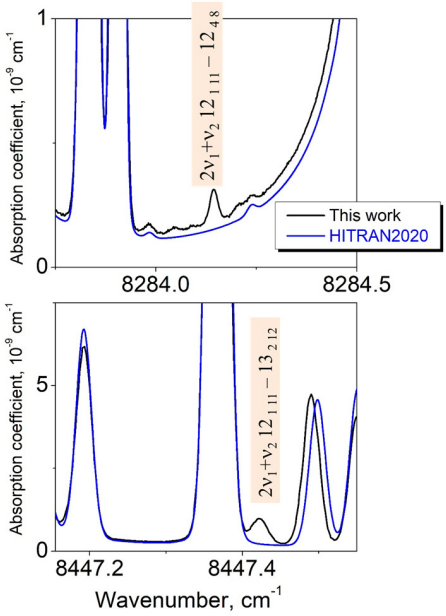

Fig. 2.16.

Two parts of the near IR experimental spectrum (black curve) in comparison with the spectrum simulation on the basis of the HITRAN2020 database (blue curve) demonstrating missed lines (vibrational-rotational assignment is given in the figure).

The line position differences of HITRAN positions with presented data for the 3 most abundant water isotopologues are shown in left panels of **Fig. 2.17**. The overall agreement is good except for the $H_2{}^{17}O$ isotopologue above 8340 cm^{-1}. These disagreements mostly originate from wrong or multiple assignments, as discussed in detail in [Koroleva2023].

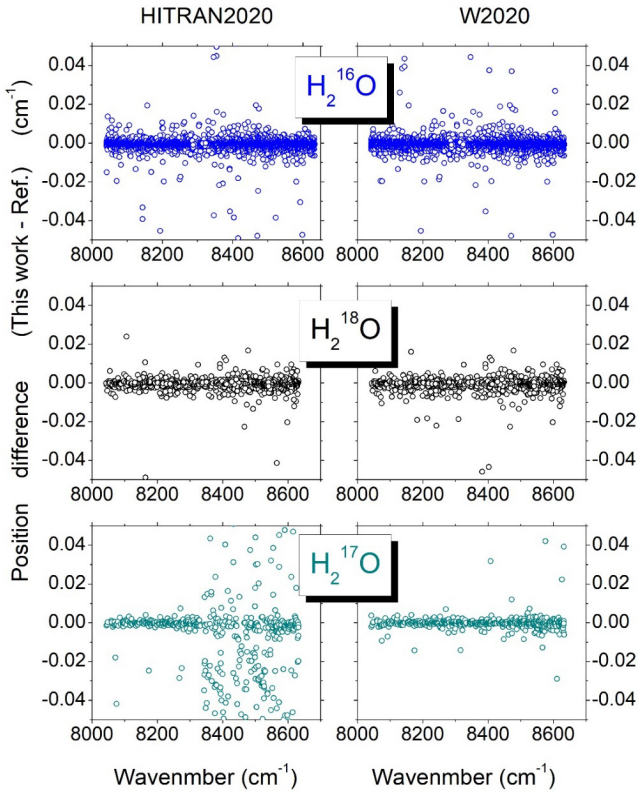

Fig. 2.17.

The $H_2{}^{16}O$, $H_2{}^{18}O$ and $H_2{}^{17}O$ line positions retrieved in this work versus the HITRAN2020 and W2020 values (left and right panels, respectively).

As for the W2020 line list, all 4687 retrieved in this work lines of three H_2O isotopologues are presented there. The assignment of 71 transitions missed in W2020 was completed. The agreement of the retrieved line positions with W2020 is very good (right panels in **Fig. 2.17**). Only 191 new positions deviate from the W2020 data by more than 0.005 cm^{-1}. **Fig. 2.18** shows examples of such disagreement with experimental spectrum for the main water isotopologue. 125 energy levels were corrected by more than 0.005 cm^{-1}, for 48 of these levels the difference between W2020 and experimental values exceed W2020 uncertainty by 10-375 times.

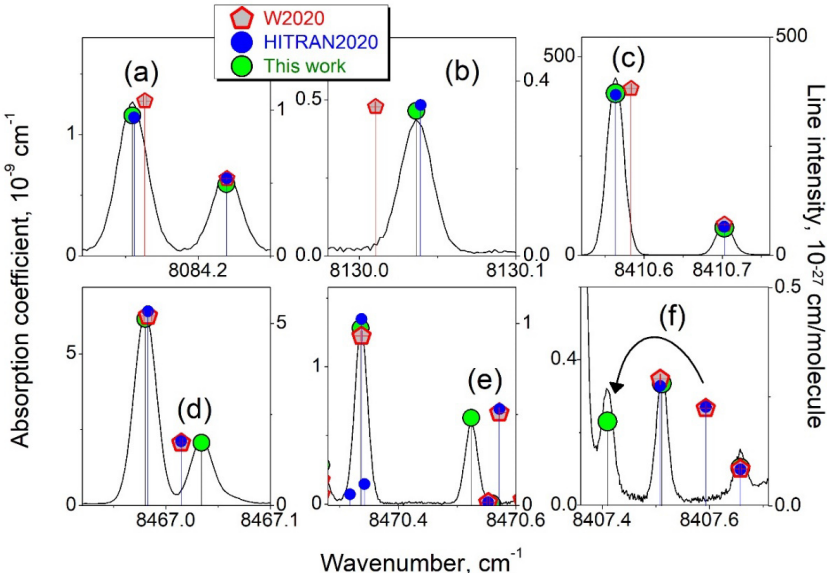

Fig. 2.18.

Examples of inconsistency between the CRDS spectrum of water vapor and the W2020 and HITRAN2020 line lists. The right-hand intensity scale is adjusted to correspond approximately to the peak heights.

2.3.3 Line intensities

The statistical uncertainty (or fit uncertainty) of retrieved line intensities is shown on **Fig. 2.19**. (Uncertainty due to pressure and temperature changes are negligible in both spectral ranges). This uncertainty is within 10% for most of the lines. The uncertainties on the level of 100% correspond to highly blended and/or weak lines.

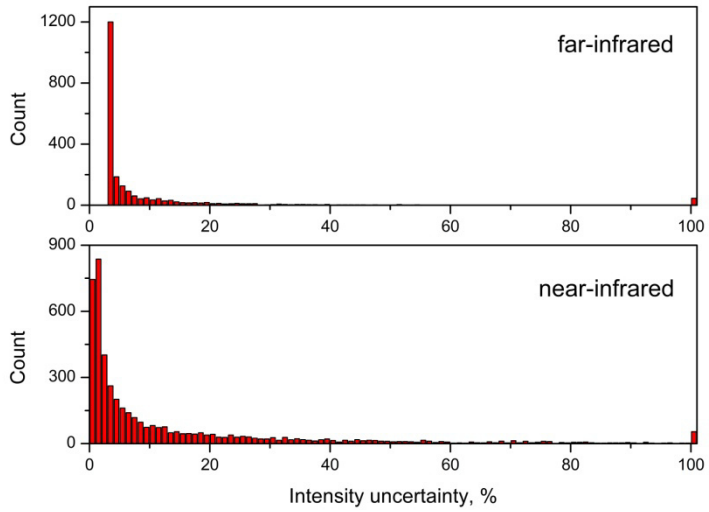

Fig. 2.19.

Statistical uncertainties of fitted line intensities in thefar- and near-infrared ranges.

In the far-infrared range, the high accuracy of line intensities could not be claimed. The limited number of points describing the line profile and the impact of the apparatus function which was roughly taken into account in the line parameter retrieval (see **Sect. 2.2.1**.) limit the accuracy of the retrieved values. The sources of HITRAN intensities in this frequency range are mostly *ab initio* calculations [Kyuberis2017, Conway2020] with accuracy higher than for presented measurements. However, it was found that most of line intensities agree with HITRAN2020 within 10 % experimental uncertainty. According to HITRAN2020 uncertainty codes, for 60.2% of line intensities the uncertainty is within 10% but for 8.2% of lines it is between 10 and 20% and for 31.6% of lines it is more than 20%. The comparison shows, therefore, that the intensities errors in HITRAN2020 may be somewhat overestimated. The agreement of experimentally observed line intensities with those that presented in W2020 line list is also good (within 10 % for about 86% of fitted lines). The exception are line intensities determined from two lowest pressure spectra #1 and #5. The influence of apparatus function to the line shape is too strong to be corrected in described way in case of such a low pressure. The saturation effects become considerable and the fitted values of the intensities are strongly underestimated by a factor up to 10 in the worst cases. Thus, the HITRAN intensities are more precise and should be preferred to those that was determined experimentally.

As for the near-infrared range, the situation is different. The ratios of measured line intensities to FTS2014, CRDS2015, HITRAN2020 and W2020 intensities are presented in **Fig. 2.20** for the $H_2{}^{16}O$ isotopologue. It shows an overall satisfactory agreement, which is better for experiment-based sources FTS2014 and CRDS2015. W2020 line intensities are on average systematically overestimated by about 10%.

In general, the difference between fitted intensities and HITRAN2020 and W2020 values is greater in near-infrared range than in the far-infrared. The agreement of experimentally observed line intensities with those presented in these line lists is within 10% for about 67% of fitted lines for both line lists. It should be noted that a large number of low-intensity lines are involved in comparison in near-infrared frequency range, which were beyond the measurements sensitivity in the far-infrared.

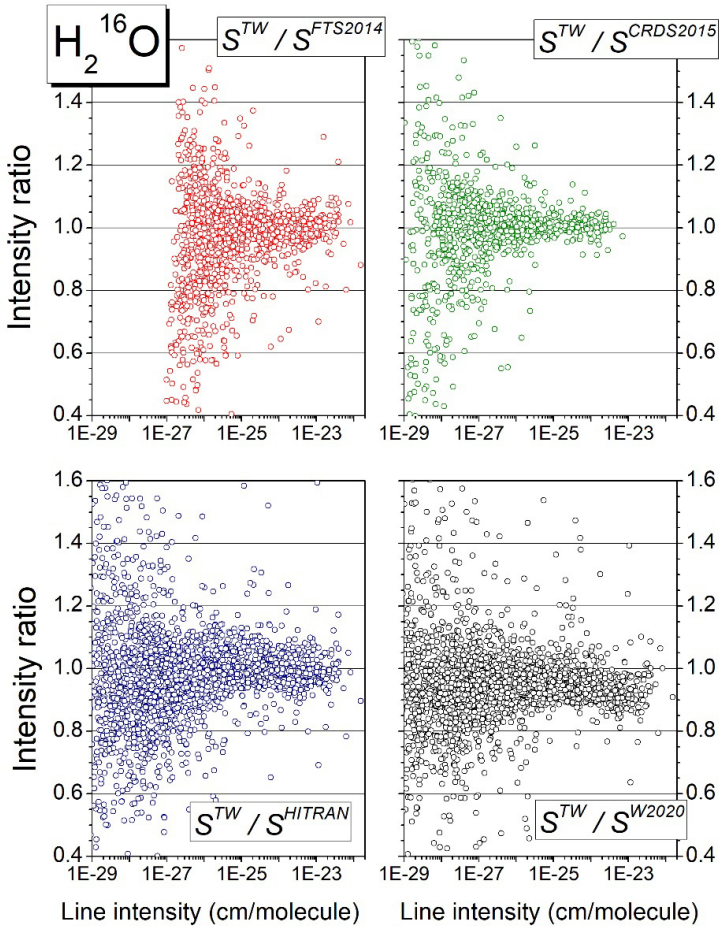

Fig. 2.20.

Ratios of measured in this work by CRDS $H_2{}^{16}O$ line intensity values (S^{TW}) to corresponding intensities from other sources: FTS2014 ($S^{FTS2014}$), CRDS2015 ($S^{CRDS2015}$), HITRAN2020 (S^{HITRAN}) and W2020 (S^{W2020}).

Figure 2.20 for the main water isotopologue shows that significant fraction of W2020 line intensities is overestimated in the near-infrared (all measured lines were involved in this comparison). The mean ratio of fitted intensities to W2020 intensities is 0.94, while for HITRAN2020 intensities it is very close to 1. The analysis of the intensity ratios for different vibrational bands shows that the average deviation depends on vibrational band and is larger for those involving the bending mode ν_2 and its overtones as illustrated on **Fig. 2.21** on example of, $\nu_1+3\nu_2$ and $3\nu_2+\nu_3$. (The systematic overestimation of W2020 intensities is 10%). For the two latter bands, HITRAN intensities are in satisfactory agreement with experiment, although have a larger dispersion. An additional problematic band both for HITRAN and for W2020 is $2\nu_1+\nu_2$.

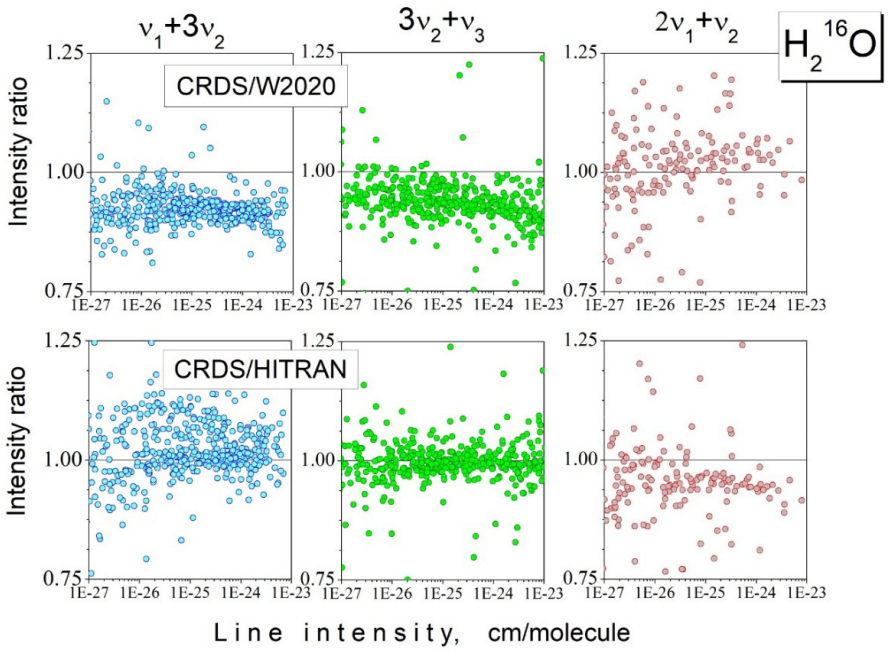

Fig. 2.21.

Ratios of the CRDS intensity values to the W2020 and HITRAN2020 intensities for $H_2{}^{16}O$ transitions of the $\nu_1+3\nu_2$, $3\nu_2+\nu_3$ and $2\nu_1+\nu_2$ bands measured in the 8041 – 8633 cm^{-1} interval.

As significant part of the observed deviations exceeds experimental uncertainty, experimental intensity values should be preferred for most of the lines in the region. **Figure 2.22** shows the most typical examples of the disagreement of experimentally retrieved intensities with HITRAN2020 and W2020 data for 6 spectral intervals (the rovibrational assignment of the problematic lines is given in the figure caption). Both lists can provide intensity values that differ several times from both experimentally determined ones and from each other.

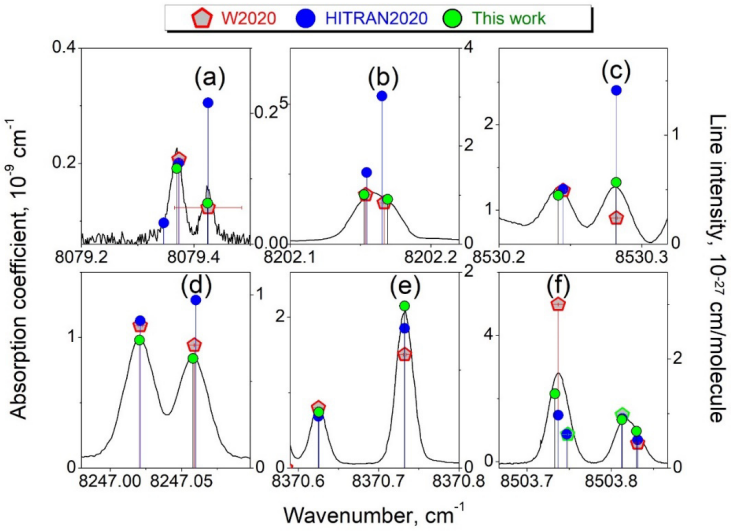

Fig. 2.22.

Examples of comparison of the H_2O spectrum diagram determined in this work (vertical bars with green circles) on the basis of the CRDS spectrum (solid line) with the W2020 (red pentagons) and the HITRAN2020 (blue circles) line lists. The right-hand intensity scale is adjusted to correspond approximately to the peak heights for each panel.

Conclusion

High quality FTS and CRDS spectra of natural water were recorded in the far-infrared (50-720 cm^{-1}) and near-infrared (8040-8620 cm^{-1}) spectral ranges. For both ranges, spectra contain water lines with intensities spanning more than five orders of magnitude. Voigt line profile was used for line fit in order to determine line positions and intensities.

In the far-infrared range, the high sensitivity (which allows to see the lines with intensities as weak as a few 10^{-26} cm/molecule) was achieved thanks to the high-power SOLEIL synchrotron radiation used as a radiation source and the multipass gas cell providing a 151.75-m absorption pathlength. Spectra were recorded at five different pressures up to 7 mbar which allows to cover the wide line intensity range between a few 10^{-26} and 10^{-19} cm/molecule. Frequency calibration was performed with the most accurate HITRAN2020 positions with declared accuracy better than 10^{-5} cm^{-1}. The accuracy of measured line positions is on the order of 5×10^{-5} cm^{-1} for isolated lines of intermediate intensity.

In the near-infrared range, the sensitivity of the used CRDS spectrometer allowed to observed lines with intensity down to a few 10^{-30} cm/molecule at a pressure of 1.33 mbar pressure. The use of a self-referenced frequency comb supplied an absolute frequency scale for the spectra.

Line positions and intensities were determined for about 3000 lines in far-infrared and 5400 lines in near-infrared range. 450 of these lines in far-infrared and about one third of the assigned transitions

in near-infrared are newly measured. The first experimental determination of 81 rovibrational levels of $H_2{}^{16}O$, $H_2{}^{18}O$, $H_2{}^{17}O$, and $HD^{16}O$ based on near-infrared spectra is reported.

The high position accuracy on the order of 5×10^{-5} cm^{-1} for isolated lines of intermediate intensity is demonstrated in both frequency ranges. For the far-infrared range, the excellent coincidence of observed line positions with 14CoMaPi results should be underlined. The calculation based on the bending-rotation Hamiltonian method provides an averaging of a large amount of data available in the far-infrared range and represents experiment better than methods based on the calculation of the empirical energy levels system and the use of experimental data in a wider frequency range. The agreement of presented line parameters with HITRAN2020 and W2020 data is also satisfactory for both frequency ranges, although some "outliers" are observed. The agreement of presented data in near-infrared range with experimental results FTS2014 and CRDS2015 is better than agreement with theory. However, a systematic shift of line positions of the order of -8×10^{-4} cm^{-1} is found.

As for the intensities, the simplistic account of FTS spectral function limits its accuracy in the far-infrared range, although fit uncertainties are within 10% for 82% of observed water lines and observed lines intensities agree with HITRAN within 10%. In the near-infrared, fit uncertainties are within 10% for 67% of observed water lines, mean intensities uncertainty is about 13%. For this range, validation tests of the theoretical values of the line intensities against measured values show both band-by-band variations of the deviations on the order of a few % and line-by-line fluctuations within a given band.

Resulted experimental line lists supplemented by HITRAN2020 and W2020 line positions and intensities are available in supplementary materials of these papers. In both spectral ranges the measurements have allowed to evidence deviations compared to these databases and provided information for databases improvement.

In the far-infrared range, spectra were recorded with Olivier Pirali and Alain Campargue, the line parameters adjustment was performed by M. Toureille. In the near-infrared range, spectrum was recorded by Samir Kassi. The rovibrational assignment in both frequency ranges was performed by S. Mikhailenko.

Chapter 3. Water-related atmospheric continuum in the far- and near-infrared ranges

This chapter combines the results of water self- and foreign-continuum retrieving in the far- and near-infrared ranges. The overview of previous continuum studies in infrared range presented in **Fig. 3.1** (all of them are given in Table 1.1). This figure contains continuum data measured both by FTS (Podobedov, Burch and Baranov measurements, CAVIAR data and measurements performed in Tomsk) and CRDS. The difference between CRDS data and those that measured in Tomsk, reaching several orders of magnitude, reflects the difficulty of continuum measurements. Studied in this work frequency ranges are highlighted by grey. Previous data were absent to the time of present study in part of FTS range (200-350 cm^{-1}) and in CRDS range (8300-8600 cm^{-1}).

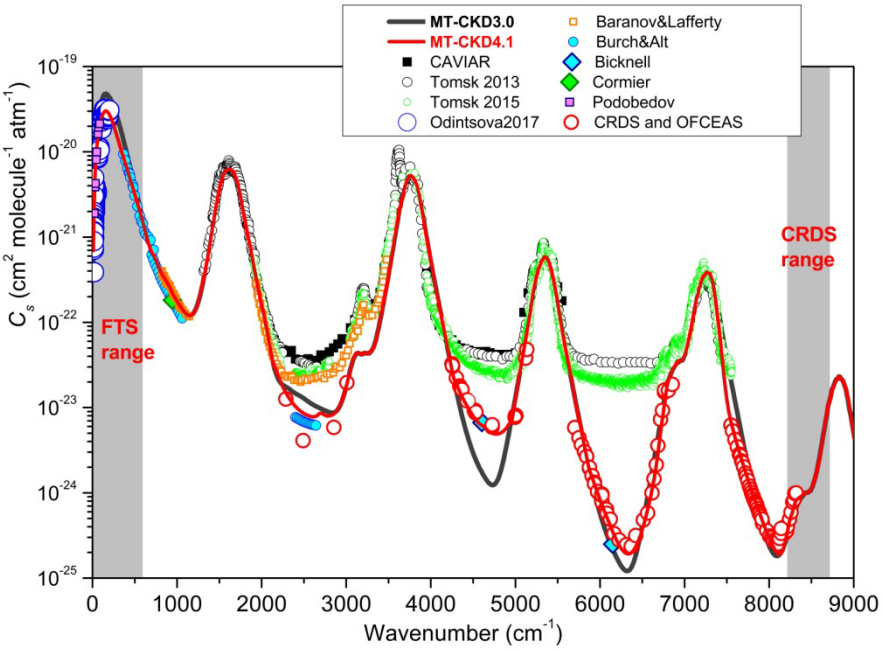

Fig. 3.1.

Overview of the water vapour self-continuum data in the infrared spectral region at close-to-room temperatures. Error-bars are not shown for clarity.

Note: the CAVIAR [Ptashnik2011] and Tomsk [Ptashnik2013,2015] room-temperature measurements had very high uncertainty in windows with error-bars varying from 50% (Tomsk) to 90% (CAVIAR) and so, were considered by the authors as very rough estimations of the continuum absorption in windows.

Retrieving the weak continuum against the background of the intense water resonance spectrum required to maintain high stability of the sample conditions during measurements. It is additionally complicated by adsorption and desorption effects strongly impacting experiments with water vapour. Numerous checks during the recordings are necessary to confirm the reliability of the obtained data, including experimental checking of continuum pressure dependences, water quantity, water partial

pressure stability in the gas mixture and repeatability of spectra. In addition, comparison of the obtained results with the available theoretical calculations and previous measurements are necessary.

Despite the difference in experimental setups, the procedure adopted for the continuum retrieval is similar in the far- and near-infrared ranges. Continuum pressure dependencies (quadratic for self-continuum and linear on the product of water and foreign gas partial pressures for foreign-continuum, according to **Eq. (1.16)**) were used to determine both the self- and foreign-continuum cross-sections and to check data quality and consistency. This is discussed in detail in **Sect. 3.1**. **Section 3.2** is devoted to self-continuum retrieval in both frequency ranges and comparison of obtained results with literature data. **Section 3.3** discusses foreign-continuum retrieval at experimental conditions summarised in **Sect. 3.3.1**. It is complicated both by more complex total absorption composition (**Sect. 3.3.2**) and the absence in the HITRAN database of N_2- and O_2- broadening coefficients of water vapor lines (**Sect. 3.3.3.**). The resulted foreign-continuum cross-sections are presented in **Sect. 3.3.4** and compared with literature data in **Sect. 3.3.5**. The continuum uncertainties associated with the experimental procedure and data processing are discussed in **Sect. 3.4**. Finally, in **Section 3.5** we discuss the physical origin of the water self-continuum on the basis of our experimental results. In the far-infrared, a physically based continuum model is presented and tested on available experimental data. The model considers all the mechanisms of continuum formation (See **Sect. 1.1.1.2, 1.1.2**). Empirical coefficients of the model are determined using the experimental data obtained in this work and from other related studies. The data obtained in the near-infrared range allowed discussing a possible water dimer contribution to the observed continuum (**Sect. 3.5.2**).

3.1. Methodology of continuum cross-sections retrieving. Continuum pressure dependences

The high intensity of water resonance spectrum both in the far- and in near-infrared ranges prevents the global continuum retrieval as a difference between measured total absorption and the model of resonance spectrum. The insufficient accuracy of individual line parameters (especially broadening coefficients, see **Sect. 3.4**) leads to very high continuum uncertainty. But in well-chosen microwindows of transparency (local minima between intense resonance lines), the continuum relative contribution to the total absorption increases up to 70% and 50% in the far- and near-infrared ranges, correspondingly. At these frequencies the influence of resonance lines parameters uncertainties is minimal. That is why continuum absorption was retrieved in microwindows of transparency in both frequency ranges except for the subterahertz frequency range 15-35 cm^{-1} where relatively small number of monomer lines allows continuum extraction almost without gaps. The common methodology for selecting microwindows and a similar approach to continuum cross-sections determining combines four series of measurements with two different experimental techniques (FTS and CRDS, see **Sect. 1.2.1.** and **1.2.2**). Further, the choice of microwindows and experimental

conditions is explained for both frequency ranges together, with emphasis on similarities and differences.

The main difference between measurements in the far- and near-infrared ranges is following. In the far-infrared, H_2O spectra are recorded in a continuous frequency interval (as shown in **Fig. 3.2**) at number of pressures. **Fig. 3.2** shows "raw" far-infrared FTS spectra of radiation power recorded with synchrotron radiation passed through the gas cell with water vapor (studied spectrum) and without water vapour (called hereafter reference spectrum or a baseline). In the near-infrared range, the CRDS setup allows fixing the radiation frequency at the selected microwindow point and recording the total absorption pressure dependences. Such "direct" recordings are performed for increasing and decreasing pressure ramps in a gas flow regime to decrease water desorption and adsorption influence.

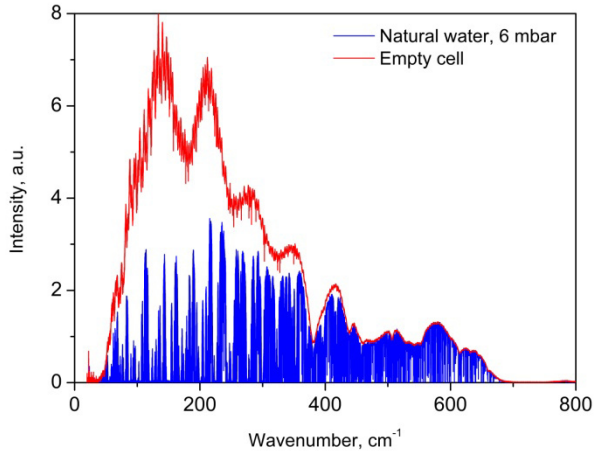

Fig. 3.2.

Transmission spectrum of natural water (blue) at a pressure of 4.5 Torr and corresponding background spectrum recorded with the empty cell (red).

The microwindows are selected at a distance from water line centres in both frequency ranges. The choice of microwindow frequency points is illustrated in **Fig. 3.3** on the CRDS spectra example. In the far-infrared range, chosen window should not be saturated. The saturation effect is clearly visible in **Fig. 3.2**. At 4.5 Torr, the pressure broadened H_2O resonance lines almost completely absorb radiation nearby the maximum of the water rotational band (100-300 cm^{-1}), masking a weak continuum component, which is clearly seen at the wing of the band (shown in the insert). To satisfy the unsaturation criterium the optical depth value should be is smaller than 10. In this case the continuum can be measured. It is not the case for most of microwindows nearby the maximum of rotational water band at chosen pressures. In the near-infrared range, high sensitivity of recordings revealed the presence of CO_2 and NH_3 as micro-impurities in the water vapour sample. Although their concentration is small (5 ppm for NH_3 and 120 ppm for CO_2), their strongest lines are visible in the spectrum (e.g., CO_2 and NH_3 lines are visible in **Fig. 3.3** at 8301.293 cm^{-1} and 8301.756 cm^{-1}). Impurities contribution to the total absorption at the chosen frequencies is less than 0.1 % and can be neglected.

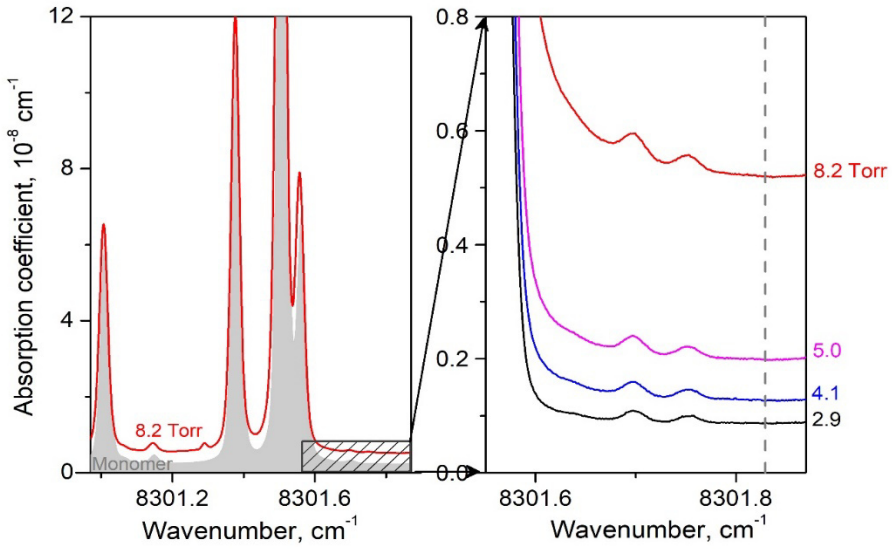

Fig. 3.3.

Left panel: The experimental CRDS H_2O spectrum at 8.2 Torr (solid curve) and a resonance absorption modelled using HITRAN2020 (grey area).

Right panel: Pressure dependence of CRDS spectra of pure water vapor near 8301 cm^{-1}, showing the increase of the water vapor self-continuum (the constant term due to the empty cavity losses was subtracted). The vertical dashed line corresponds to the spectral point at 8301.825 cm^{-1} selected for the continuum measurement.

As for a pressure choice, in both frequency ranges the maximum possible pressure is decided to be limited by about 70% of relative humidity of saturated steam pressure (about 15 Torr at a room temperature) to avoid water condensation leading to droplets formation on the cell windows. In addition, in the far-infrared range the upper water pressure was limited to 8 Torr to increase the number of usable (unsaturated) microwindows nearby the maximum of the H_2O rotational band. In the far-infrared range, the lowest H_2O pressure is chosen considering the fact that the continuum should be measurable against the background of water monomer lines, i.e. the continuum value must exceed the experimental noise. In the near-infrared range, pressure ramp recordings is started from zero pressure.

For foreign-continuum measurements, H_2O, N_2, O_2 and air pressures are chosen from the following considerations. (I) The foreign-continuum should have sufficient magnitude to be measured. (II) Spectrum should contain sufficient number of microwindows for measurements (collisionally-broadened lines eliminate microwindows at high pressures). In the far infrared range, the highest pressure is also limited due to unrepeatable change of the instrumental baseline at pressures above 320 Torr.

Note that water vapor concentration is varied differently in the far- and near-infrared ranges during foreign-continuum measurements. In the far-infrared range, the cell is filled with a given pressure of water vapour and then the foreign gas is gradually injected up to the maximum (total) pressure. Then the gas mixture is pumped out. Spectra are recorded at various pressure steps of the increasing and decreasing pressure ramps. The availability of broad-band spectra make it possible to

analyse resonance line profile and to control water pressure and isotopic composition. Experimental absorption coefficient is calculated using Eq. (1.18) in chosen microwindows to obtain total absorption and continuum absorption pressure dependences at selected wavenumbers.

For foreign-continuum measurements in the near-infrared range, water vapour generator (**Sect. 1.1.2**) produces the gas flow with constant water concentration of 1%. Following the fact that water foreign-continuum is proportional to the product of water and foreign gas partial pressures (Eq. (1.16)), this led to linear dependence of the foreign-continuum on the total pressure squared. Some measurements are repeated several times to check the repeatability. An example of recorded pressure ramps is given in **Fig. 3.4** for dry and humidified nitrogen, oxygen and air. It shows that increasing and decreasing data are perfectly superimposed that confirms the high stability of the experiment and reproducibility of measurements.

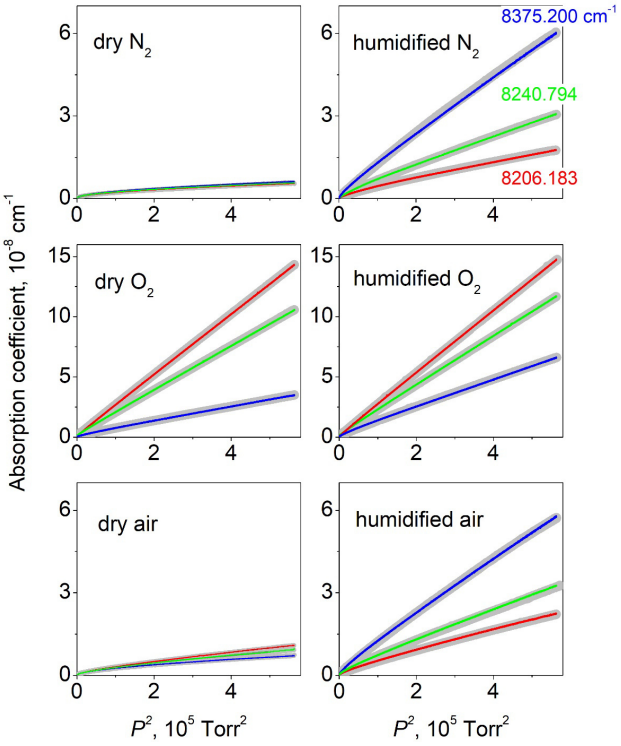

Fig. 3.4.

Variation of the absorption coefficient *versus* the total pressure squared, *P,* during pressure ramps up to 750 Torr for three spectral points of the 1.25 μm window (8206.183, 8240.794 and 8375.200 cm^{-1} - red, green and blue curves, respectively) for increasing and decreasing pressure ramps (grey and colored lines, respectively) at dry and humidified gas samples.

The content of this chapter is briefly summarised in Table 3.1.

Table 3.1. Continuum cross-sections retrieving methodology.

Frequency range		Far-infrared	Near-infrared
Spectrometer		FTS (Sect. 1.2.1.1.)	CRDS (Sect. 1.2.2.)
Recordings result		Spectra at series of pressure	Pressure ramps
Microwindows choice		At a distance from the intense water lines Not saturated	At a distance from CO_2 and NH_3 lines
Pressure choice		Less than 70% of relative humidity of saturated steam pressure Lower limit: Continuum is measurable Upper limit: Enough unsaturated microwindows	-
Pressure values	Self-continuum	1.5-4.5 Torr H_2O	0-15 Torr H_2O
	Foreign-continuum	15-320 Torr total pressure 1-15% H_2O	0-750 Torr total pressure 1% H_2O

3.2. Self-continuum

This chapter presents results of two experiments using FTS and CRDS techniques on self-continuum retrieving. Data treatment details are given in **Section 3.2.1.** Far-infrared range is divided here into subterahertz and superterahertz ranges (**Sections 3.2.1.1** and **3.2.1.2**) because the methods of continuum cross-section retrieving are different for these ranges. Comparison with literature data is given for all three ranges together in **Section 3.2.2.**

It was necessary to subtract resonance spectrum contribution from experimentally observed absorption to retrieve continuum. HITRAN line parameters available to date of data treatment and 25 cm^{-1} wings cut of (**Sect. 1.1.1.2** and **1.1.3**) for resonance spectrum calculations. In sub- and superterahertz ranges line profile Eq. (1.7) was used, in the near-infrared Voigt line profile (Eq. 1.9) was applied.

3.2.1 Self-continuum cross-sections retriewing

3.2.1.1. Subterahertz frequency range (15-35 cm^{-1})

An example of raw FTS transmission spectra recorded with empty cell (called hereafter reference or background spectrum, baseline) and water sample are shown in **Fig. 3.5**. The H_2O resonance spectrum (green trace in **Fig. 3.5**) was simulated as a product of the reference spectrum with transmittance obtained using profile Eq. (1.7) and HITRAN line parameters. Spectral range where continuum could be retrieved (15-35 cm^{-1}) is narrower than the total range available from the FTS recording because of insufficient radiation power at the edges of the range (**Fig. 3.5**).

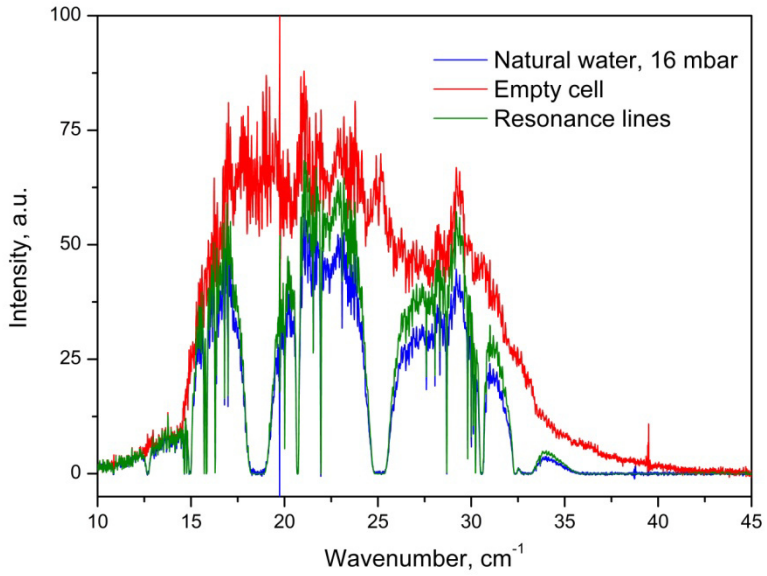

Fig. 3.5.

Synchrotron power transmitted through the empty cell (red), cell filled with water (blue) and simulation corresponding to the resonance absorption of H_2O (green). The spectra were recorded with a 0.02 cm^{-1} resolution.

The average of four reference spectra recorded one by one (see **Sect. 1.2.1.3**) was used for the continuum analysis. For checking continuum pressure dependence, water spectra were recorded only at two pressures for natural water (8.2 and 12 Torr) and two pressures for ^{18}O-enriched water (9.75 and 11.25 Torr) because of limited synchrotron time allocated to this study. Derived self-continuum cross-sections for natural water are in good agreement with each-other and with previous measurements as illustrated in **Fig. 3.6**. Gaps in the spectrum correspond to intervals obscured by strong water lines (optical depth larger than 1.5).

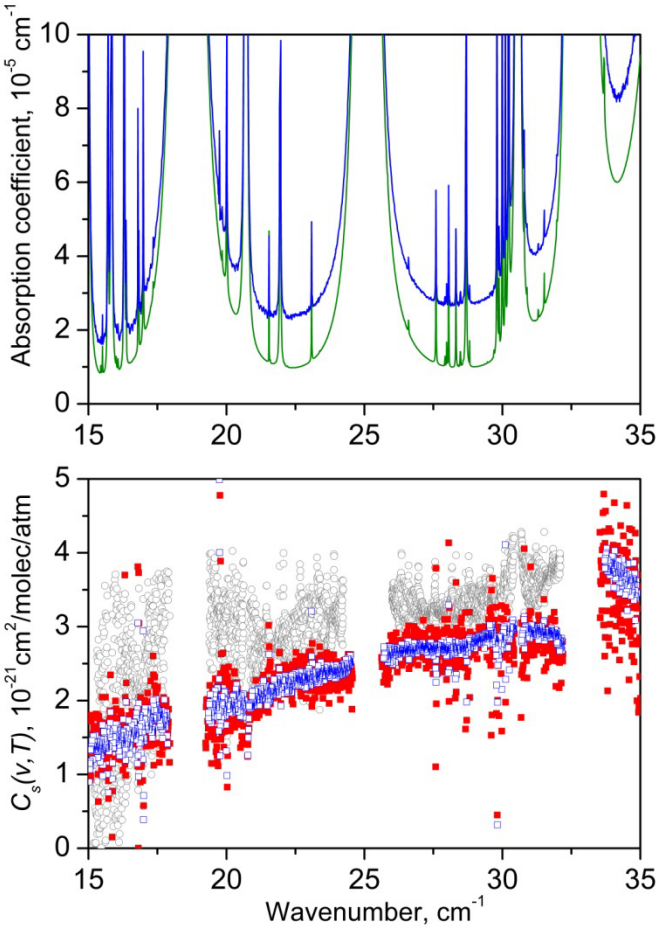

Fig. 3.6.

Upper panel: FTS water vapor absorption spectrum recorded at 296 K and 12 Torr (blue trace), calculated water resonance absorption spectrum using the HITRAN2016 database [Gordon2017] (green).

Lower panel: Derived water vapor self-continuum cross-sections from the 12 Torr (blue) and 8.2 Torr (red) recordings and comparison to the previous values reported in [Odintsova2017] from 11.25 Torr recording (grey).

Previous continuum measurements for ^{18}O-enriched water are absent. However, the expected coincidence within a noise level between results for natural water and ^{18}O water is shown on **Fig. 3.7**. (This is because the interaction potential of two water molecules is the same for these isotopologues.) The end-over-end rotation spectrum of $(H_2{}^{18}O)_2$ dimer can be roughly predicted shifted by about 1–2 cm^{-1} down from the $(H_2{}^{16}O)_2$ dimer spectrum because of larger molecular mass. However, the SNR of our data is not sufficient to evidence such small isotopic shift of the continuum.

Obtained self-continuum cross-sections are available in supplementary materials associated with [Odintsova2019].

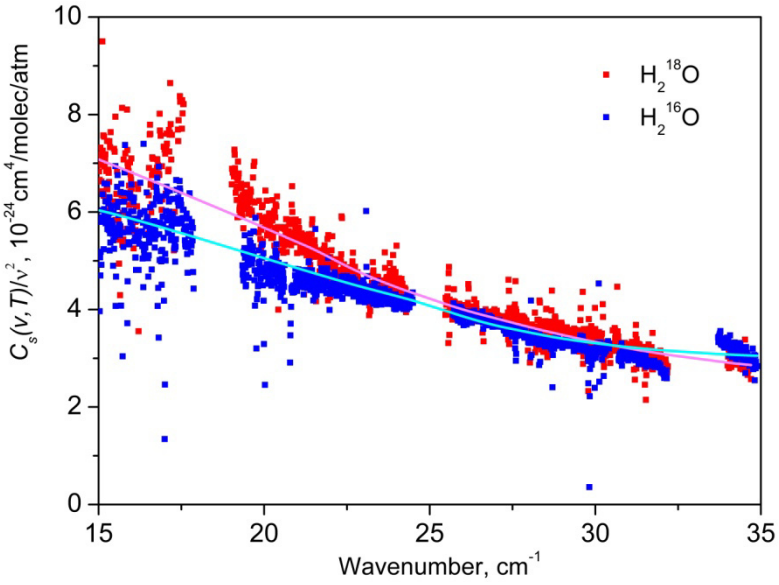

Fig. 3.7.

Comparison of $H_2{}^{16}O$ and $H_2{}^{18}O$ normalized self-continuum cross-sections, $C_S(\nu)/\nu^2$. Blue and red symbols correspond to $H_2{}^{16}O$ and $H_2{}^{18}O$, respectively (both obtained from water vapor recording at 12 Torr). Light blue and magenta curves correspond to a smoothing of the $H_2{}^{16}O$ and $H_2{}^{18}O$ data, respectively.

3.2.1.2. Superterahertz range (50-500 cm^{-1})

In the range 50-500 cm^{-1}, two series of water vapor spectra were recorded with different resolution. The first series contains 5 spectra at pressures between 3 and 4.5 Torr for natural water and 7 spectra at pressures between 1.5 and 4.5 Torr for ^{18}O enriched water with 0.02 cm^{-1} resolution (low-resolution spectra). This set allows checking continuum pressure dependence and use it for self-continuum cross-section retrieving. The second series contains spectrum at 3.75 Torr for natural water and two spectra at 2.25 and 3.75 Torr for ^{18}O enriched water with 0.002 cm^{-1} resolution (high-resolution spectra). This series allow to see water continuum band shape in more details. Experimental conditions are summarised in Table 3.2.

Table 3.2. Experimental conditions for continuum recordings in superterahertz range

Sample	*P*, Torr	Resolution, cm^{-1}	Acquisition number
Natural water	4.50	0.02	200
	4.12		200
	3.75		200
	3.00		200
	2.25		200
	4.50	0.002	380
^{18}O enrichment	4.51	0.02	200
	4.09		
	3.75		
	3.38		
	2.99		
	3.62		
	2.25		
	1.49		
	2.99	0.002	200
	4.49		

The continuum was obtained as a difference between measured absorption and simulated monomer spectrum using low-resolution spectra in 118 spectral points located in microwindows for natural water and in 127 spectral points for ^{18}O enriched water. **Figure 3.8** illustrates typical pressure dependence of the resulted continuum in three microwindows, which is in a good agreement with expected linear pressure dependence versus water pressure squared Eq. (1.16). Self-continuum cross-section was obtained after a linear fit of continuum pressure dependences using Eq. (1.16).

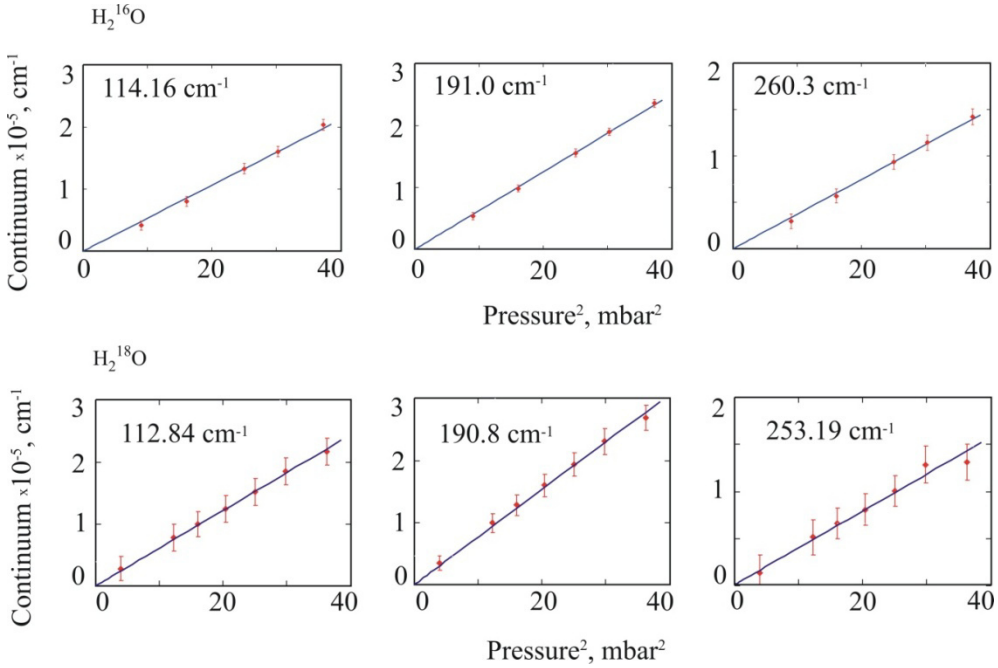

Fig. 3.8.

Self-continuum absorption coefficient for $H_2{}^{16}O$ (upper row) and $H_2{}^{18}O$ (lower row) *versus* pressure squared in three selected micro-windows. Error bars correspond to one standard deviation of the noisy signal from mean value within current microwindow.

The second set of recordings contains two spectra at 3 and 4.5 Torr with a high resolution of 0.002 cm^{-1}. It allows retrieving more detailed shape of continuum absorption, which is crucial for its

physical nature analysis. Continuum absorption was calculated directly in the same way as in subterahertz range (see **Sect. 3.2.1.1.**) as a difference between experimentally observed absorption and monomer line contributions within microwindows of transparency. The narrower instrumental function (see **Sect. 1.2.1.2**) allowed accounting better for the monomer contribution and thus enlarging the number of spectral points (about 6000 for each spectrum). **Figure 3.9** shows an excellent agreement between self-continuum cross-sections retrieved from continuum pressure dependences and from high-resolution spectra and thus validates these two approaches to apparatus function accounting. Coincidence of observed continuum from a spectra recorded at a different resolution validates our treatment of the apparatus function as described in **Sect. 1.2.1.2.**

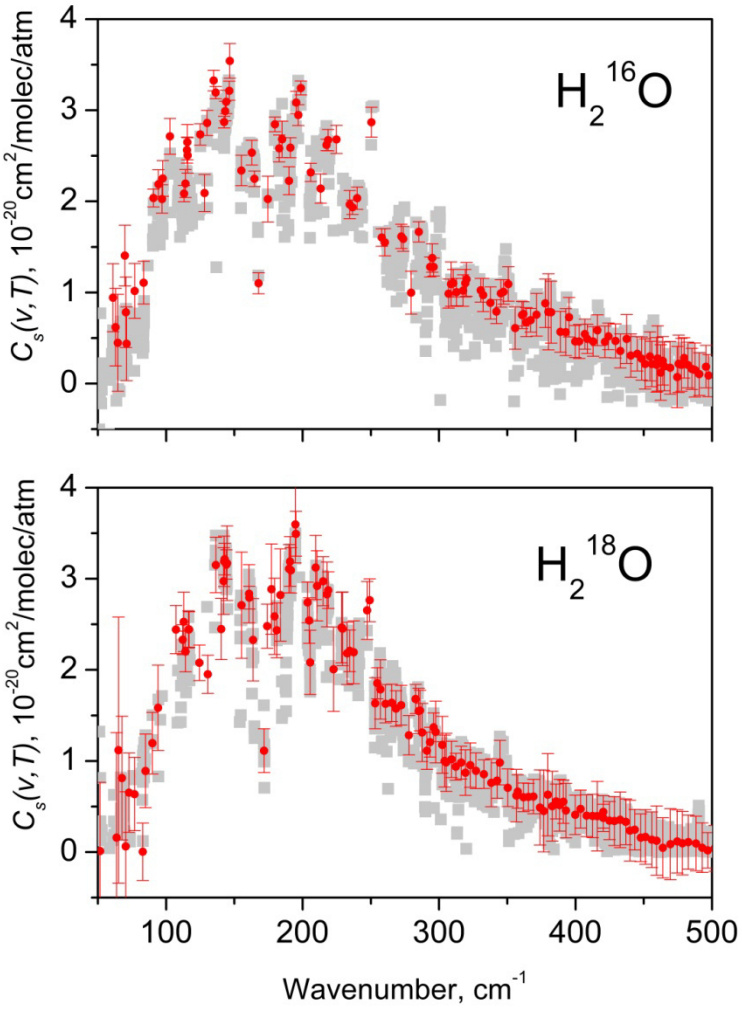

Fig. 3.9.

Self-continuum cross-sections retrieved from high resolution water vapor spectra recorded at 3 Torr (grey squares). The red circles correspond to values derived from the analysis of the quadratic pressure dependence of the absorption in micro-windows selected in lower resolution recordings. Error bars correspond to one standard deviation of the noisy signal from its mean value within current microwindow.

As expected, the $H_2{}^{16}O$ and $H_2{}^{18}O$ absorption continua are very similar in shape and magnitude. This is an additional verification of the quality of the experimental data.

Obtained self-continuum cross-sections are available in supplementary materials associated with [Odintsova2019].

3.2.1.3. Near-infrared range (8290-8620 cm^{-1})

As described in **Sect. 3.1**, measurements were performed at fixed frequencies in the microwindows for increasing and decreasing pressure ramps. **Figure 3.10** shows typical total variation of the absorption during pressure ramps. The coincidence between increasing and decreasing pressure ramps is excellent. It indicates the absence of potential systematic errors.

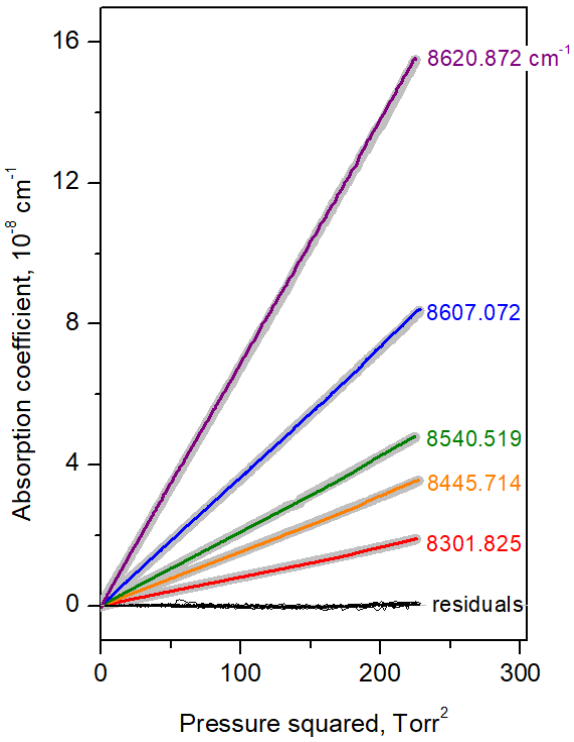

Fig. 3.10.

Self-continuum absorption *versus* the squared water vapor pressure during increasing (in gray) and decreasing (in different colours) pressure ramps up to 15 Torr at different frequencies of the 1.25 μm window of transparency. The residuals (in black) correspond to the superposition of differences between measurements and corresponding five fitted linear functions.

The total absorption in microwindows consists of the continuum and resonance line wings contributions, both behaving quadratically *versus* H_2O pressure at large detuning from line centre. Rayleigh scattering loses (which are linearly proportional to pressure) are less than two orders of magnitude smaller than the total absorption and thus could be neglected. That is confirmed by perfect linear dependence of the total absorption versus pressure squared (see residuals in **Fig. 3.10**). The total

absorption cross-section is obtained from fit of these dependences by a linear function. Self-continuum cross-section results from subtraction of water lines contribution from the total absorption cross-section.

Figure 3.11 allows to compare the retrieved self-continuum and the total measured absorption cross-sections. The difference between them is the resonance spectrum contribution. This contribution is between 30 and 70% from the total depending on frequency. The large variations of the total absorption cross-section within the studied range are mostly due to the resonance spectrum. After subtraction, the continuum frequency dependence is smoother.

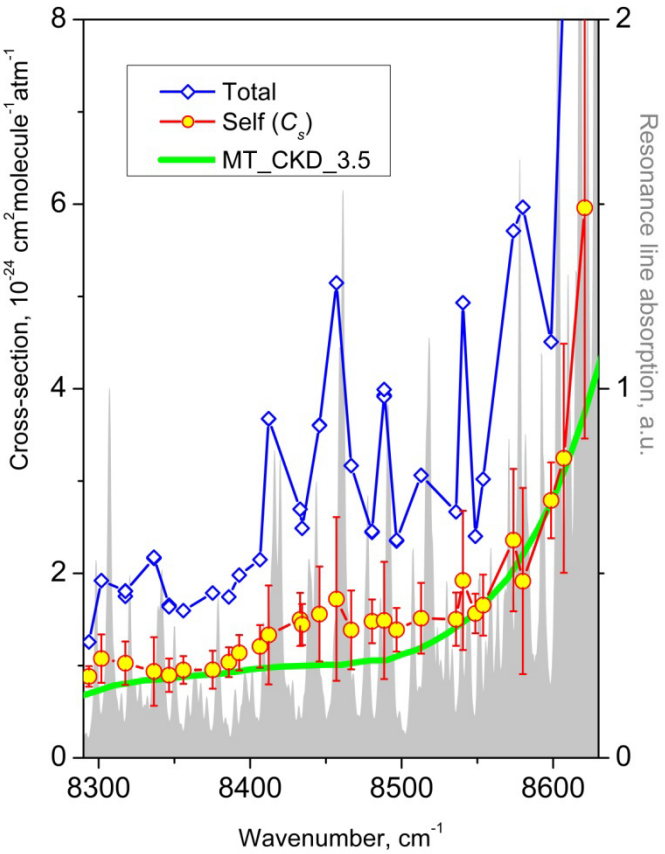

Fig. 3.11.

Total measured absorption cross-section of water vapor at room temperature (blue) at the measurement points selected in the 1.25 μm window. The retrieved H_2O self-continuum absorption cross-sections (yellow open circles) which are plotted with their associated error bars (dominated by the uncertainties of the resonant lines contribution). The MT_CKD_3.5 self-continuum model (green line) [https://github.com/AER-RC/MT_CKD/]. For comparison, a low resolution simulation of the resonance H_2O absorption spectrum is presented as gray background in arbitrary vertical scale.

CRDS technique provides an uncertainty of total absorption measurement better that 1%. However, the error bars of the retrieved continuum are much larger due to resonance lines parameters uncertainty. This problem will be discussed in details in **Sect. 3.4.**

Retrieved self-continuum cross-sections presented in **Table 3.3** for each spectral point together with their uncertainties related to experiment and resonance spectrum subtraction and numbers of scans (The same as Table 1 from [Koroleva2022]).

Table 3.3.
Self-continuum cross sections derived between 8293 and 8621 cm^{-1}.

Frequency cm^{-1}	C_s [a] 10^{-24} $cm^2 molecule^{-1}$ atm^{-1}	R_{WML} [b] %	C_s Unc [c] %	Nb of ramps
8293.592	0.883(1)	29.7	12.6	1
8301.825	1.076(1)	44.0	24.3	2
8317.615	1.026(27)	42.7	22.8	3
8336.464	0.937(7)	56.8	39.7	2
8346.523	0.896(9)	45.6	20.2	2
8355.863	0.953(2)	40.3	15.7	1
8375.201	0.955(3)	46.6	21.6	1
8385.874	1.038(3)	40.5	15.5	1
8392.751	1.140(3)	42.5	16.8	1
8406.511	1.208(3)	42.5	19.2	1
8412.218	1.333(3)	63.7	40.2	2
8432.946	1.501(3)	44.3	19.2	1
8434.240	1.446(3)	41.9	15.4	1
8445.714	1.559(3)	56.8	33.0	2
8456.934	1.722(3)	66.5	51.5	1
8466.674	1.386(3)	56.3	30.8	1
8480.505	1.480(7)	39.6	16.0	2
8488.515	1.49(3)	62.2	42.6	4
8496.624	1.388(6)	41.1	17.0	2
8512.892	1.513(2)	50.6	25.3	2
8535.871	1.503(4)	43.6	19.2	1
8540.519	1.923(3)	61.0	39.2	1
8548.646	1.565(3)	34.9	13.7	2
8553.827	1.656(3)	45.2	19.9	1
8573.765	2.360(4)	58.7	32.7	1
8579.992	1.916(3)	67.9	52.7	2
8598.690	2.791(4)	38.1	14.7	1
8607.072	3.247(4)	61.9	38.2	1
8620.872	5.960(68)	62.8	41.9	3

Notes
[a] The statistical uncertainties are given within parentheses after each *Cs* value, in the unit of the last quoted digit. They include the fit uncertainty and statistical uncertainty (for the frequencies where measurements were repeated – see last column). The uncertainties related to the resonant line subtraction are much larger and included in the column total uncertainties given in the "C_s Unc." column.
[b] Relative contribution of the far-wing contribution to the total measured absorption coefficient: $\alpha_{WML} = \alpha_{WML}/(\alpha_{WML}+\alpha_{WCS})$.
[c] Total uncertainty on the retrieved C_s values (in %) mainly due to uncertainty on the (subtracted) far-wing, α_{WML} (see Text).

3.2.2 Comparison with literature

Previous experimental studies of water vapour self-continuum in the frequency ranges under consideration are summarised in Table 1.1 both for far- and near-infrared ranges. Let us recall [Podobedov2008] and [Slocum2015] measurements and unpublished results obtained by R. A. Bohlander and reported by Burch [Burch1981] in low-energy wing of water rotational band and Burch measurements above 350 cm^{-1} [Burch1982]. Although present data does not cover the results reported

at lower frequencies [Liebe1987, Kuhn2002, Koshelev2011] these data are added to the comparison as well. In the near-infrared range, previous continuum measurements were performed by the same CRDS setup at lower frequencies [Campargue2016]. At higher frequencies FTS measurements at higher temperatures [Simonova2022] are available. For proper comparison, the continuum data obtained at elevated and lowered temperatures should be recalculated to 296 K using measured continuum temperature dependences.

For the far-infrared range, the comparison of C_S values is shown in **Fig. 3.12**. Present results are part of series of SOLEIL self-continuum measurements [Odintsova2017, Odintsova2019, Odintsova2020]. Present data agree with first results of this series [Odintsova2017] limited to the 40–200 cm^{-1} range. Measurements from this work fill the 200–350 cm^{-1} gap, where the water vapor continuum was not investigated before. Subsequent study [Odintsova2020] confirms presented data near the continuum band maximum. However, data from [Odintsova2020] were recorded at higher H_2O pressures up to 12 Torr (producing stronger continuum) thanks to that they are more accurate in the high-frequency part of the studied range. The use of higher H_2O pressure allowed also to extend the range of the continuum measurements up to 700 cm^{-1}.

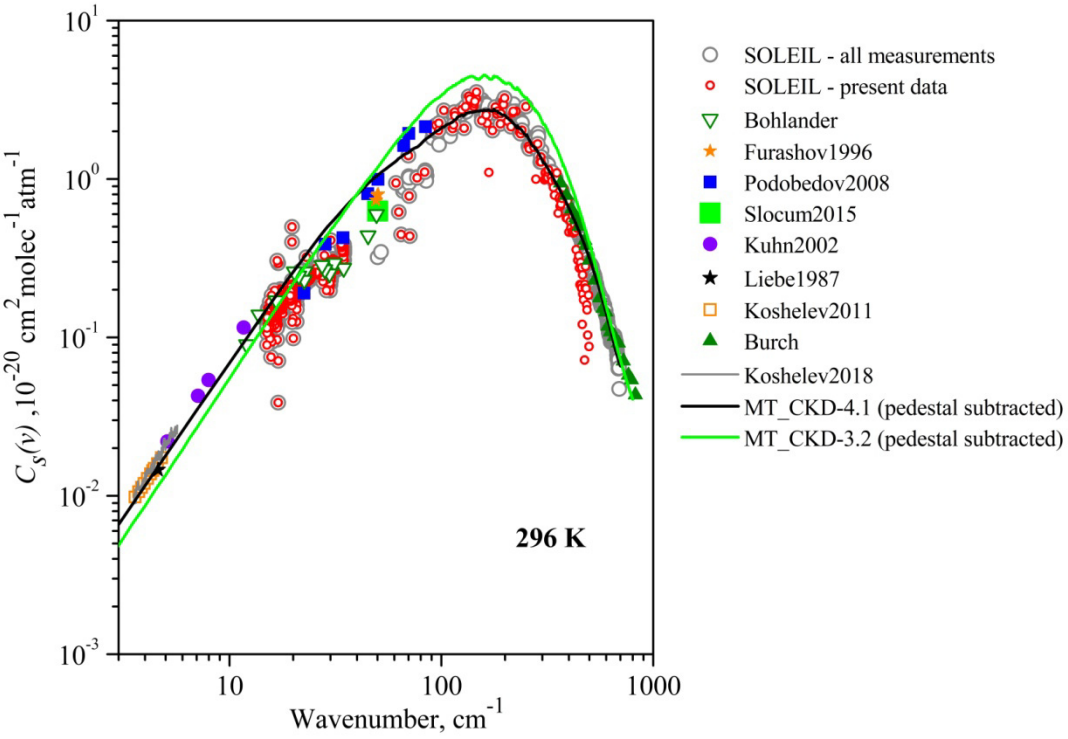

Fig. 3.12.
Self-continuum cross-sections determined in this work in comparison with literature data

Figure 3.12 illustrates the satisfactory agreement of the presented data with the previous measurements in this spectral range listed in Table 1.1. Presented C_{self} values in the 15 – 35 cm^{-1} range agree with the results of [Burch1981, Podobedov2008]. In the range of 50.3 – 84.1 cm^{-1}, new $C_{self}(\nu)$

values are smaller than reported in [Burch1981, Furashov1996, Podobedov2008, Slocum2015] by a factor between 1.5 and 2, respectively. These deviations can be explained by the measurements uncertainties: SOLEIL values were obtained from low signal-to-noise ratio spectra at the edge of the working range of the synchrotron mode. Note that the data from [Podobedov2008] and [Burch1981] also show a large dispersion reflecting their uncertainties.

Measured C_{self} data were used to refine the MT_CKD model [Mlawer2023]. The updated MT_CKD-4.1 version gives a continuum value 30% smaller in the region of its maximum. Note that the "plinth/pedestal" under resonance lines was attributed in the present work to the water resonance spectrum and not to the continuum as it is accepted in the MT_CKD model. For proper comparison, the contribution of this "plinth" was subtracted from the MT_CKD continuum in **Fig. 3.12** continuum.

In the near-infrared range, the comparison of retrieved C_{self} with previous experimental data and the MT_CKD-3.5 model is presented in **Fig. 3.13**. The first three newly measured spectral points coincide with those of [Campargue2016]. At these wavenumbers, the present results exceed previous one by 6.3, 8.4 and 6.5%. About a half of this difference is due to using different versions of HITRAN line list for continuum retrieval. Resonance absorption modelled with HITRAN2012 (as in [Campargue2016]) is larger by about 3% compared with HITRAN2020. Taking that into account, new measurements are in agreement with previous one within combined uncertainty (see Table 3.3).

Measured C_{self} data validates MT_CKD-3.5 model towards high frequency edge of the 1.25 μm window. The model was refined below 8300 cm^{-1} taking into account data from [Campargue2016], but at higher wavenumber it is identical to the previous version [Mlawer2023]. The comparison with the MT_CKD model reveals some additional absorption near 8455 and 8300 cm^{-1}, which will be discussed in **Sections 3.4** and **3.5**.

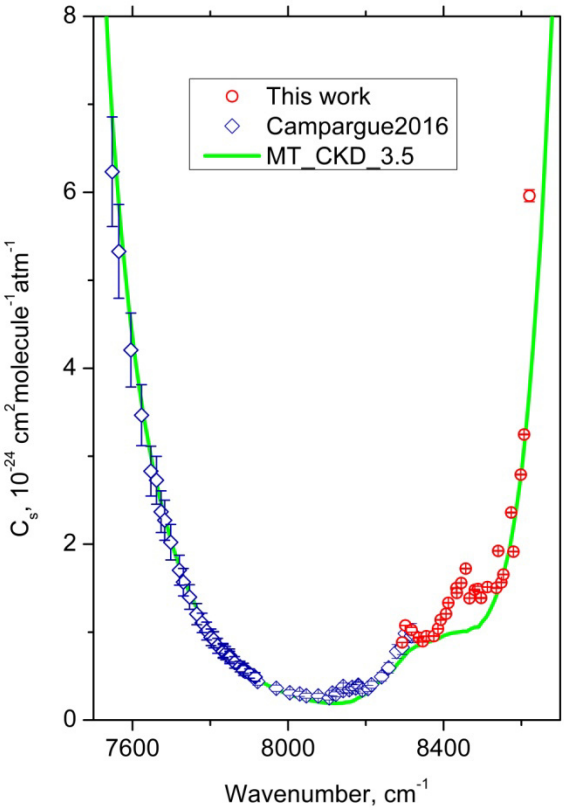

Fig. 3.13.

Self-continuum cross-sections of water vapor at room temperature in the 1.25 μm window. The experimental values measured in [Canpargue2016] and in this work (blue and red circles, respectively) are compared to the MT_CKD_3.5 values (solid green curve). Note that the plotted error bars do not include the (large) contribution due to the resonant line parameters

The present measurements overlap with [Simonova2022] data obtained at 398 and 431 K in 8500-8620 cm^{-1} interval. These data are obtained with FTS technique at several pressures between 750 and 3117 Torr. Simonova et al. presents the continuum model suggested that the continuum is formed mainly due to the absorption of water dimers. Knowledge of the dimer spectrum temperature dependence [Leforestier2014] allows extrapolating high-temperature measurements [Simonova2022] to room temperature. **Fig. 3.14** shows that, similarly to observations in 1.6 μm window [Mondelain2014], the 398 K and 431 K extrapolations are close to each other but in about 2 times above presented room temperature C_{self}. Based on the results of fitting of the dimer model in [Simonova2022] to experimental data, they suggested a possible significant contribution from another (non-dimer) absorption mechanism to the self-continuum in this spectral region (including line wings [Serov2017]). This may decrease the final temperature dependence of the self-continuum absorption as compared to the pure water dimer prediction in [Leforestier2014] and so, to explain this difference with our data.

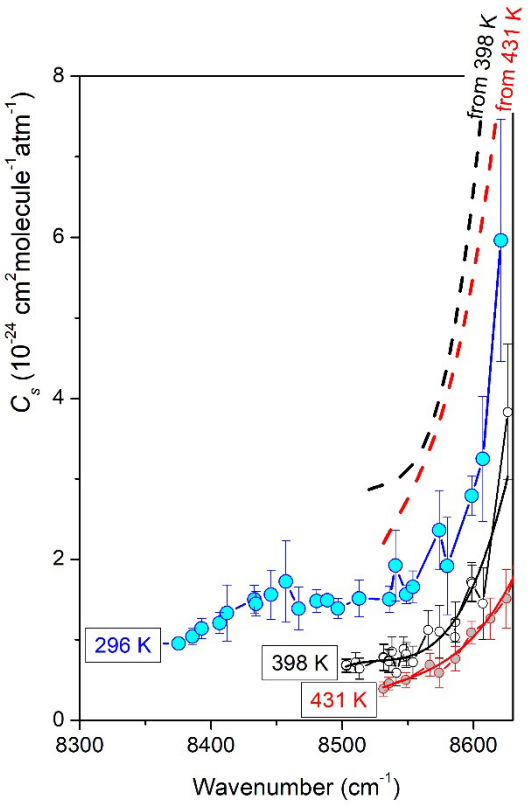

Fig. 3.14.

Self-continuum cross-sections of water vapor between 8375 and 8630 cm^{-1} measured at room temperature in this work (blue circles) in comparison with data from [Simonova2022] obtained at 398 K and 431 K (black and red circles, respectively; solid curves correspond to their approximations by smooth dependences). Black and red dashed lines are extrapolations of the 398 K and 431 K datasets to 294 K using exp(D_0/kT) temperature dependence (see **Sect. 1.1.4**). Error bars include the contribution of resonant lines for all datasets.

3.3. Foreign-continuum

3.3.1. Experimental conditions and pressure stability

As it was underlined in **Sect. 3.1**, experiments on foreign-continuum retrieving were completely different in far- and near-infrared ranges not only due to different experimental setup, but also because the pressure in the cell had to be changed in different ways. However, high sensitivity of the continuum value to water vapor pressure requires checking the influence of adsorption and desorption effects and monitoring the water pressure during measurements. It is performed by this was performed by determining the integrated absorption coefficient of isolated water vapor lines in both frequency ranges. However, due to the high foreign gas pressures and water lines density, only a few dozen of lines are usable for water pressure determination both in far- and in near-infrared ranges.

This chapter gives more details on experimental conditions and presents the results of water pressure determination performed in the same way both for far- and near-infrared.

Experimental conditions for foreign-continuum recordings in the far-infrared range are summarised in **Table 3.4**. Five experimental series were performed for H_2O-N_2, H_2O-O_2, H_2O-air foreign-continuum. During each recording series, the cell was filled with water vapour, and then foreign-gas gas was gradually added to the maximum total pressure. After that gas mixture was step-by-step pumped out. Both gas filling and pumping were made slow enough to maintain thermodynamic equilibrium. Spectra were recorded after each change of pressure during the increasing and decreasing pressure. Water vapor and foreign gas pressure were assumed to be independent during the pressure increase and proportional during the pressure decrease.

Table 3.4. Experimental conditions for the far IR study.

Foreign gas Gas purity, %	Nitrogen 99.9999			Oxygen 99.9995	Dry air 99.999
Radiation source	globar	synchrotron			
Series number	1	2	3	4	5
Number of pressure points	9	11	8	12	7
Filling H_2O pressure, Torr	2.2	1.5	3	3	3
Min./max. total pressure, Torr	15/75	30/150	75/323	150/300	150/300
Number of acquisitions	200-400	200	100-200	200	200

To check the pressure value in the far-infrared range, water lines were chosen from the same experimental recordings, which were used for the continuum cross-sections retrieval. The expected water content is generally confirmed (**Fig. 3.15**). However, the change of partial water pressure within a few percents could not be revealed even for the best experimental series due to the large uncertainty of the retrieved data.

In the near-IR range, the water vapor generator produced a gas with a constant preset humidity, therefore, both during the filling and pumping of the cell, the pressure ratio of water vapor to foreign gas were constant and equal to 1%. Total pressure in the cell was changing with a speed of about 1 Torr/s up to 750 Torr. Pressure dependence of absorption of gas in the cell was recorded directly at each fixed frequency.

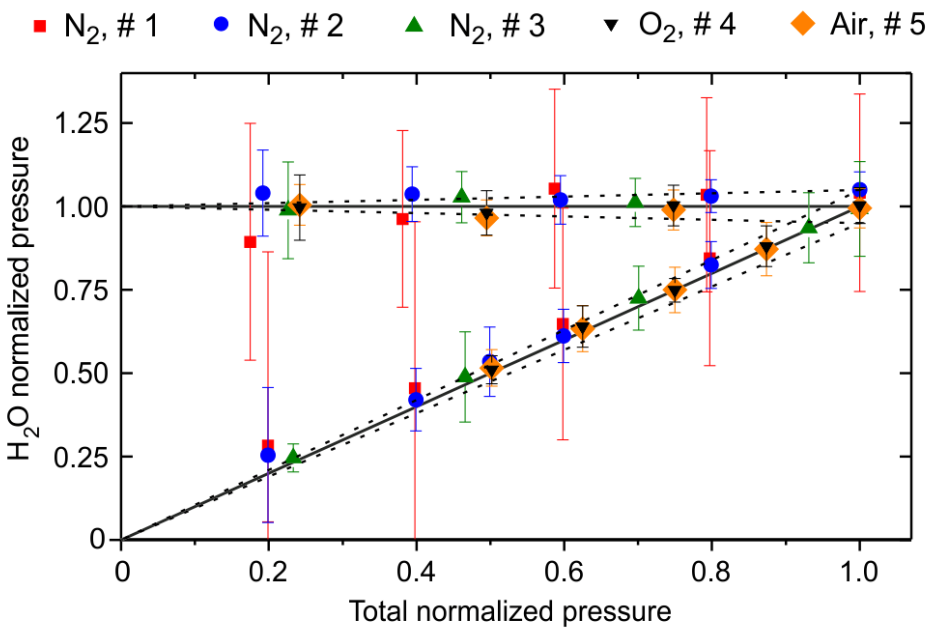

Fig. 3.15.

Expected (solid lines) and spectroscopically determined (symbols) water vapour partial pressure normalized by its measured value at the cell filling *versus* total pressure of the gas mixture normalized by its the maximum value for the increasing (horizontal) and decreasing (inclined) pressure ramps. Each symbol represents one spectrum at given pressure from series of measurements as described in Table 3.1. Error bars correspond to 1σ uncertainty. Dashed lines show uncertainty of water content assumed for the analysis.

Additional frequency scans were recorded in a narrow frequency intervals (several cm^{-1}) at pressures of 250, 500 and 750 Torr to check water concentration in the gas cell. Examples of such recordings are shown in the left panel of **Fig. 3.16**.

In the CRDS setup, water pressure in the cell occurs to be systematically less than the preset value on water vapour generator. We assume that part of water vapour was adsorbed in thin metal tubes used to supply gas to the spectrometer cell. The result of water pressure spectroscopic determination at 750 Torr total pressure from the eight lines broadened by O_2, N_2 and air is plotted on the middle panel of **Fig. 3.16** *versus* the intensities of corresponding lines. The obtained partial pressure differs from its nominal value by about 15%. The weighted average value of the experimentally determined partial water pressure was used for the pressure correction factor determination. The weight of each pressure value was calculated as the square root of the sum of squared experimental noise, fit uncertainty and HITRAN intensity uncertainty. Linear correction was assumed. The pressure correction function is shown in the right panel of **Fig. 3.16** together with experimentally retrieved water pressures. This correction was applied for all pressure ramps analysis. This correction influence significantly to obtained foreign-continuum cross-sections value (see **Sect. 3.3.4.2.**)

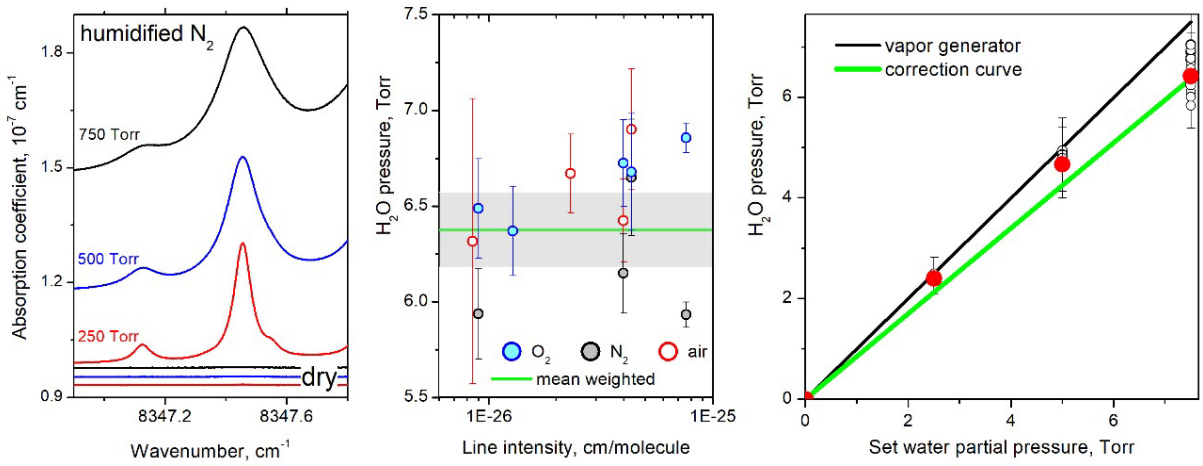

Fig. 3.16

Left panel: CRDS spectra of 1% humidified N_2. The three baselines at the bottom of the plot are the corresponding dry N_2 spectra (linear with pressure increase is due to Rayleigh scattering).

Middle panel: Water vapor partial pressure values retrieved from intensities of water lines broadened by N_2, O_2 and air at total pressure 750 Torr, *versus* their HITRAN2020 intensities.

Right panel: Water vapor partial pressures retrieved from the line profile analysis *versus* the nominal partial pressure (1% of the total). Red dots correspond to the line at 8347.46 cm^{-1} presented in the left panel. The pressure correction curve (green straight line) as determined from experimental points.

3.3.2. N_2- and O_2- broadening coefficients estimation

To simulate resonance water lines broadened by nitrogen and oxygen, corresponding broadening coefficients are needed. The calculation results based on the semi-empirical Modified Complex Robert-Bonamy (MCRB) formalism were used [Gamache2019, Vispoel2019, Vispoel2020]. The same approach was used for calculating air-broadening coefficients for HITRAN.

At the time of data analysis in the far-infrared range only data from [Vispoel2019, Gamache2019] were available. Nitrogen and oxygen broadening coefficients were reported only for a limited number of water vapour lines, although all necessary (calculated) air-broadening coefficients were listed in the HITRAN database. For nitrogen, [Vispoel2019] presents broadening coefficients calculations for the three most abundant water isotopologues ($H_2{}^{16}O$, $H_2{}^{18}O$ and $H_2{}^{17}O$) for the transitions in the ground vibrational state for the total angular momentum quantum number $J < 23$. Oxygen broadening coefficients were provided for the pure rotational transitions of the main isotopologue, $H_2{}^{16}O$, with $J < 10$ [Gamache2019].

To obtain the N_2- and O_2-broadening coefficients for all other lines observed in the recorded spectra, two assumptions were used. For lines of H_2O isotopologues and rotational transitions in excited vibrational states unaccounted in [Vispoel2019, Gamache2019], the broadening coefficients

were considered to be the same as for corresponding $H_2{}^{16}O$ lines in the ground state. For each isotopologue, the approach based on the evaluation of broadening efficiency factors [Liebe1987] was used to obtain broadening coefficients for higher *J*. Ratios of the foreign gas broadening to air-broadening were determined for the lines with known foreign- and air-broadening coefficients (calibration lines) and assumed to be identical for all the transitions (**Fig. 3.17**). Line intensities were taken into account as the weight multipliers for corresponding lines broadening coefficients in the averaging procedure.

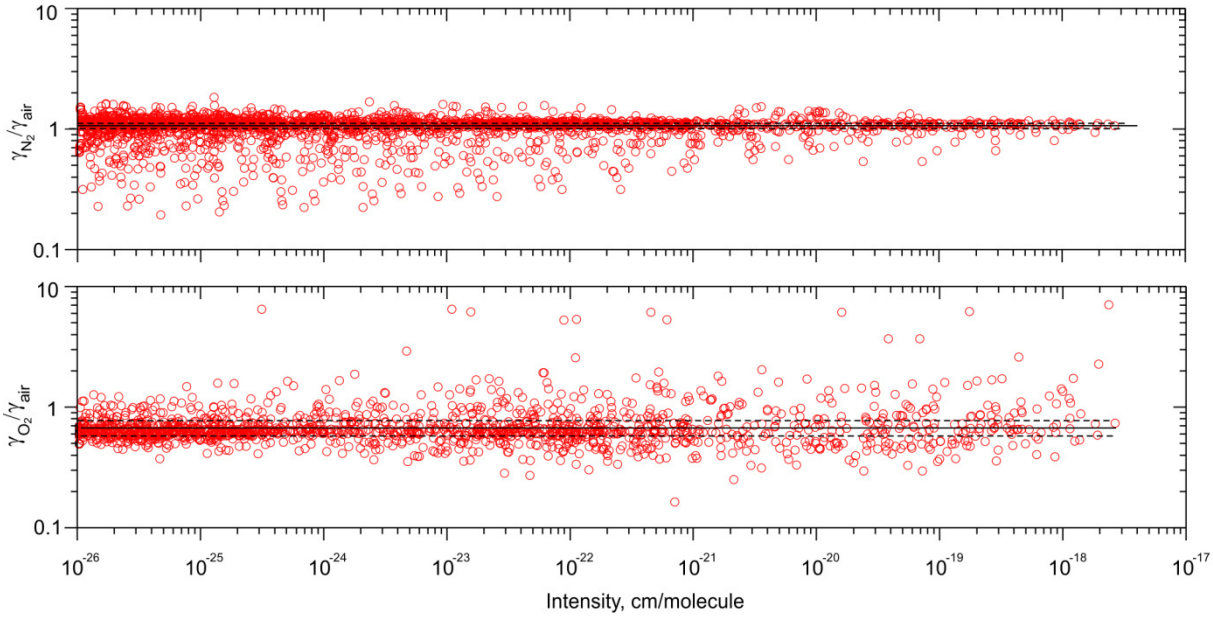

Fig. 3.17.

Ratio of nitrogen (upper panel) and oxygen (lower panel) broadening coefficients to air broadening vs. line intensity. Black solid and dashed lines are for determined mean weighted values of the ratio and mean weighted deviation, respectively.

The resulting ratios are 1.064(57) and 0.67(10) for N_2- and O_2-broadening, respectively. The consistency between them was verified based on standard atmospheric O_2/N_2 mixing ratio of 21/79 leading to an air-broadening coefficient $\gamma_{air} = 0.79\gamma_{N2} + 0.21\gamma_{O2} = 0.67(10)\text{x}0.21 + 1.064(57)\text{x}0.79 = 0.98(7)$. In the same way, the consistency of broadening coefficients for all the calibration lines was checked. The mean weighted by line intensity value of $0.79\gamma_{N2} + 0.21\gamma_{O2}$ was 0.971(43) (see **Fig. 3.18**). Deviation from the expected unity value is less than 10% for most lines but for number of lines it increases up to 50%. These deviations indicate necessity of the revision of related broadening coefficients.

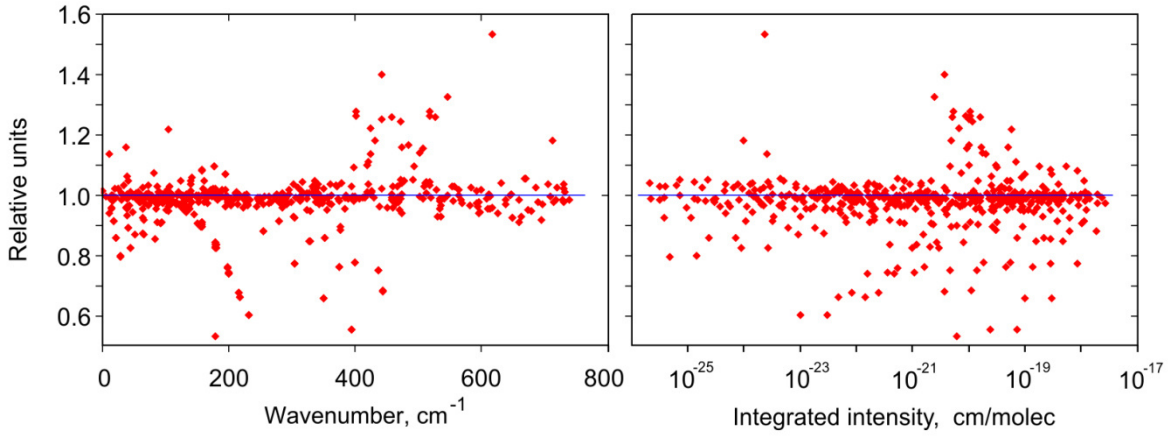

Fig. 3.18.

Plotted symbols correspond to the quantity $0.21(\gamma_{O2}/\gamma_{air}) + 0.79(\gamma_{N2}/\gamma air)$ for all the calibration lines

The results of MCRB calculations were updated in [Vispoel2020]. Supplementary materials of [Vispoel2020] provide the line list in HITRAN format including N_2-broadening coefficients. It was used for modelling of resonance spectrum for humidified nitrogen in the near-infrared range without additional extension. Oxygen-broadening coefficients of each water line were calculated using the equation $\gamma_{air} = 0.79\gamma_{N2} + 0.21\gamma_{O2}$, using γ_{air}, and γ_{N2} from HITRAN2020 [Gordon2020] and Ref. [Vispoel2020], respectively.

3.3.3. Total absorption composition for humidified N_2, O_2 and air

In case of humidified nitrogen, oxygen and air, total absorption consists of dry $\alpha_{dry\ gas}$ and water-related α_{wet} components. Let us consider $\alpha_{dry\ gas}$ composition first. As it was discussed in Chapter 1.1.2.2, for dry nitrogen, dry oxygen and dry air, stable dimers and dipole transitions of monomers are practically absent at chosen experimental conditions (O_2 magnetic dipole lines are much weaker than water monomer lines in both frequency ranges under consideration). In dry air, contributions of the lines of impurity gases (CO_2, NH_3) are negligible at the frequencies selected for measuring the continuum.

In the far-infrared range, performed dry gas recordings allows $\alpha_{dry\ gas}$ estimation. Such estimation using the same spectra as for the baseline stability check (see **Fig. 1.11** and **Sect. 1.2.1.3**) shows that $\alpha_{dry\ gas}$ is within 1.5% nearby the maximum of water rotational band at pressures considered in this work (**Table 3.1**) which is within the margin of error associated with experimental noise in the entire considered wavelength range. However, even a small CIA contribution is taken into account automatically, since reference spectra are recorded using the same dry gas at the same pressure as the wet gas spectrum.

The different contributions to the total absorption α_{total} in the near-infrared range are illustrated in **Fig. 3.19** for N_2, O_2 and air. $\alpha_{dry\ gas}$ and α_{wet} are shown in the left and right panels of **Fig. 3.19** using typical pressure ramps. In this frequency range, the total absorption of humidified oxygen is

significantly larger than for nitrogen and air, due to the contribution of the collision-induced oxygen absorption band centred near 7900 cm^{-1} [Mondelain2018]. In contrast to the far-infrared range, Rayleigh scattering makes a noticeable contribution to the total absorption in the near-infrared. It was calculated from the refractive index coefficients given in [Thalman2014]. It depends linearly on pressure and its contribution makes the total absorption dependence on pressure squared nonlinear.

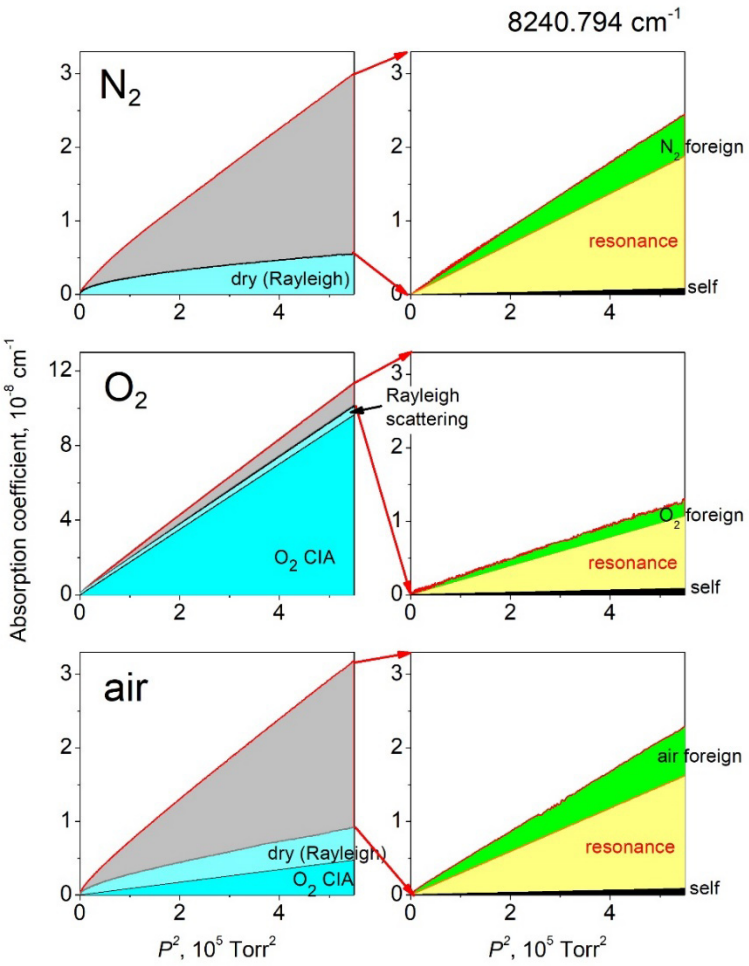

Fig. 3.19.

Left panels: Variation of the absorption coefficient *versus* the squared total pressure, *P,* for humidified (red curve) and dry (black curve) gas samples during pressure ramps up to 750 Torr at the 8240.794 cm^{-1} spectral point. The dry gas "absorption" (in cyan) includes a Rayleigh scattering contribution and a contribution of the CIA of the 1.27 μm oxygen band (for O_2 and air).

Right panels: The water-related absorption (gray area in left panel) obtained as difference of the humidified and dry absorption. It includes contributions of the water vapor self-continuum (blue area), the resonance lines (yellow area) and the foreign-continuum absorption (green area).

Dry gas absorption was recorded additionally and was used as baselines in the near-infrared similarly to the reference spectra used in the far-infrared range to take into account the dry continuum

contribution and the contribution of Rayleigh scattering. After the subtraction, the aforementioned nonlinearity introduced by Rayleigh scattering mostly disappears. The water-related absorption and all its components depend linearly on the total pressure squared because the concentration of water vapor is maintained constant and thus proportional to the total pressure.

Despite the fact that experimental conditions and positions of microwindows were chosen to maximise the measured foreign-continuum, the contribution of water monomer lines to total absorption exceeds 50% both in far- and in near-infrared range. The contribution of water self-continuum to the total absorption is relatively small (about 10% nearby the continuum maximum in the far- and less than 5% in near-infrared). For near-infrared range, the water-related absorption is shown in the right panels of **Fig. 3.19** for all three gases under consideration. Note that measured foreign-continuum absorption is very small (within 15% of total absorption for air and nitrogen and less than 1.5% for oxygen) which make such measurements and data treatment challenging and lead to high uncertainties of retrieved foreign-continuum cross-sections (see **Sect. 3.3.4.2** and **3.4**).

3.3.4. Foreign-continuum cross-sections retrieval

3.3.4.1. Far-infrared range (50-500 cm^{-1})

In each of the chosen microwindows, the continuum was calculated as the difference between the total absorption observed in the experiment and the resonance spectrum modelled using Eqs. (1.7-1.9). **Figure 3.20** shows typical examples of continuum pressure dependences for increasing and decreasing pressure dependences in upper and lower panels, correspondingly.

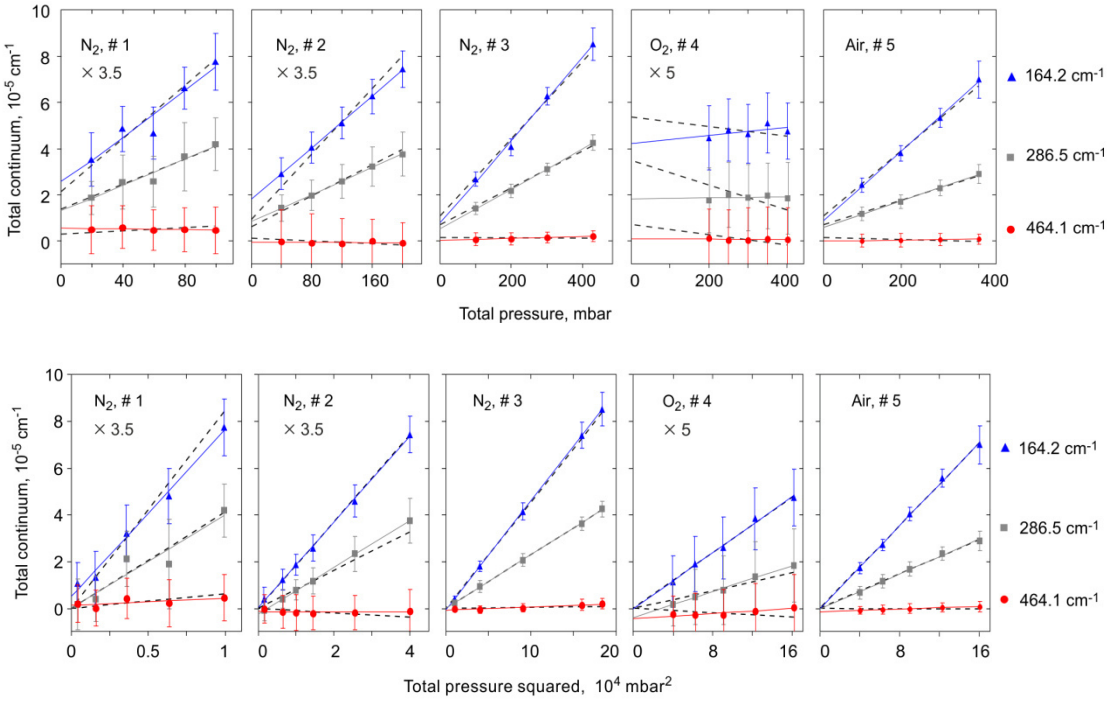

Fig. 3.20.

Total derived continuum absorption pressure dependence for in H_2O-N_2, H_2O-O_2 and H_2O-air mixtures for three typical micro-windows in the far-infrared range during increasing pressure (upper panel) and decreasing (lower panel) ramps. The absorption magnitude for Series 1-2 and 4 have been multiplied by 3.5 and 5 respectively. Error bars correspond to 1σ standard deviation of the noisy signal from its mean value within the current micro-window. Solid and dashed straight lines correspond to the best fit of linear function with and without the empirical correction term $\Delta\alpha$, to the same points (see text for details).

The independence of water and foreign-gas content during increasing pressure ramp leads to a linear dependence of the total continuum on the pressure. Since the water pressure is constant (see Table 3.4 in **Sect. 3.3.1**), the self-continuum does not change during the increasing pressure ramp and can be defined as an intercept of the pressure dependence. The self-continuum cross-sections obtained in this way agree within 3σ-uncertainty with the latest [Odintsova2020] self-continuum measurements in pure water vapour (**Fig. 3.21**). This validates the used approach and allows for using the more accurate C_S values of [Odintsova2020] for the foreign-continuum retrieval.

The foreign-continuum was calculated using following formula:

$$\alpha_{for}(\nu, P) = \alpha_{cont}(\nu, P) - C_s^{[Odintsova2020]} P_{H_2O}^2/kT = \\ = \Delta\alpha(\nu) + C_f\, P_{H_2O}/kT, \quad (3.1)$$

where $\Delta\alpha$ is an empirical constant for taking into account the discussed in **Sect.1.2.1.3**, **Fig.1.11** variations of the baseline. Its influence on data treatment is reflected by the difference between the straight solid and dashed lines in **Fig. 3.20** corresponding to fit with and without $\Delta\alpha$. Both lines are well within the uncertainty range of experimental points but the correction improves the *rms* of the fit

by a factor of 3. Under the experimental conditions chosen in this work, the correction term represents between 1% and 10 % of the total continuum absorption.

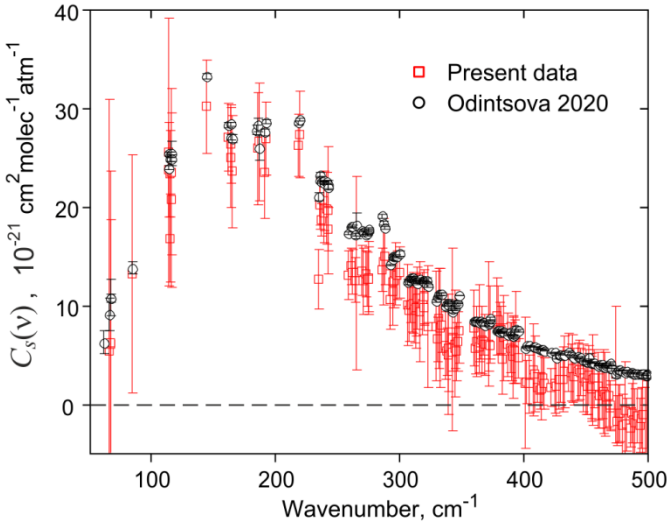

Fig. 3.21.

Water vapour self-continuum cross-section averaged over all data retrieved in this work from increasing pressure ramps (open red squares) and similar data from [Odintsova2020] (open black circles). Error bars correspond to 1σ uncertainty.

The constant value $P_{H_2O}/P_{foreign}$ (1-15% depending on experimental series) leads to linear continuum dependence on the total pressure squared dependence as follows:

$$\alpha_{cont}(\nu, P) = \Delta\alpha(\nu) + \frac{\beta(\nu)P^2}{kT}, \tag{3.2}$$

$$\beta(\nu) = C_s^{[Odintsova2020]}\left(\frac{P_{H_2O}}{P}\right)^2 + C_f\left(\frac{P_{H_2O}}{P}\right)\left(1 - \frac{P_{H_2O}}{P}\right), \tag{3.3}$$

where $\Delta\alpha$ again corresponds to the baseline variations. The foreign-continuum cross-sections C_f were calculated from β values derived from the linear dependence of the total continuum *versus* P^2 using C_s values from [Odintsova2020].

An agreement of foreign-continuum cross-sections retrieved with increasing and decreasing pressure ramps is illustrated in **Fig. 3.22**. Large measurement uncertainty in data recorded with globar as a radiation source (Series 1 from Table 3.4) is explained by smaller radiation power available from the globar source than from the synchrotron (Fig. 1.4) and in Series 2 (recorded with synchrotron but with lower total and H_2O pressure than for other synchrotron foreign-continuum measurements) by small amount of water vapour (Table 3.4), leading in both cases to smaller signal-to-noise ratio compared to other series. The presence of periodic variations at high frequencies for series 3 and 4 indicates an imperfect correction of the baseline with $\Delta\alpha$ since it takes into account the change of the baseline not for each pressure, but on average. Agreement between increasing and decreasing pressure ramps data allows its weighted averaging for further use and comparison with literature.

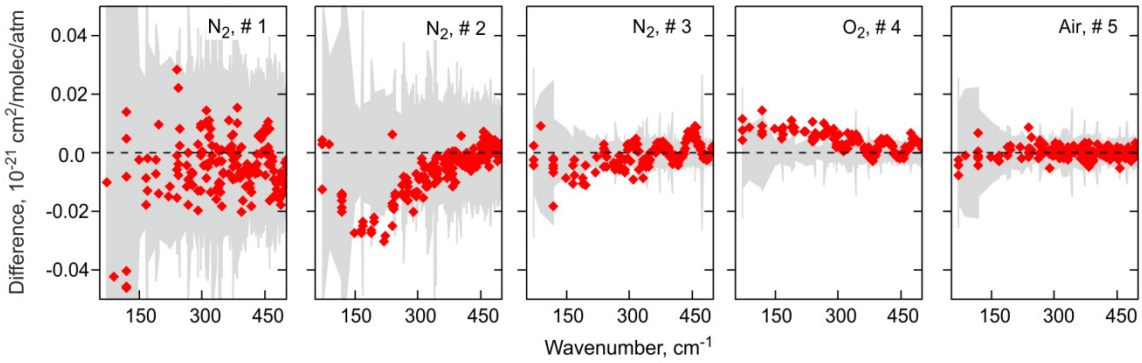

Fig. 3.22.

Differences between the retrieved C_f values corresponding to the increasing and decreasing pressure ramps. Gray areas represent $\pm 1\sigma$ combined uncertainty of two datasets centred on zero.

An agreement between H_2O-N_2 foreign continuum retrieved from different experimental series (Series 1 corresponds to globar data and Series 2 and 3 recorded with different total and H_2O pressures using synchrotron radiation, see Table 3.4) is demonstrated in **Figure 3.23**. Final derived H_2O-N_2 foreign continuum corresponds to mean weighted value from all these series.

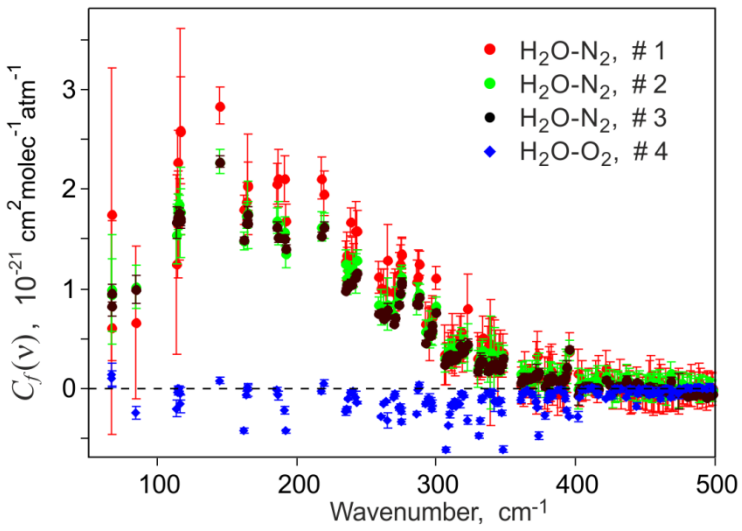

Fig. 3.23.

Cross-sections of H_2O-N_2 (Series 1 recorded with globar and Series 2-3 recorded with synchrotron with different total and H_2O pressures) and H_2O-O_2 (Series 4) foreign-continuum absorption averaged over increasing and decreasing pressure. Error bars correspond to 1σ combined uncertainty of the two datasets

H_2O-O_2 foreign continuum turned out to be too small to be determined (**Fig. 3.23**). Its upper limit is about one order of magnitude less than H_2O-N_2 foreign continuum. The coincidence between increasing and decreasing pressure ramps (**Fig. 3.22**) is several times better than the amplitude of the

fluctuations between successive micro-windows, indicating that both large spread of points and negative cross-sections are due to uncertainties of H_2O line pressure broadening parameters.

Air foreign-continuum cross-section determination results are presented in **Fig. 3.24** together with weight-averaged N_2-continuum cross sections (multiplied by 0.78 to take into account N_2 content in air) demonstrating good quantitative agreement between these two datasets. Note that the "plinth/pedestal" under resonance lines is attributed to water resonance spectrum and not to the continuum as it is accepted in MT_CKD model (by analogy with the self-continuum retrieving in the far-infrared range). For proper comparison, the contribution of the pedestal is subtracted from the MT_CKD continuum leading to appearance of sharp peaks due to wing cut off. MT_CKD-3.2 version was available at the time of the presented analysis. Current version of the model (4.1) coincides with v.3.2 for the water foreign-continuum.

Obtained foreign-continuum cross-sections are available in supplementary materials to [Koroleva2021].

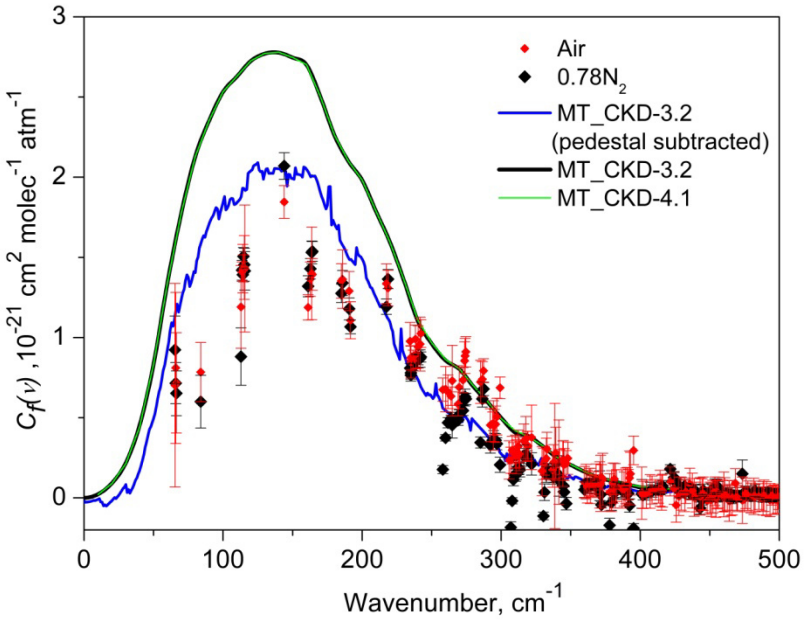

Fig. 3.24.

H_2O-air (red rhombs) and multiplied by 0.78 H_2O-N_2 (black rhombs) foreign-continuum cross-sections retrieved in this work. Error bars correspond to 1σ uncertainty. Blue solid line presents corresponding data of MT_CKD-3.2 with subtracted pedestal for comparison (see text for details). Black and green lines are for unmodified data from MT_CKD-3.2 and MT_CKD-4.1.

3.3.4.2. Near-infrared range (8100-8600 cm^{-1})

The foreign-continuum was obtained after subtraction of water monomer lines and self-continuum contributions from the water-related absorption part (**Fig. 3.19**). Despite the fact that the continuum was retrieved in microwindows under experimental conditions selected to be optimal for

these measurements, the monomer lines contribution to water-related absorption exceeds 50% in all selected microwindows. The measured foreign-continuum is very small and strongly affected by pressure uncertainties and the inaccuracies of monomer lines parameters.

The expected linear dependence of foreign-continuum on total pressure squared is illustrated in **Fig. 3.25** for all three gases under consideration. Decreasing and increasing pressure ramps data are superimposed in this figure. The foreign continuum cross-sections were obtained from a linear fit of the pressure dependences using Eq. (1.16).

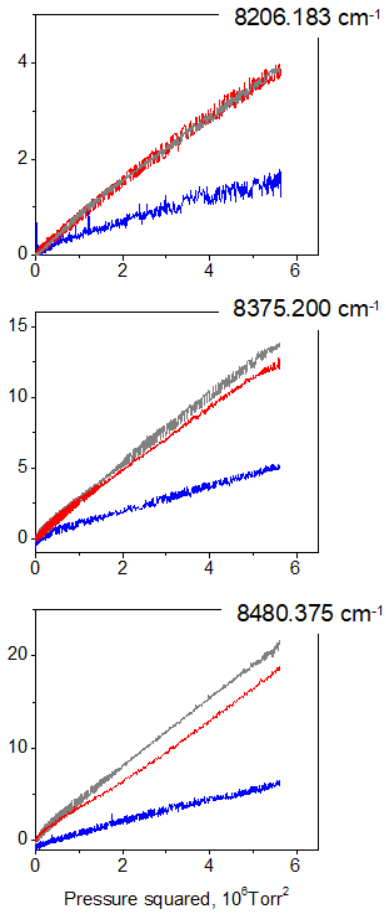

Fig. 3.25.

Variation of the absorption coefficient corresponding to the foreign gas contribution *versus* the squared total pressure, *P,* during both increasing and decreasing pressure ramps for three typical microwindows. Traces in grey, blue and red correspond to gas samples of humidified N_2, O_2 and synthetic air, respectively.

Figure 3.26 shows an overview of the retrieved foreign continuum cross-sections. The plotted error bars are the experimental uncertainties on the (corrected) value of the water partial pressure (about 3%) (see **Sect. 3.4**). It should be pointed that the above-mentioned 15 % line intensity based correction of the partial pressure of water vapour in the gas cell has a strong impact on the obtained C_f values. Without the correction, nitrogen and air foreign-continuum cross-sections values would have

been smaller by a factor 2-3 and the oxygen foreign-continuum cross-sections become too weak to be evaluated.

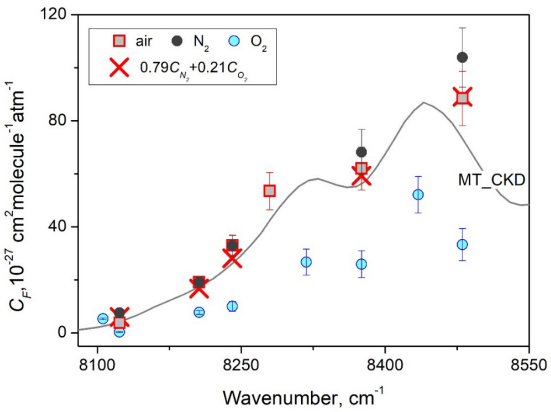

Fig. 3.26.

Overview of the near IR foreign continuum cross-sections, C_f, retrieved in this work for N_2 (black dots), O_2 (blue dots) and dry air (red squares) and comparison to the MT_CKD-4.1 model for air. The red crosses correspond to the calculated values of C_{air} obtained from $C_{air}= 0.79C_{N2}+0.21C_{O2}$. The plotted error bars correspond to signal to noise ratio and linear fit error (Eq. 1.15) and pressure uncertainty.

Obtained foreign-continuum cross-sections are presented in **Table 3.5** together with their uncertainties associated with experiments and with monomer lines parameters uncertainties (it represents Table 1 from [Koroleva2023II]).

Table 3.5. Foreign gas cross-sections of water vapor (C_F) derived at nine spectral points between 8100 and 8500 cm^{-1}.

Wavenumber, cm^{-1}	C_F 10^{-27} $cm^2molecule^{-1}atm^{-1}$			Resonance absorption %			Uncertainty due to resonance spectrum 10^{-27} $cm^2molecule^{-1}atm^{-1}$		
	N_2	O_2	air	N_2	O_2	air	N_2	O_2	air
8105.865	-	5.3(3)	-	-	49.6	-	-	2.1	-
8123.155	7.6(1.1)	0.3(2)	3.8(9)	68.6	82.6	77.0	2.3	3.8	4.4
8206.183	19(2)	7.7(8)	19.1(1.9)	63.1	67.2	61.3	4.1	6.3	7.6
8240.794	33(4)	10.1(1.9)	33.0(3.7)	69.8	77.7	67.6	8.8	14.2	16.9
8279.585	-	-	53.5(7.0)	-	-	72.4	-	-	34.3
8317.615	-	26.7(4.7)	-	-	76.1	-	-	32.3	-
8375.200	68.2(8.5)	25.9(5.1)	62.0(8.0)	71.4	78.0	71.8	14.3	33.8	32.3
8434.240	-	52.1(6.9)	-	-	68.8	-	-	40.2	-
8480.505	104(11)	33.3(6)	88.4(10.0)	66.5	74.2	67.8	12.9	37.5	42.0

Notes

Columns 2-4: C_F values for N_2, O_2 and air, respectively, with corresponding experimental uncertainty given between parenthesis. The uncertainty value is limited to the statistical fit uncertainty and water partial pressure uncertainty,

Columns 5-7: Corresponding fraction (in %) of the resonance absorption contribution to the water-related absorption,

Columns 8-10: Uncertainty related to the subtraction of the resonance absorption contribution evaluated on the basis of the errors on the HITRAN line parameters.

3.3.5. Discussion and comparison with literature

Water vapour foreign-continuum in the Earth atmosphere is mostly due to molecular collisions of water molecules with nitrogen (78.084 %), oxygen (20.95 %) and argon (0.934 %):

$$\alpha_{H_2O-air} = C_{H_2O-air}\frac{P_{H_2O}P_{air}}{kT} = \\ = C_{H_2O-N_2}\frac{P_{H_2O}P_{N_2}}{kT} + C_{H_2O-O_2}\frac{P_{H_2O}P_{O_2}}{kT} + C_{H_2O-Ar}\frac{P_{H_2O}P_{Ar}}{kT} \quad (3.4)$$

where C_{H_2O-air}, $C_{H_2O-N_2}$, $C_{H_2O-O_2}$and C_{H_2O-Ar} are corresponding foreign-continuum cross-sections.

The contribution of H_2O-Ar pairs to the atmospheric continuum absorption is expected to be negligible because of the small relative abundance of argon and because Ar collisions with water molecules are less efficient in induction of additional dipole in H_2O molecules than N_2-H_2O and O_2-H_2O collisions due to the spherically symmetric structure of Ar. This is confirmed by the fact that the H_2O-Ar continuum cross-section was measured to be several times less than the H_2O-N_2 cross-section at 239 GHz [Bauer1998]. Taking into account gases concentrations in the air, this led to a relation

$$C_{H_2O-air} = 0.78C_{H_2O-N_2} + 0.21C_{H_2O-O_2} \quad (3.5)$$

Figure 3.26 illustrates the good agreement between the measured C_{H_2O-air} values and those calculated using Eq. (3.5) with the measured $C_{H_2O-N_2}$ and $C_{H_2O-O_2}$ cross-sections in near-infrared range.

In the far-infrared, the H_2O-O_2 continuum is much weaker than H_2O-N_2 continuum (too weak to be determined). Eq. 3.5 could be simplified to

$$C_{H_2O-air} = 0.78C_{H_2O-N_2} \quad (3.6)$$

Figure 3.24 illustrates the good agreement between the measured C_{H_2O-air} and $C_{H_2O-N_2}$ connected by this relation. The deviations (more notable in the range between 250 and 400 cm^{-1}) are related to the inaccuracy of resonance lines parameters, mostly foreign gases broadening coefficients (see discussion in **Sect. 3.4.2**). The agreement between sets of measurements for different foreign-gases illustrates the self-consistency of obtained results.

In the frame of the far-wing water continuum interpretation, $C_{H_2O-N_2}$ and $C_{H_2O-O_2}$ are expected to scale according to the corresponding water line broadening coefficients. Roughly, oxygen broadening coefficients of water lines are on average 30% smaller than those by nitrogen that is in line with scaling factor of nitrogen and oxygen foreign continuum in the near-infrared range (**Fig. 3.24**). This is not the case in the far-infrared range probably because heterodimers contribution to foreign-continuum [Baranov2012II].

For comparison with literature data in the far-infrared range, the mean weighted value of $0.78C_{H_2O-N_2}$ and C_{H_2O-air} determined in this work was used. Also, all the previous measurements in nitrogen were converted to C_{H_2O-air} using Eq. (3.6). **Figure 3.27** illustrates the generally good agreement between presented far-infrared foreign-continuum cross-sections with previous

measurements in the upper [Burch1979] (350-500 cm^{-1}) and lower [Podobedov2008, Slocum2015] (22-84 cm^{-1}) wings of the band.

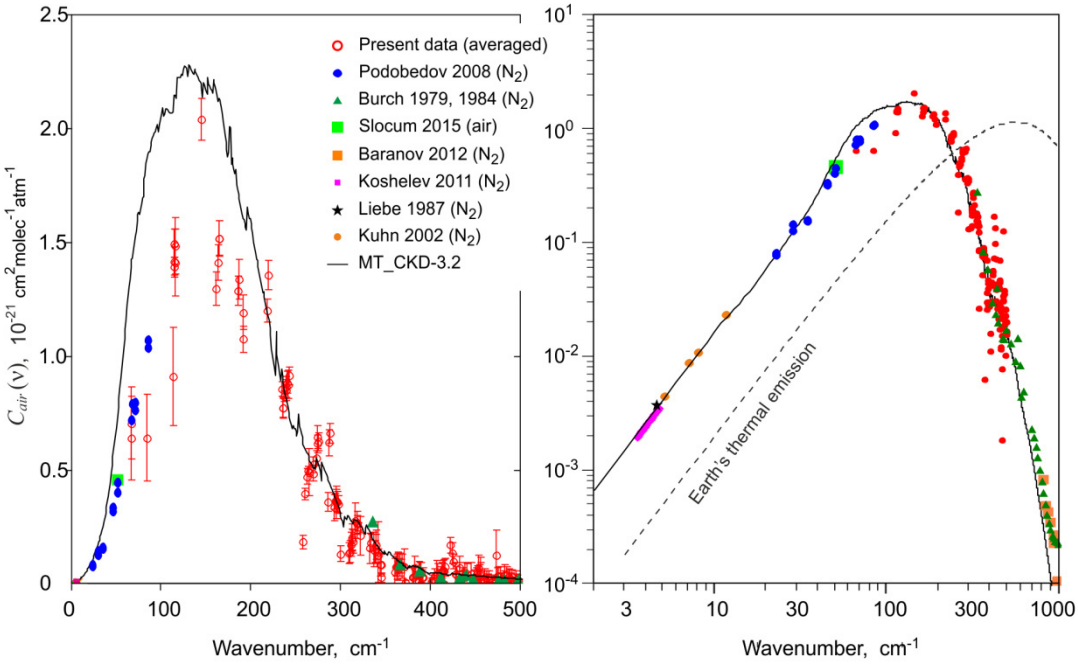

Fig. 3.27.

Comparison of the results from this work to literature laboratory data on absorption cross-sections of the H_2O-air continuum at 296 K in linear (left) and logarithmic (right) scales. The dotted curve in the right panel is the Planck's law for the Earth's mean thermal emission radiance (in arbitrary units).

The only measurements of the foreign-continuum available in the near-infrared frequency range are high-temperature CAVIAR results [Ptashnik2012]. Taking into account the fact that the temperature dependence of the foreign continuum is known to be very weak [Ptashnik2012], agreement on the order of magnitude of presented foreign-continuum measurements with 400 K CAVIAR C_{air} values is observed (**Fig. 3.28**). The large error bars of CAVIAR measurements (on the order of 100%) do not allow for a sound comparison.

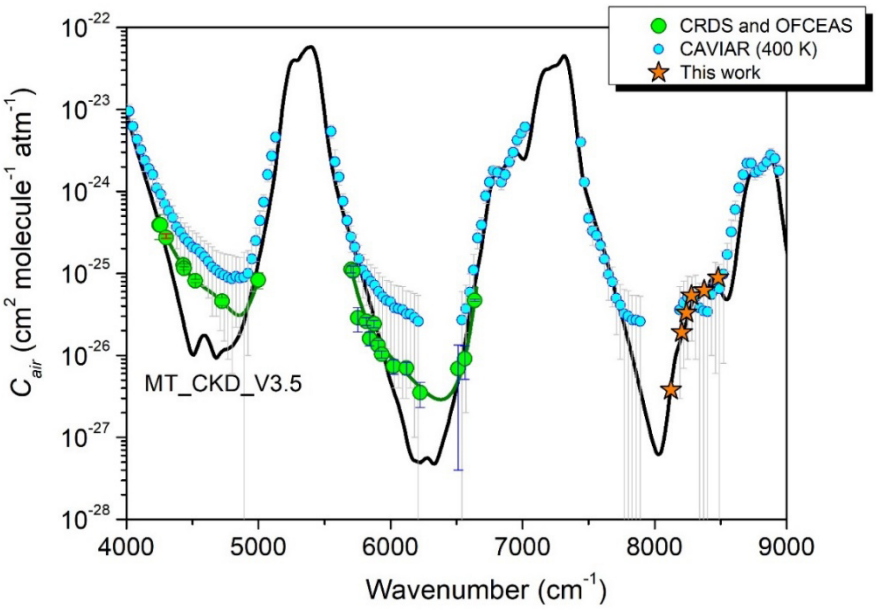

Fig. 3.28.

Overview of the water foreign continuum cross-sections, C_{air} between 4000 and 9000 cm^{-1} obtained in this work and found in the literature [Mondelain2014 ,Vasilchenko2019, Mondelain2020, Ptashnik 2012], and comparison to the MT_CKD-3.5 model. The CAVIAR experimental values [Ptashnik2012] were obtained at 400 K while the other data are for room temperature.

The comparison of experimental and calculated C_{air} values with the MT_CKD model shows an overall good agreement in both frequency ranges, although some overestimate is notable (**Fig. 3.27**) near the maximum of the water rotational band (60–200 cm^{-1}) where previous experimental data were absent. In the near-infrared range, $C_{H_2O-O_2}$ frequency dependence is consistent with the two maxima of the MT_CKD model (**Fig. 3.26**).

3.4. Continuum uncertainty analysis

Despite the significant difference between CRDS and FTS setup and the difference in the details of data processing, in both frequency ranges the accuracy of the resulting continuum cross-sections is limited by the following factors:

a. Detector noise
b. Experimental baseline stability
c. Stability of the gas sample temperature and pressure during the measurements
d. Data processing method
e. Validity of the resonance spectrum model including line shape and the accuracy of line parameters
f. Approach for far line wings modelling

The a-c points could be attributed to the "technical" side and are discussed in **Sect. 3.4.1**. Points d-f concern resonance spectrum modelling are examined in **Sect. 3.4.2**.

3.4.1. Experimental uncertainty

In microwindows of transparency, where the continuum was measured, experimental noise is noticeable on the background of small absorption, especially at low pressures. Baseline variations are not revealed under experimental conditions both in far- and in near-infrared range except for foreign-continuum measurements in far-infrared range (see **Sect. 1.2.1.3**). These variations were taken into account by correction term $\Delta\alpha$ (Eq. 3.1 and 3.2) and is believed not to influence on resulted foreign-continuum cross-sections value. The experimental noise is thus determined by the detector noise in both frequency ranges.

In the far-infrared, this is reflected in **Figs. 3.8** and **3.20** for pure water vapour and gas mixtures, where the plotted error bars correspond to the noise-equivalent absorption in the microwindows. Both for the self- and foreign-continuum cross-sections in the far-infrared, experimental noise is one of the main uncertainty sources. In contrast, pressure ramps recordings in the near-infrared range look advantageous (**Figs. 3.10, 3.19, 3.25**), where the noise level is orders of magnitude lower than the absorption level even with a small foreign-continuum magnitude (**Fig. 3.25**).

In addition, part of continuum uncertainties could be attributed to the non-linearity of continuum pressure dependences from Eq. (1.16). In the far-infrared range, the fit procedure for the foreign-continuum retrieval included additional empirical $\Delta\alpha$ term to correct instrumental baseline variations including slow drift of mean radiation power with time and imperfect reproduction of the baseline after pressure change (presumably due to the cell windows inelastic deformation). This term can introduce (in principle) systematic error in the retrieved continuum but (as discussed in detail in [Koroleva2021]), it improves the agreement with expected pressure dependences and it is smaller than statistical uncertainty of the linear function fit (**Figs. 3.8** and **3.20**). A potentially notable systematic influence on the continuum absorption cross-sections can be introduced by pressure and temperature uncertainties, especially in the case of foreign-continuum, since pressure sensors measure the total pressure of a gas mixture, and the humidity of the gas in the spectrometer cell is not certain.

The temperature was stable during all the experiments within 1 K and the uncertainty associated with temperature is believed to be negligible. Used pressure gauges have the accuracy of 0.25% of reading for both spectral ranges (see **Sect. 1.2.1.1** and **1.2.2**). Uncertainty associated with pressure is also considered to be small for self-continuum measurements and foreign-continuum measurements in the far-infrared.

During the foreign-continuum measurements in the near-infrared, water vapor partial pressure in the cell was found to be in about 15% less than the set-point (**Fig. 3.16**). In spite of the high signal-to-noise ratio of the recorded spectra and careful analysis of about twenty water line recordings, the large broadening of the line profile makes an accurate determination of the line area difficult (due to

baseline uncertainty). That led to uncertainty of applied pressure correction of about 3% although this pressure correction influence on observed continuum significantly more strongly. It was taken into account in C_f uncertainty calculation.

3.4.2. Resonance spectrum parameters uncertainty

In both frequency ranges under consideration water, vapour resonance spectrum represents the significant fraction of total observed absorption. This leads to a continuum uncertainties associated with the inaccuracy of resonant line parameters comparable or even exceeding experimental uncertainties. This is the case of the water self-continuum in the near IR, where the C_s experimental uncertainties are less than 1% while the uncertainties due to the parameters of the resonant lines are tens of percent (**Figs. 3.11** and **3.13** with C_s plotted, respectively, with total uncertainties and with experimental uncertainties only).

Resonance lines integrated absorption can be roughly estimated as the product of the line width and the absorption coefficient at the line maximum. The continuum magnitude mostly depends on the line integrated intensity, self- and air-broadening coefficients of the nearby lines. The increase of each of these parameters leads to a decrease of the continuum and *vice-versa*. The uncertainty related to line intensities and air- and self-broadening coefficients can be estimated by propagation of the error codes provided by HITRAN for the different line parameters. **Figure 3.27** presents the HITRAN2020 line parameters with a colour depending on their HITRAN error code. Note that both in far- and in near-infrared range, the accuracies are better for line intensities than for broadening coefficients. According to HITRAN error codes, intensity uncertainties are within 2-5% in the far-infrared and 5-10% in the near-infrared range for most of the lines while broadening coefficients uncertainties are between 10 and 20%. N_2-broadening coefficients uncertainties were taken from [Vispoel2019, Vispoel2020]. Note that uncertainties from [Vispoel2020] are 2-3 times smaller than for HITRAN air-broadening coefficients (which are also based on [Vispoel2020]). This fact indicates that HITRAN error codes are very conservative. Uncertainties of O_2-broadening coefficients were taken from [Gamache2019] for far-infrared range and mixed from N_2- and air-broadening coefficients uncertainties in the same way as for O_2-broadening coefficient calculation ($\gamma_{air} = 0.79\gamma_{N2} + 0.21\gamma_{O2}$) for near-infrared range.

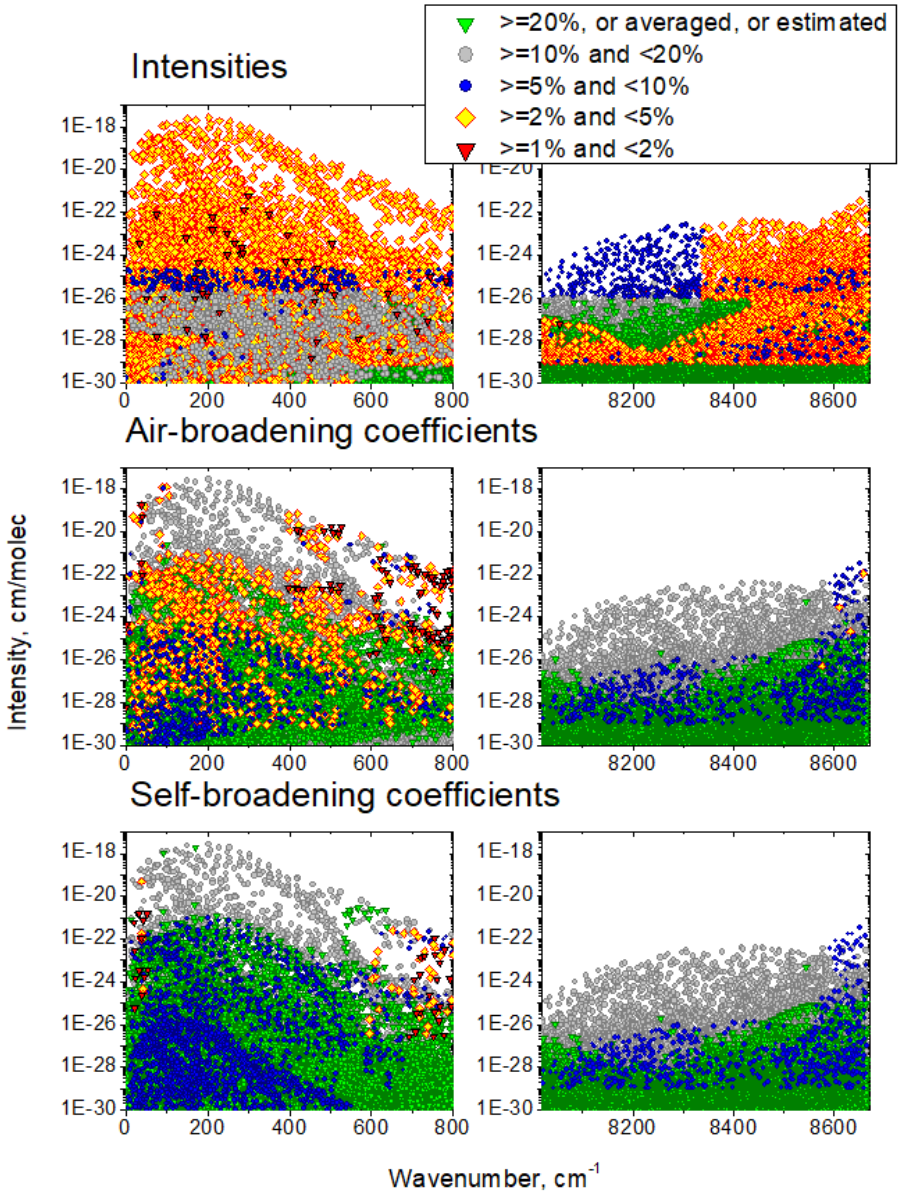

Fig. 3.27.

Overview of the HITRAN2020 [Gordon2020] line list of water vapor in the studied region with different symbols according to the error bar on the line intensities and self-broadening coefficients (left and right panels, respectively).

The uncertainties of continuum cross-sections related to the resonance lines parameters were estimated by increasing or decreasing the line parameters of all lines simultaneously within the limits of their error bars. Such procedure allows estimating the maximum expected impact on the continuum and reflect the continuum sensitivity to resonance spectrum model. The changes of the far-infrared continuum due to varying air-broadening within HITRAN uncertainties are plotted in **Fig. 3.28**. In addition to a strong impact on the C_{air} values, the variation of resonant line parameters induces a larger dispersion of the C_{air} values, the continuum frequency dependence appearing less smooth (right panel of **Fig. 3.28**). This larger dispersion illustrates the impact of the resonance absorption lines on the C_{air}

values and seems to indicate that HITRAN line parameters are reasonable and HITRAN error codes of water monomer lines are conservative.

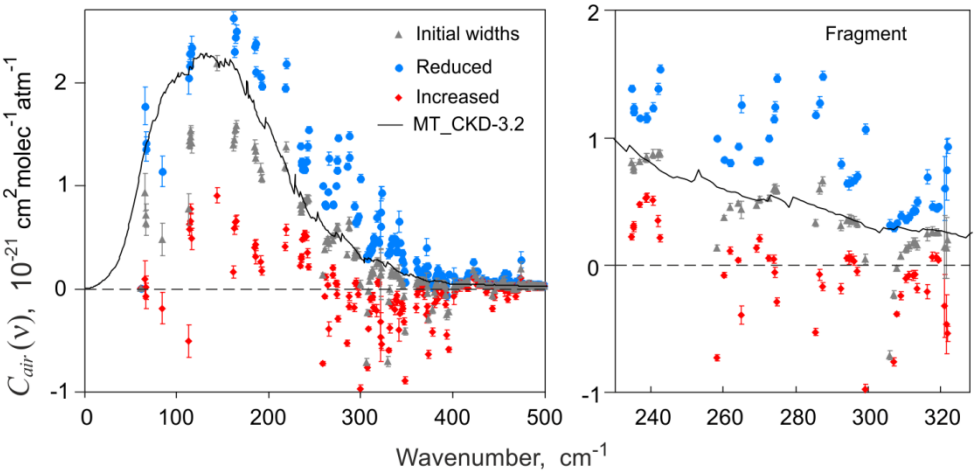

Fig. 3.28.

Continuum cross-section $C_{H20\text{-}air}$ at nominal (dark grey symbols), minimal (blue points) and maximal (red points) values of air-broadening parameter of all water lines within their HITRAN's stated uncertainty. Error bars correspond to 1σ experimental uncertainty. MT_CKD-3.2 continuum is shown by solid line for the comparison.

In the far-infrared range the described estimation gives self- and foreign continuum cross-sections uncertainties of about 20% and about 80%, respectively. In the near-infrared, it gives self-continuum cross-sections uncertainties up to 50% and more than 100% for H_2O-air foreign-continuum.

The monomer spectrum model (including line list, line shape function, its numerical parameters and line wings approach) and the set of continuum cross-sections should be self-consistent to reproduce the total absorption correctly. The absorption measured in microwindows is well reproduced by the model even with continuum coefficients obtained with excessively modified parameters of the resonance spectrum (such as blue and red points in **Fig. 3.28**). It is illustrated in **Fig. 3.29**, where the absorption in microwindows (points) are shown together with experimental H_2O-air SOLEIL spectra of foreign-continuum measurements (solid curves, series 5 from Table 3.4). The total absorption was calculated using Eqs. (1.7-1.9) for resonance spectrum modelling, C_s values from [Odintsova2020] and three different sets of C_f values presented by black, blue and red symbols in **Fig. 3.28**, each set used together with the corresponding line list. In each microwindow three corresponding symbols are merged into one in the scale of **Fig. 3.29** and can be distinguished only after significant zooming. Thus, variation of the air-pressure broadening coefficients within their stated uncertainty (about 20%) gives variation of the total absorption modelling less than 0.1% in the considered microwindows within the whole studied spectral range 50-500 cm^{-1}. Any change in the line list will result in systematic error in the total absorption calculation if the continuum coefficients are not reconsidered.

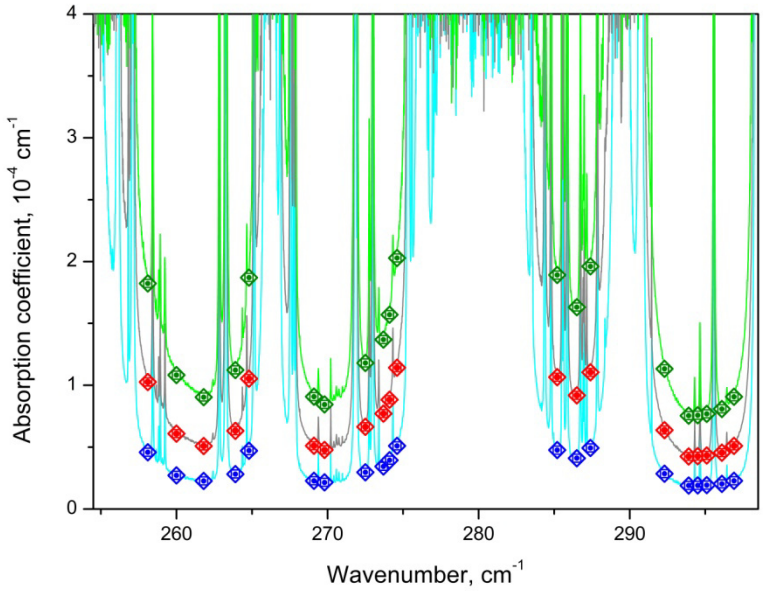

Fig. 3.29

Fragments of three typical experimental spectra (solid lines) of wet air (Series 5 from Table 3.4) and total absorption calculated in selected micro-windows on the basis of the retrieved continuum coefficients (symbols)

3.5. Insights on the origin of water vapor continuum

Water vapor self-continuum absorption (under considered conditions) consists of the absorption by molecular pairs (including stable and metastable dimer states and neglecting minor contribution of free pairs) and the absorption related to uncertain far wings of H_2O resonance lines (see **Sect. 1.1.3**). The availability of water dimer spectrum calculated by quantum-chemical methods for the far infrared range [Scribano2007] allows an attempt to separate all these components and build a continuum model on this basis. Such analysis is currently more difficult in the near-infrared range, but contribution of the dimer absorption to the observed continuum could be revealed based on comparison with the MT_CKD model and calculation of the O - H stretching vibrational overtone spectrum of the water dimer [Salmi2008] (see, for example, [Simonova2022]).

3.5.1 The self-continuum modeling in the far-infrared range

To construct a physically based continuum absorption model, it is necessary to evaluate the contributions of bimolecular absorption and resonance lines wings. Let us denote the latter absorption (which is a function of temperature) as *W(T)*. Following Eq. (1.14), for bimolecular absorption, it is necessary to model stable and metastable dimers spectra together with their equilibrium constants

(taking into account that free pairs contribution is negligible, as discussed in **Sect. 1.1.2**). The continuum absorption cross-section $C_{self}^{calc}(T)$ (in $cm^2molec^{-1}atm^{-1}$) can be thus simulated as

$$C_{self}^{calc}(\nu,T) = \alpha_{self}\, kT/P^2_{H2O} = K_{BD}BD(\nu,T)+K_{MD}MD(\nu,T)+W(\nu,T)/P \quad (3.7)$$

Ab initio calculations of stable water dimer (*BD*) spectrum in the 0–600 cm^{-1} frequency range are presented in [Scribano2007]. They are validated by [Lee2008] with more robust molecular dynamic approach and by experimental observations of the water dimer rotationally resolved spectrum in the 3.5–8.4 cm^{-1} interval [Tretyakov2013, Serov2014, Koshelev2018]. The stable dimer equilibrium constant K_{BD} was retrieved from the intensity of the rotationally resolved spectrum of the dimer at room temperature [Serov2014]. This value of the constant (0.036 atm^{-1} at room temperature) corresponds to a dissociation energy of 1144(19) cm^{-1}. The latter agrees with *ab initio* calculations [Leforestier2012] and with experimental results obtained by the velocity map imaging method [Rocher-Casterline2011II] (1108 cm^{-1} and 1105(10) cm^{-1}, respectively). However, the estimations from [Byryak2015] indicate that this K_{BD} value may be somewhat overestimated.

Metastable dimer spectrum was modelled as the superposition of two boundary cases MD_1 and MD_2 described in **Sect. 1.1.2.1** [Vigasin2010] (first and second type of metastable dimer spectrum hereafter). This approximation is expected to be good in the range of the pure rotational H_2O band because of the general similarity of these two extreme case spectra (both are bell-shaped and their intensity maxima coincide). The difference between them is noticeable nearby the dimer peak (around 10 cm^{-1}) which is absent if metastable dimer is considered as two monomers almost freely rotating near each other. Metastable dimer equilibrium constant can be calculated as $K_{MD}=b_0/RT-B(T)/RT-K_{BD}$ using empirical approximations for $B(T)$ and $b_0(T)$ from [Leforestier2014] and [Tretyakov2012], respectively.

To calculate resonance lines wings contribution $W(T)$, the empirical χ-function modifying the Lorentzian wings of resonance lines from [Serov2017] was used:

$$\chi(\nu-\nu_0) = \left(1 + A\frac{|\nu-\nu_0|}{d\nu_{wing}}\right) exp\left(-\frac{(\nu-\nu_0)^2}{d\nu_{wing}^2}\right), \quad (3.8)$$

where ν_0 is line centre frequency, A (in a.u.) and $d\nu_{\text{wing}}$ (in cm^{-1}) are the variable parameters corresponding to the line wing amplitude and the characteristic width of the wing, respectively. Model parameters A and $d\nu_{\text{wing}}$ are determined by the interaction potential and are temperature dependent because both the relative speed of molecular movement and the internal energy (characterising interaction between molecules in course of their collision) increase with temperature. Note that A may depend on the rotational state of molecule and be different for different lines, but so far there are no theoretical calculations. The model assumes that A and $d\nu_{\text{wing}}$ are the same for all lines within the band.

In relatively narrow T-intervals considered in this work, the temperature dependence of each continuum component can be approximated using a power law:

$$X(T) = X(T_0)\left(\frac{T_0}{T}\right)^{n_X}, \quad (3.9)$$

where X refers to BD, MD_1, MD_2 or W, n_X is temperature exponent.

Temperature exponent of the total continuum model is defined as:

$$n = \frac{ln\left(C_S^{calc}(T)/C_S^{calc}(T_0)\right)}{ln\left(T_0/T\right)}, \quad (3.10)$$

And similarly for the continuum components:

$$n_x = \frac{ln\left(X(T)/X(T_0)\right)}{ln\left(T_0/T\right)}. \quad (3.11)$$

As a result, the expression for the continuum absorption cross-section is converted as follows:

$$C_S^{calc}(T) = K_{BD}BD(v,T)+K_{MD}(kMD_1(v,T)+(1-k)MD_2(v,T))+W(v,T)/P, \quad (3.12)$$

where k is the relative fraction of first type metastable dimer (MD_1) to the total model of the metastable dimer spectrum ($0 \le k \le 1$).

This model function was optimised to available experimental self-continuum data in the far-infrared range (see Table 1.1). The parameters of the model function are given in Table 3.6 (which reproduce Table 2 from [Odintsova2022]).

Table 3.6. Parameters of the continuum model in the rotational band.

	K_{BD}, atm^{-1} [Serov_2014]	K_{MD} [a], atm^{-1}	w [b], cm^{-1}	k [c]	A [d]	dv_{wing} [e], cm^{-1}
296 *K*	0.036	0.016	20	1	19	15
326 *K*	0.017	0.011	30	1	14	15

Figures 3.30 and **3.31** show that the model represents experiments well. (The best agreement of the model with experimental data was achieved with k=1). Compared to SOLEIL continuum measurements, the largest deviations are observed in the 35 – 84 cm^{-1} interval, where the calculated values are intermediate between SOLEIL data and those from [Podobedov2008]. However, the deviation is within the spread of experimental points.

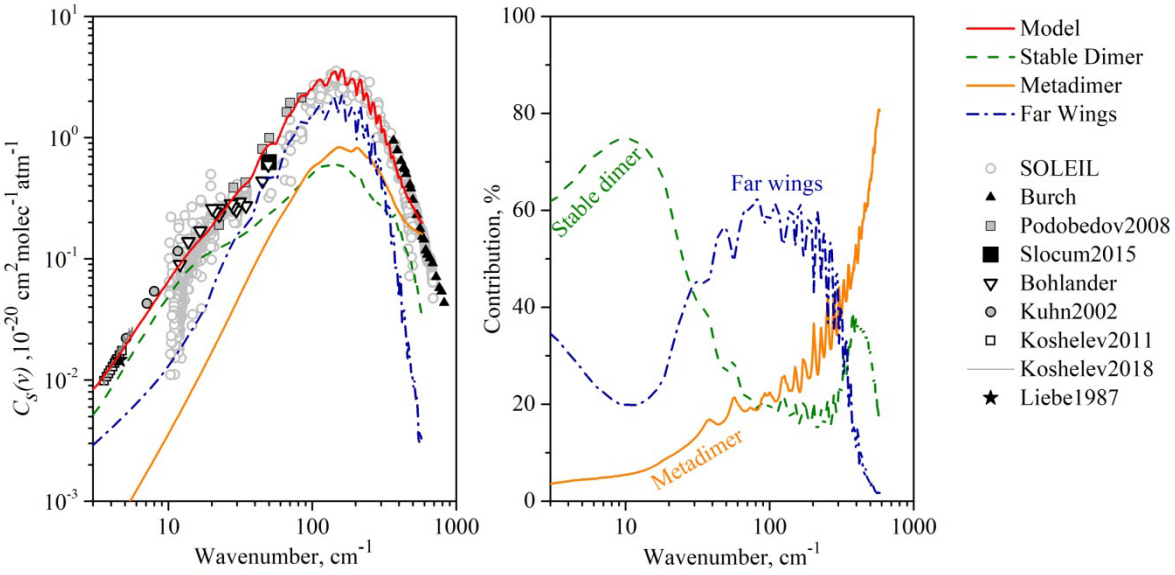

Fig. 3.30.

The self-continuum cross-section (left panel) and relative contribution of continuum components (right panel) in the superterahertz range: comparison of experimental data with model of the continuum and its components.

Experimental and calculated continuum temperature exponents are also in agreement with available (scarce) experimental data as displayed in **Fig. 3.31** within the spread of experimental points (which is quite significant). Temperature exponent frequency dependence of MT_CKD4.1 model qualitatively is very similar to the observed one, but a slight overestimation is notable.

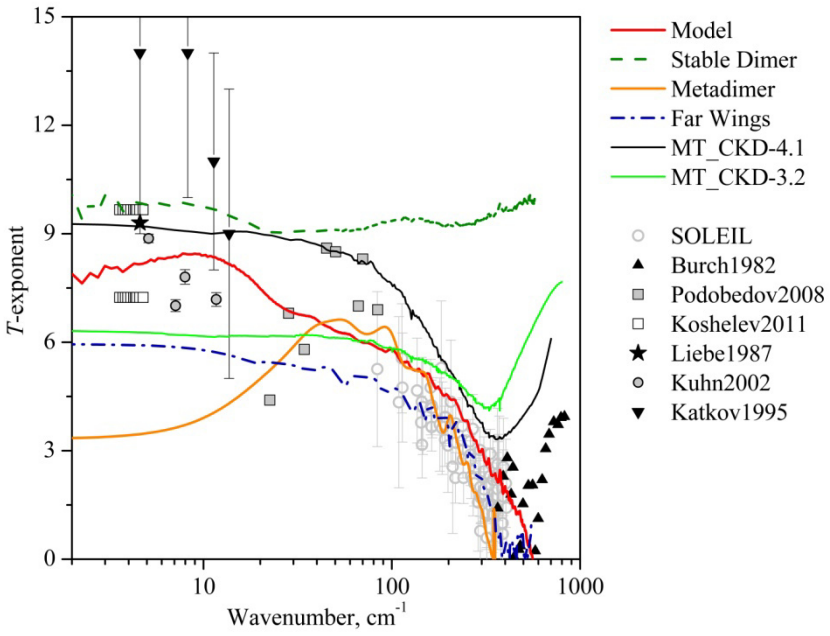

Fig. 3.31.

Self-continuum temperature exponent: experimental data and continuum models.

Thus, the model allows reproducing the experimentally observed continuum in the region of H_2O rotational band. The contribution of stable dimers is predominant (50-75%) in the mm-submm range (10–40 cm^{-1}) but decreases to about 20% in the range of the H_2O band intensity maximum (100–300 cm^{-1}) while contribution of metastable dimers increases with increasing frequency from 20 % to 40% in this range. The analysis of spectral function C_s/ν^2 (**Fig. 3.32**) reveals a characteristic sharp slope near 20 cm^{-1}. It shows that continuum frequency dependence reproduces the spectral function of the water dimer predicted by *ab initio* calculations [Scribano2007] (green dashed curve in **Fig. 3.32**). Resonance lines wings are responsible for the rest of the absorption and have the greatest influence on the continuum near H_2O rotational band maximum.

Exclusion of any of the continuum components from the model will lead to significant deviations from experiment.

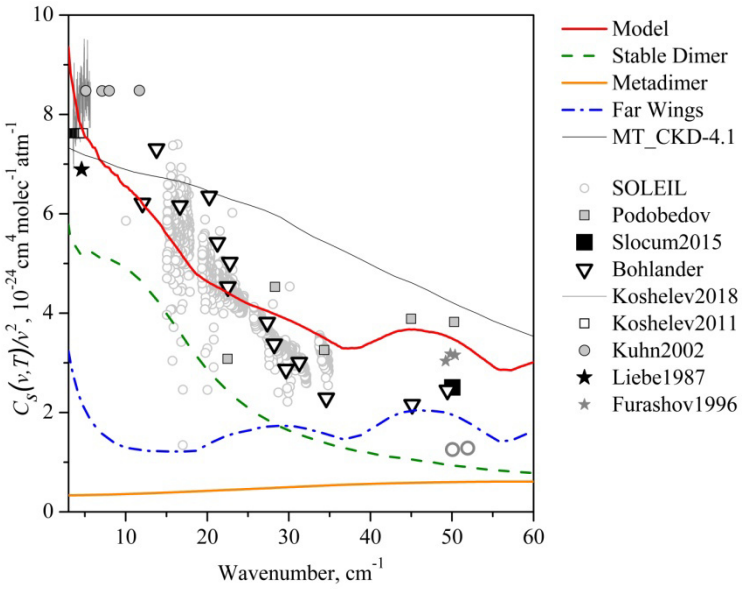

Fig. 3.32.

The self-continuum cross-section in the subterahertz range: comparison of experimental data with model of the continuum and its components.

3.5.2 Tentative detection of water dimer spectrum in the near-infrared range

The comparison of measured self-continuum cross-section with MT_CKD model (**Fig. 3.13**) reveals an additional broad structure around 8455 cm^{-1} (another weaker one seems to be present near 8300 cm^{-1}, which coincides with a small local maximum of the MT_CKD prediction).

Talking about possible explanation for the observed structure, one should not completely exclude aforementioned high uncertainty of the resonance spectrum. Note that the structure (revealed with the standard convention of the line wing cut-off at ±25 cm^{-1} adopted by the MT_CKD model) constitutes a significant (about 60%) local deviation from the model, even if it is related to resonance lines. The

continuum is also very sensitive to variation of the wing cut-off value. However, such variation weakly affects the shape of the observed spectral structure at 8455 cm^{-1}. Therefore, more likely, the structure has different origin. Let us consider if this structure can be attributed to water dimer manifestation.

In [Salmi2008], the calculation of vibrational spectrum of the water dimer is presented up to 17000 cm^{-1} by modeling the dimer as two coupled but individually vibrating monomers. A computed dipole moment surface was used to calculate band intensities. According to these calculations, one of bound water dimer bands is located near 8530 cm^{-1}. The vibrational assignment of this band upper state, labelled as $|0>f|2>b|1>$, corresponds to a vibration of the donor H_2O unit of the $(H_2O)_2$ dimer, with double excitation of the free OH bond stretching and a single excitation of the H_fOH_b bending. Although shifted by about 75 cm^{-1} from the center of the observed absorption feature (see **Fig. 3.33**), this band is the only band predicted in the region. The uncertainty of the calculation [Salmi2008] is quite close to the value of this shift (different methods presented in the article give results differing up to 50 cm^{-1}).

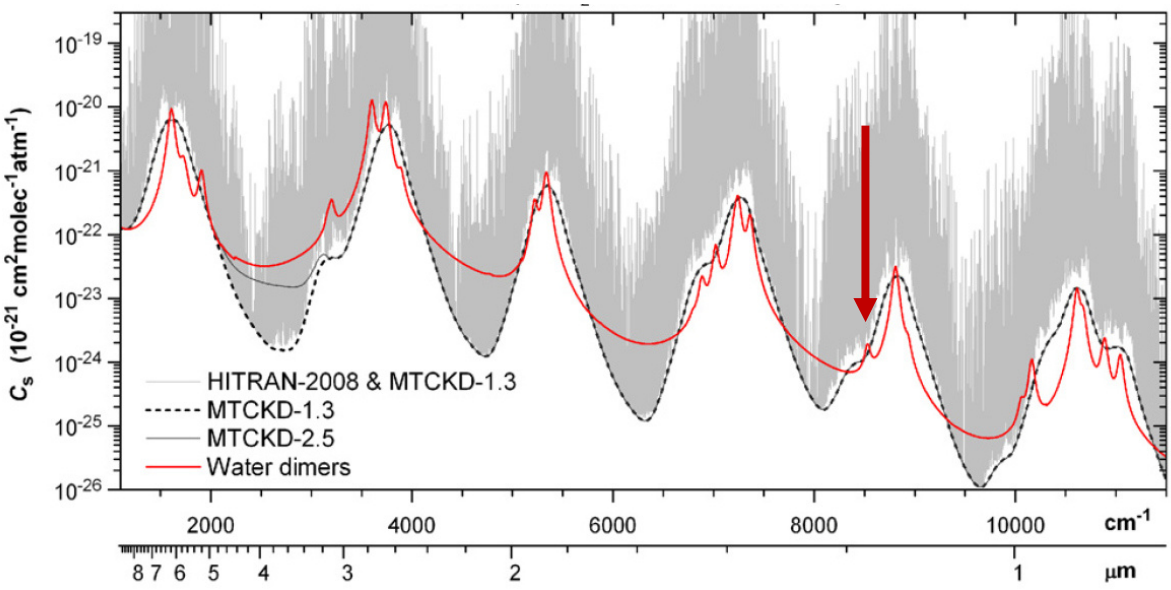

Fig. 3.33. (from [Ptashnik2011])

The general spectral resemblance between the semi-empirical continuum model MT_CKD and expected absorption by true bound water dimers. The latter is simulated in this work using theoretical data from [Kjaergaard2008] (VPT2), and partly, experimental data [Bouteiller2004, Kuyanov-Prozument2010] for water dimer band intensities and positions and K_{eq}(296 K)=0.04 atm^{-1}. The water dimer band shape is simulated using Voigt profile with FWHM=60 cm^{-1} and 1500 cm^{-1} wings cut-off. Beyond 4 m window both MTCKD versions are identical. The figure is adapted from [Ptashnik2004]

The bound water dimer cross-section integrated over a given band could be estimated as a product of band intensity S_{band} (cm/molecule) and bound dimer equilibrium constant K_{BD} (atm^{-1}):

$$\int C_s d\nu = K_{BD} S_{band}. \qquad (3.8)$$

According to recalculation from [Simonova2022], the intensity of dimer band predicted at 8530 cm^{-1} [Salmi2008] is 2.35 × 10^{-21} cm/molecule. As for K_{BD}, authors of [Simonova2022] used the average value of estimation from [Scribano2006] (recalculated with more accurate value of dissociation energy D_0= 1105 cm^{-1} instead of 1234 cm^{-1}) and [Buryak2015]. It gives K_{BD} about 0.025 atm^{-1} at a room temperature. It leads to a calculated value of 5.87 ×10^{-23} cm·$molecule^{-1}atm^{-1}$ for the integrated cross-section for this band (with the equilibrium constant at room temperature is about 0.025 atm^{-1}). The Gaussian fit of observed spectral structure after subtraction the MT_CKD prediction as a baseline (corresponding to H_2O monomer absorption) gives (4.89±1.3) × 10^{-23} $cm^2molecule^{-1}atm^{-1}$ integrated cross-section (and the band center at 8455.2±3.4 cm^{-1}). Thus, both the position of the observed band and its experimental integrated cross-section are consistent with the predicted values, which allows suggesting that this particular water dimer band might have been revealed from our CRDS spectra.

Conclusion

The water vapour self- and foreign-continua are newly measured in the high energy edge of the far- and near-infrared frequency ranges (15-500 cm^{-1} and 8100-8620 cm^{-1}) by using Fourier transform spectrometer with synchrotron as a light source in the far-infrared and highly stable and sensitive cavity ring-down spectrometer in the near-infrared. Measurements are performed at room temperature.

Expected pressure dependences of self- and foreign-continuum are observed and used to retrieve continuum cross-sections in selected microwindows. Presented data agree with previous experimental continuum studies and allow validating the MT_CKD model. In the far-infrared range, observed self continuum were used for adjustment the model which resulted in about 30% difference between the updated (4.1) and previous (3.2) versions nearby continuum maximum.

The most important contributors to the continuum uncertainty are analysed. It is demonstrated that resonance line shape parameter uncertainties strongly affect the value of the continuum. The impact of pressure broadening parameters is dominating. The interconnection between continuum cross-sections and line list used for its retrieval has been highlighted. It is shown that inaccuracies of resonance spectrum parameters and the associated continuum uncertainties do not notably affect the accuracy of determining the *total* absorption in microwindows when using the line list and related continuum data in pair.

In the far-infrared range, obtained data allowed evaluating of relative contributions of continuum components (namely, stable and metastable dimers and resonance lines wings) on the basis of available *ab initio* calculations of $(H_2O)_2$ spectrum and suggesting physically based model of atmospheric continuum. The development of the continuum model in the far-infrared range as well as natural water self-continuum cross-sections retrieval is made by T. Odintsova.

In the near-infrared frequency range, an additional broad absorption feature is observed near 8455 cm^{-1}. The band can be interpreted as a possible evidence of a band of the bound dimers, $(H_2O)_2$.

CONCLUSION

Present work contributed to the knowledge on water vapor absorption in two frequency ranges important for atmospheric and astrophysical applications such as greenhouse gas monitoring, radiation balance calculation, study of atmospheres of Solar system planets. Both components of the water vapour absorption (monomer lines and continuum) were studied on the basis of experimental data recorded using two different experimental methods (FTS and CRDS) in two frequency ranges important for practical applications.

Spectra simulation was carried out prior to each experimental series for choosing optimal thermodynamic conditions for the resonance spectrum or continuum characteristics determination. In the case of a FTS, the recording resolution was selected to minimize the influence of the apparatus function. Several test experiments were performed. In particular, in the case of FTS, baseline stability was analysed. For CRDS, excellent recordings repeatability was achieved with increasing and decreasing pressure in the cell. Spectroscopic checks of gases composition and purity and pressure stability were carried out.

High-resolution spectra recordings were obtained at several water vapor pressures, as well as pressure ramp recordings at a fixed frequency in the near-infrared range.

In both frequency ranges, the water line positions and intensities were determined based on the fitting of the line profile to the experimentally recorded spectral lines. Identification of spectral lines was carried out. The measured line positions allowed to clarify (and in some cases to determine for the first time) the values of the energy levels of the water molecule. The result of this part of the work are line lists containing information about line parameters (line positions and intensities) supplemented by their uncertainties, quantum numbers identifying the corresponding transition, and energy values of the lower levels of the transition. The line lists contain lines that differ in intensity by 7 and 4 orders of magnitude in the far- and near-infrared range, respectively, thanks to the wide pressure range and the high sensitivity of the spectrometers. In the near-infrared range, it was possible to retrieve the parameters for the lines with intensities 2 orders of magnitude less than during previous measurements in the same frequency range.

A good agreement of the obtained line parameters with previous theoretical and experimental work was demonstrated. Despite the fact that the water monomer spectrum is considered to be well known, recorded spectra analysis revealed a large number of inaccuracies in the identification of H_2O lines, their positions and intensities in widely used spectroscopic databases such as HITRAN.

For continuum retrieval, frequencies in microwindows of transparency between water lines were selected in order to maximise continuum contribution to total absorption and (in the case of the far-infrared range) minimise the apparatus function influence to measured values. The expected continuum pressure dependences were demonstrated in both frequency ranges. Self- and foreign-continuum absorption cross-sections were retrieved in two frequency ranges important for spectroscopic applications where previous measurements were absent. In the far-infrared range,

measurements of the continuum in a sample with an increased (94%) $H_2{}^{18}O$ content were carried out in addition to continuum measurements for water vapor with a natural isotopic abundance. The coincidence of results for two water vapor isotopologues with similar properties confirms the reliability of the obtained data. The consistency of the foreign-continuum retrieving results for humidified nitrogen, oxygen and air is demonstrated for both frequency ranges.

A good agreement of the obtained results with the previous continuum measurements is demonstrated. In the far-infrared range, presented results were confirmed by subsequent measurements at higher water vapor pressures. It is shown that the MT_CKD continuum model widely used for atmospheric applications overestimates the continuum in the far-infrared range by about 30% near its maximum. The obtained data were used to refine the model (they are taken into account in the MT_CKD-4.1 version) [Mlawer2023]. Continuum measurements in the near-infrared range generally validates the MT_CKD-3.5 model. In both frequency ranges, present results fill the gaps where previous experimental data were absent (**Fig. C1**)

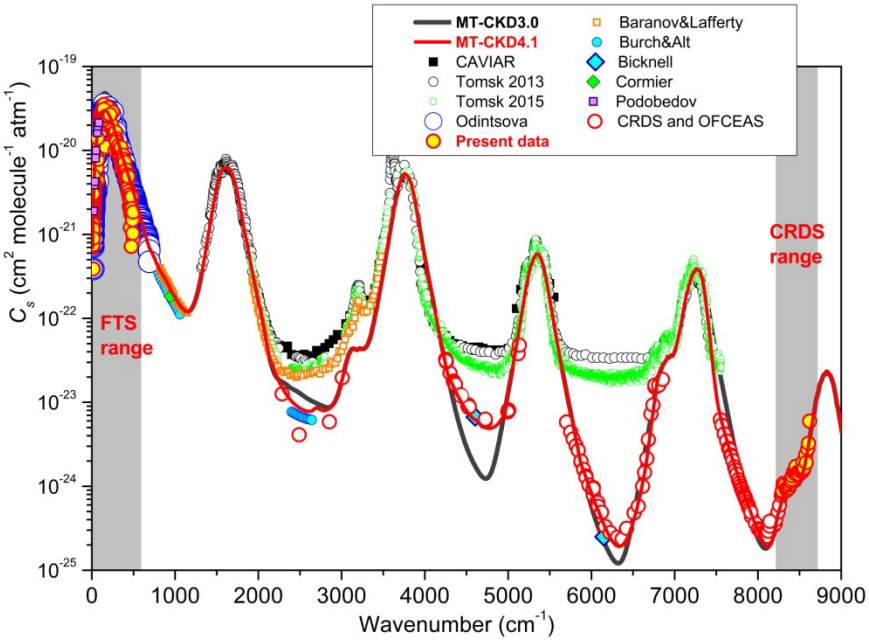

Fig. C1.

Water continuum data overview.

(See Note to Fig. 4 for comments on the CAVIAR and Tomsk data in windows)

The contributions of various uncertainty of the measured continuum were analysed. It is shown that H_2O line parameters uncertainty is one of the main error sources. It exceeds the uncertainties associated with the experimental technique and the method of data analysis. The non-smoothness of the measured continuum observed in the far-infrared range indicates insufficient subtraction of the water monomer lines, which is confirmed by the analysis of recordings at various pressures. Results of this work indicate that uncertainties of the HITRAN parameters used for the data analysis are overestimated. For a more accurate retrieving of the continuum spectrum, a significant increase in the accuracy of collision broadening coefficients calculations is necessary.

The connection between continuum absorption and the resonance spectrum model (includes water line parameters, line profile and line wings approach) used to determine continuum is demonstrated. It is shown that using of self-consistent resonance spectrum model and continuum data minimizes the influence of their uncertainties on the resulted of total absorption calculation in the microwindows of transparency (within the thermodynamic conditions for which the continuum data were obtained).

The results of presented work demonstrate that the relationship between the resonance spectrum and continuum also impose a restriction on their study separately from each other. The inaccuracy of water line parameters and the choice of water line wings model affects the magnitude of the continuum, and extracting the water lines contribution of the continuum is impossible without correct models of its other components. The joint study of resonance absorption and continuum opens the way to the construction of a physically based total absorption model. The data on the self-continuum obtained in the frame of this work in the far infrared range allowed to demonstrate the possibility of constructing a continuum model taking into account all the mechanisms of its formation (bimolecular absorption and absorption of water line wings) based on the quantum chemical calculation of the dimer spectrum [Scribano2007].

The continuum analysis in the near-infrared range revealed the presence of a peak near 8455 cm^{-1}, which is absent in the MT_CKD calculation. It can be preliminarily identified as the vibrational-rotational absorption band of the water dimer based on previous theoretical calculations [Salmi2008]. Earlier, similar peaks in the continuum spectrum were detected near the frequencies 1600, 3610 and 3750 cm^{-1} and were identified as dimeric [Ptashnik2011]. The detection of the peak at 8455 cm^{-1} presented in this work confirms that dimer features are manifested in the entire range of the vibrational-rotational spectrum of water vapor.

Water line parameters study will continue in both frequency ranges by analysing recordings obtained with FTS at SOLEIL and with CRDS made with different concentrations of water vapor isotopologues. It will allow to clarify the positions and intensities of weak lines or doublets and unresolved groups of lines. In addition, line broadening measurements are possible. As for the continuum, measuring its temperature dependences can provide the necessary data for a deeper understanding of continuum nature, as it was demonstrated in this work by the example of spectra in the far infrared.

In general, the main result of the work is new data on the spectrum of water vapor in both studied frequency ranges, which are in demand for fundamental spectroscopy and its applications and already was applied to refine model widely used for atmospheric applications [Mlawer2023].

In conclusion, the personal contribution of the author is formulated to each paper contributed to this thesis.

Table C1. Author personal contribution

			Paper	Contribution
Water lines	Far-infrared		[Toureille2022]	• determining the optimal experimental conditions • spectra recording • results analysis and comparison with literature data •
	Near-infrared		[Koroleva2023]	• fit of recorded CRDS spectrum • line assignment • comparison with literature data
Continuum	Far-infrared	Self	[Odintsova2019]	• optimal experimental condition selection • self-continuum cross-section determination using high-resolution spectra and low-resolution spectra for ^{18}O-enriched water in the frequency range 50-500 cm^{-1} • continuum uncertainty analysis • results analysis and comparison with literature
		Foreign	[Koroleva2021]	• optimal experimental condition selection • foreign-continuum cross-section determination • continuum uncertainty analysis • results analysis and comparison with literature
		Review	[Odintsova2022] [Galanina2022]	• data analysis and validation
	Near-infrared	Self	[Koroleva2022]	• optimal experimental condition selection • experimental data recording • foreign-continuum cross-section determination • continuum uncertainty analysis results analysis and comparison with literature
		Foreign	[Koroleva2023]	• optimal experimental condition selection • experimental data recording • foreign-continuum cross-section determination • continuum uncertainty analysis • results analysis and comparison with literature

REFERENCES

A

[Aldener2005] Aldener M, Brown SS, Stark H, Daniel JS, et al. Near-IR absorption of water vapor: pressure dependence of line strengths and an upper limit for continuum absorption. J Mol Spectrosc 2005;232:223. https://doi.org/10.1016/j.jms.2005.04.011.

B

[Baranov2008] Baranov YuI, Lafferty WJ, Ma Q, Tipping RH. Water-vapor continuum absorption in the 800–1250 cm^{-1} spectral region at temperatures from 311 to 363 K. J Quant Spectrosc Radiat Transfer 2008;109:2291—2302. https://doi.org/10.1016/j.jqsrt.2008.03.004.

[Baranov2011] Baranov YuI, Lafferty WJ. The water-vapor continuum and selective absorption in the 3–5 μm spectral region at temperatures from 311 to 363 K. J Quant Spectros. Radiat Transfer 2011;112:304–1313. doi:10.1016/j.jqsrt.2011.01.024.

[Baranov2011II] Baranov YuI. The continuum absorption in H_2O+N_2 mixtures in the 2000–3250 cm^{-1} spectral region at temperatures from 326 to 363 K. J Quant Spectrosc Radiat Transfer 2011;112:2281–6. doi:10.1016/j.jqsrt.2011.06.005.

[Baranov2012] Baranov Yu I, Lafferty WJ. The water vapour self- and water–nitrogen continuum absorption in the 1000 and 2500 cm^{-1} atmospheric windows. Philos Trans R Soc A 2012;370:2578–89. https://doi.org/10.1098/rsta.2011.0234.

[Baranov2012II] Baranov Yu I, Buryak IA, Lokshtanov SE, Lukyanchenko VA, Vigasin AA. H_2O-N_2 collision-induced absorption band intensity in the region of the N2 fundamental: ab initio investigation of its temperature dependence and comparison with laboratory data. Phil Trans R Soc A 2012;370:2691–709. doi:10.1098/rsta.2011.0189.

[Barber2006] Barber RJ, Tennyson J, Harris GJ, Tolchenov RN. A high-accuracy computed water line list. Mon Not R Astron Soc 2006;368:1087-94. https://doi.org/10.1111/j.1365-2966.2006.10184.x.

[Bauer1998] Bauer A, Godon M, Carlier J, Gamache RR. Continuum in the windows of the water vapour spectrum. Absorption of H2O-Ar at 239 GHz and line width calculations. J Quant Spectrosc Radiat Transf 1998;59(3-5):273–85. https://doi.org/10.1016/S0022-4073(97)00111-8.

[Bertaux2020]Bertaux J-L, Hauchecorne A, Lefèvre F, Bréon F-M, Blanot L, Jouglet D, Lafrique P, and Akaev P: The use of the 1.27 μm O2 absorption band for greenhouse gas monitoring from space and application to MicroCarb. Atmos Meas Tech 2020;13:3329–3374. https://doi.org/10.5194/amt-13-3329-2020, 2020. https://doi.org/10.5194/amt-13-3329-2020.

[Bicknell2006] Bicknell WE, Cecca SD, Griffin MK. Search for low-absorption regimes in the 1.6 and 2.1 lm atmospheric windows. J Direct Energy 2006;2:151–161.

[Birk2020] Birk M, Wagner G, Loos J, Shine KP. 3 μm Water vapor self- and foreign- continuum: new method for determination and new insights into the self- continuum. J Quant Spectrosc Radiat Transf 2020;253:107134. doi:10.1016/j.jqsrt.2020.107134.

[Bignell1970] Bignell K.J. Water-vapour infra-red continuum. Quart. J. Roy. Meteorol. Soc. 1970;96:390, http://dx.doi.org/10.1002/qj.49709640904.

[Boissoles2003] Boissoles J, Boulet C, Tipping; RH, Brown A, Ma Q. Theoretical calculation of the translation-rotation collision-induced absorption in N_2–N_2, O_2–O_2, and N_2–O_2 pairs. J Quant Spectrosc Radiat Transfer 2003;82:505–16. doi:10.1016/S0022-4073(03)00174-2.

[Bordet2021] Bordet B, Kassi S, Campargue A. Line parameters of the 4-0 band of carbon monoxide by high sensitivity cavity ring-down spectroscopy near 1.2μm. J Quant Spectrosc Radiat Transf 2021;260:107453. doi:10.1016/j.jqsrt.2020.107453.

[Bouteiller2004] Bouteiller Y, Perchard JP. The vibrational spectrum of $(H_2O)_2$:comparison between anharmonic ab initio calculations and neon matrix infrared data between 9000 and 90 cm^{-1}. Chem Phys 2004;305:1–12. https://doi.org/10.1016/j.chemphys.2004.06.028.

[Bubukina2011] Bubukina II, Zobov NF, Polyansky OL, Shirin SV, Yurchenko SN. Optimized semiempirical potential energy surface for $H_2{}^{16}O$ up to 26000 cm^{-1}. Opt Spectrosc2011;110:160-6. https://doi.org/10.1134/S0030400X11020032.

[Burch1979] Burch DE, Gryvnak DA. Method of calculating H2O transmitting between 333 and 633 cm^{-1}; 1979. Report No AFGL-TR-79-0054.

[Burch1981] Burch DE. Continuum absorption by atmospheric H2O, Proc. SPIE. 277 (1981) 28–39

[Burch1982] Burch DE. 1982 Continuum absorption by H_2O. Report No AFGL-TR-81-03001982

[Burch1984] Burch DE, Alt RL. Continuum absorption by H_2O in the 700–1200 cm^{-1} and 2400–2800 cm^{-1} windows, MA, USA: Hanscom Air Force Base; 1984. US Air Force Geophysics Laboratory report AFGL-TR-84–0128.

[Burch1985] Burch DE, Alt RL. Continuum absorption by H2O in the 700 –1200 cm^{-1} and 2400 – 2800 cm^{-1} windows, MA: Air Force Geophys Laboratory, Hanscom AFB; 1984. Report AFGL-TR-84-0128.

[Buryak2015] Buryak I., Vigasin A. A. Classical calculation of the equilibrium constants for true bound dimers using complete potential energy surface. J Chem Phys 2015;143:234304. https://doi.org/10.1063/1.4938050.

[Bykov2001] Bykov A, Naumenko O, Sinitsa L, Voronin B, Flaud J-M, Camy-Peyret C, Lanquetin R. High-order resonances in the water molecule. J Mol Spectrosc 2001;205:1-8. https://doi.org/10.1006/jmsp.2000.8231.

C

[Campargue2015] Campargue A, Mikhailenko SN, Lohan BG, Karlovets EV, Mondelain D, Kassi S. The absorption spectrum of water vapor in the 1.25 μm atmospheric window (7911 – 8337 cm^{-1}). J Quant Spectrosc Radiat Transf 2015;157:135-52. https://doi.org/10.1016/j.jqsrt.2015.02.011.

[Campargue2016] Campargue A, Kassi S, Mondelain D, Vasilchenko S, Romanini D. Accurate laboratory determination of the near infrared water vapor self-continuum: a test of the MT_CKD model. J Geophys Res Atmos 2016;121 13,180–13,203. doi:10.1002/2016JD025531.

[Campargue2020] Campargue A, Kassi S, Yachmenev A, Kyuberis AA, Küpper J, Yurchenko SN. Observation of electric-quadrupole infrared transitions in water vapor. Phys Rev Res 2020;2:023091. https://doi.org/10.1103/PhysRevResearch.2.023091.

[Cazzolli2009] Cazzolli G, Puzzarini C, Buffa G, Tarrini O. Pressure-broadening of water lines in the THz frequency region: improvements and confirmations for spectroscopic databases. Part II. J Quant Spectrosc Radiat Transf 2009;110:609–18. doi:10.1016/j.jqsrt.2008.12.001.

[Chen2000] Chen P, Pearson JC, Pickett HM, Matsuura S, Blake GA. Submillimeter-wave measurements and analysis of the ground and v_2=1 states of water. Astrophys J Suppl Series 2000;128:371–85. doi:10.1086/313377.

[Chistikov2019] Chistikov DN, Finenko AA, Lokshtanov SE, Petrov SV, and Vigasin AA. Simulation of collision-induced absorption spectra based on classical trajectories and *ab initio* potential and induced dipole surfaces. I. Case study of N_2–N_2 rototranslational band J Chem Phys 2019;151:194106. https://doi.org/10.1063/1.5125756.

[Chistikov2021] Chistikov DN, Finenko AA, Kalugina YN, Lokshtanov SE, Petrov SV, Vigasin AA, Simulation of collision-induced absorption spectra based on classical trajectories and ab initio potential and induced dipole surfaces. II. Case study of CO_2–Ar rototranslational band. J Chem Phys 2021;155:064301. https://doi.org/10.1063/5.0060779.

[Clough1980] Clough SA, Kneizys FX, Davies R, Gamache R, Tipping R. Theoretical lineshape for H*2*O vapor; application to the continuum, in: A. Deepak, T.D. Wilkerson, L. H. Ruhnke (Eds.), Atmospheric water vapor, Academic Press, New York, 1980, p. 25.

[Clough1989] Clough SA, Kneizys FX, Davies R. Line shape and water vapor continuum Atmospheric Research 1989;23:229-241.

[Coheur2005] Coheur P-F, Bernath PF, Carleer M, Colin R, Polyansky OL, Zobov NF, Shirin SV, Barber RJ, Tennyson JA 3000 K laboratory emission spectrum of water. J Chem Phys 2005;122:074307. https://doi.org/10.1063/1.1847571.

[Conway2020] Conway EK, Gordon IE, Kyuberis AA, Polyansky OL, Tennyson J, Zobov NF. Calculated line lists for $H_2{}^{16}O$ and $H_2{}^{18}O$ with extensive comparisons to theoretical and experimental sources including the HITRAN2016 database. J Quant Spectrosc Radiat Transf 2020;241:106711. https://doi.org/10.1016/j.jqsrt.2019.106711.

[Cormier2002] Cormier JG, Ciurylo R, and Drummond JR. Cavity ringdown spectroscopy measurements of the infrared water vapor continuum. J Chem Phys 2002;116:1030–1034. doi:10.1063/1.1425825.

[Cormier2005] Cormier JG, Hodges JT, Drummond JR. Infrared water vapor continuum absorption at atmospheric temperatures. J Chem Phys 2005;122:114309. doi:10.1063/1.1862623.

[Coudert2004] Coudert LH, Pirali O, Vervloet M, Lanquetin R, Camy-Peyret C. The eight first vibrational states of the water molecule: measurements and analysis. J Mol Spectrosc 2004;228:471–98. doi:10.1016/j.jqsrt.2012.02.023

[Coudert2014] Coudert LH, Martin-Drumel M-A, Pirali O. Analysis of the high-resolution water spectrum up to the second triad. J Mol Spectrosc 2014;303:36–41. doi:10.1016/j.jms.2014.07.003.

D

[De Natale1997] De Natale P, Lorini L, Inguscio M, Nolt IG, Park JH, Di Lonardo G, et al. Accurate frequency measurements for H_2O and $^{16}O_3$ in the 119 cm^{-1} OH atmospheric window. Appl Opt 1997;36:8526–32. doi:10.1364/AO.36.008526.

[Drouin2011] Drouin BJ, Yu SS, Pearson JC, Gupta H. Terahertz spectroscopy for space applications: 2.5 –2.7 THz spectra of HD, H_2O and NH_3. J Mol Structure 2011;1006:2–12. doi:10.1016/j.molstruc.2011.05.062.

E

[El-Kader2016] El-Kader MSA. Theoretical Calculation of the Rototranslational Collision-Induced Absorption (CIA) Spectra in O_2–O_2 Pairs. Z Phys Chem 2016; 230(8):1099-1109. doi:10.1515/zpch-2015-0674.

F

[Firsov2023] Firsov KM, Chesnokova TYu, Razmolov AA. Impact of Water Vapor Continuum Absorption on CO_2 Radiative Forcing in the Atmosphere in the Lower Volga Region. Atmospheric and Oceanic Optics 2023;36(2):162–168. https://doi.org/10.1134/S1024856023030053.

[Flaud1979] Flaud J-M, Camy-Peyret C, Narahari Rao K, Chen D-W, Hoh Y-S, Maillard J-P. Spectrum of water vapor between 8050 and 9370 cm^{-1}. J Mol Spectrosc 1979;75:339-62. https://doi.org/10.1016/0022-2852(79)90081-X.

[Fleurbaey2022] Fleurbaey H, Grilli R, Mondelain D, Campargue A. Measurements of the water vapor continuum absorption by OFCEAS at 3.50 μm and 2.32 μm. J Quant Spectrosc Radiat Transf 2022;278:108004. doi.org/10.1016/j.jqsrt.2021.108004.

[Fulghum1991] Fulghum SF, Tilleman MM. Interferometric calorimeter for the measurement of water vapour absorption. J Opt Soc Am B 1991;8:2401. https://doi.org/10.1364/JOSAB.8.002401.

[Furashov1996] Furashov NI, Sverdlov BA, Chernyaev SN. Absorption of electromagnetic radiation by pure water vapor at frequencies near 1.5 THz. Radiophysics and Quantum electronics 1996;39(9):754–759. https://doi.org/10.1007/BF02120857.

[Furtenbacher2020] Furtenbacher T, Tóbiás R, Tennyson J, Polyansky OL, Császár AG. W2020: A Database of Validated Rovibrational Experimental Transitions and Empirical Energy Levels of $H_2{}^{16}O$. J Phys Chem Ref Data 2020;49:033101. https://doi.org/10.1063/5.0008253.

[Furtenbacher2020II] Furtenbacher T, Tóbiás R, Tennyson J, Polyansky OL, Kyuberis AA, Ovsyannikov RI, Zobov NF, Császár AG. The W2020 database of validated rovibrational experimental transitions and empirical energy levels of water isotopologues. II. $H_2{}^{17}O$ and $H_2{}^{18}O$ with an update to $H_2{}^{16}O$. J PhysChem Ref Data 2020;49:043103. https://doi.org/10.1063/5.0030680.

G

[Galanina2022] Galanina TA, Koroleva AO, Simonova AA, Campargue A, Tretyakov MYu. The water vapor self-continuum in the "terahertz gap" region (15–700cm^{-1}): Experiment versus MT_CKD-3.5 model. J Mol Spectrosc 2022;389:111691. https://doi.org/10.1016/j.jms.2022.111691.

[Gamache2019] Gamache R. Private communication, 2019.

[Gordon2017] Gordon IE, Rothman LS, Hill C, Kochanov RV, Tan Y, Bernath PF, et al. The HITRAN2016 molecular spectroscopic database. J Quant Spectrosc Radiat Transfer 2017;203:3–69. https://doi.org/10.1016/j.jqsrt.2017.06.038.

[Gordon2022] Gordon IE, Rothman LS, Hargreaves RJ, Hashemi R, Karlovets EV, Skinner FM, Conway EK, Hill C, Kochanov RV, Tan Y, Wcisło P, Finenko AA, Nelson K, Bernath PF, Birk M, Boudon V, Campargue A, Chance KV, Coustenis A, Drouin BJ, Flaud J-M, Gamache RR, Hodges JT, Jacquemart D, Mlaver EJ, Nikitin AV, Perevalov VI, Rotger M, Tennyson J, Toon GC, Tran H, TyuterevVlG, Adkins EM, Baker A, Barbe A, Canè E, Császár AG, Egorov O, Fleisher AJ, Fleurbaey H, Foltynowicz A, Furtenbacher T, Harrison JJ, Hartmann J-M, Horneman V-M, Huang X, Karman T, Karns J, Kassi S, Kleiner I, Kofman V, Kwabia-Tchana F, Lee TJ, Long DA, Lukashevskaya AA, Lyulin OM, MakhnevVYu, Matt W, Massie ST, Melosso M, Mikhailenko SN, Mondelain D, Müller HSP, Naumenko OV, Perrin A, Polyansky OL, Raddaoui E, Raston PL, Reed ZD, Rey M, Richard C, Tóbiás R, Sadiek I, Schwenke DW, Starikova E, Sung K, Tamassia F, Tashkun SA, Vander Auwera J, Vasilenko IA, Vigasin AA, Villanueva GL, Vispoel B, Wagner G, Yachmenev A, Yurchenko SN. The HITRAN2020 molecular spectroscopic database. J Quant Spectrosc Radiat Transf 2022;277:107949. https://doi.org/10.1016/j.jqsrt.2021.107949.

H

[Hartmann1993] Hartmann JM, Perrin MY, Ma Q, Tipping RH. The infrared continuum of pure water vapor: calculations and high-temperature measurements. J Quant Spectrosc Radiat Transf 1993;49:675. https://doi.org/10.1016/0022-4073(93)90010-F.

[Hartmann2008] Hartmann J-M, Boulet Ch, Robert D. Collisional effects on molecular spectra. Laboratory experiments and model. Consequences for applications. Amsterdam: Elsevier; 2008.

[Hartmann2021] Hartmann J-M, Boulet Ch, Robert D. Collisional effects on molecular spectra. Laboratory experiments and modelS. Consequences for applications. 2nd edition. Amsterdam: Elsevier; 2021.

[Hettner1918] Hettner G. Über das ultrarote Absorptionsspektrum des Wasserdampfes. Ann Phys 1918;360:476–96. doi:10.1002/andp.19183600603.

[Hirschfelder, 1954] Hirschfelder JO, Curtiss CH, Bird RB. Molecular theory of gases and liquids. 1954. NY: Jon Wiley & Sons, Inc.

[Horneman2005] Horneman VM, Anttila R, Alanko S, Pietilä J. Transferring calibration from CO_2 laser lines to far infrared water lines with the aid of the ν_2 band of OCS and the ν_2, ν_1-ν_2, and ν_1+ν_2 bands of $^{13}CS_2$: molecular constants of $^{13}CS_2$. J Mol Spectrosc 2005;234:238–54. doi:10.1016/j.jms.2005.09.011.

[Hu2001] Hu S-M, He S-G, Zheng J-J, Wang X-H, Ding Y, Zhu Q-S. High-resolution analysis of the ν_2+2ν_3 band of HDO. Chinese Physics 2001;10:1021-7. https://doi.org/10.1088/1009-1963/10/11/306.

I

J

[Johns1985] Johns JWC. High-resolution far infrared (20-350 cm^{-1}) spectra of several species of H_2O. J Opt Soc Am B 1985;2:1340–54. doi:10.1364/JOSAB.2.001340.

K

[Karman2015] Karman T, Milirdos E, Hunt K, Groenenboom GC, derAvoid Advan. Quantum mechanical calculation of the collision-induced absorption spectra of N2-N2 with anisotropic interactions. J Chem Phys 2015;142:084306. doi:10.1063/1.4907917.

[Kassi2012] Kassi, S, Campargue A. Cavity ring down spectroscopy with 5×10^{-13} cm^{-1} sensitivity. J Chem Phys 2012;137:234201, doi:10.1063/1.4769974.

[Kauppinen1978] Kauppinen J, Kärkkäinen T, Kyrö E. High-resolution spectrum of water vapor between 30 and 720 cm^{-1}. J Mol Spectrosc 1978;71:15–45. doi:10.1016/0022-2852(78)90073-5.

[Kauppinen1982] Kauppinen J, Jolma K, Hornaman VM. New wave-number calibration tables for H_2O, CO_2, and OCS lines between 500 and 900 cm^{-1}. Appl Opt 1982;21:3332–6. doi:10.1364/AO.21.003332.

[Klimeshina2013] Klimeshina TE, Rodimova OB. Temperature dependence of the water vapour continuum absorption in the 3–5μm spectral region. J Quant Spectrosc Radiat Transf 2013;119:77–83. doi:10.1016/j.jqsrt.2012.12.020.

[Kjaergaard2003] Kjaergaard HG, Robinson W, Howard DL, Daniel JS, Headrick JE, Vaida V. Complexes of importance to the absorption of solar radiation. J Phys Chem A 2003; 107:10680-10686. doi:10.1021/jp035098t.

[Kjaergaard2008] Kjaergaard HG, Garden AL, Chaban GM, Gerber RB, Matthews DA, Stanton JF. Calculation of vibrational transition frequencies and intensities in water dimer: comparison of different vibrational approaches. J Phys Chem A 2008;112:4324–35. doi:10.1021/jp710066f.

[Konefał2019]Konefał M, Mondelain D, Kassi S, Campargue A. High sensitivity spectroscopy of the O_2 band at 1.27 μm: (I) pure O_2 line parameters above 7920 cm^{-1}. J Quant Spectrosc Radiat Transf 2020;241:106653. doi:10.1016/j.jqsrt.2019.106653.

[Koroleva2021] Koroleva A.O., Odintsova T.A., Tretyakov M.Yu., Pirali O., Campargue A. The foreign-continuum absorption of water vapour in the far-infrared (50–500 cm−1). J Quant Spectrosc Radiat Transfer 2021; 261:107486. https://doi.org/10.1016/j.jqsrt.2020.107486.

[Koroleva2022] Koroleva AO, Kassi S, Campargue A. The water vapor self-continuum absorption at room temperature in the 1.25 μm window. J Quant Spectrosc Radiat Transf 2022;286:108206. doi:10.1016/j.jqsrt.2022.108206.

[Koroleva2023] Koroleva AO, Mikhailenko SN, Kassi S, Campargue A. Frequency comb-referenced cavity ring-down spectroscopy of natural water between 8041 and 8633 cm^{-1}// J Quant Spectrosc Radiat Transfer, 2023;298:108489. https://doi.org/10.1016/j.jqsrt.2023.108489.

[Koroleva2023II] Koroleva AO, Kassi S, Mondelain D, Campargue A. The water vapor foreign continuum in the 8100-8500 cm^{-1} spectral range. J Quant Spectrosc Radiat Transf 2023;296:108432. https://doi.org/10.1016/j.jqsrt.2022.108432.

[Koshelev2011] Koshelev MA, Serov EA, Parshin VV, Tretyakov MYu. Millimeter wave continuum absorption in moist nitrogen at temperatures 261–328K. J Quant Spectrosc Radiat Transfer 2011;112:2704–12. https://doi.org/10.1016/j.jqsrt.2011.08.004.

[Koshelev2018] Koshelev M.A., Leonov I.I., Serov E.A., Chernova A.I., Balashov AA, Bubnov G.M., Andriyanov A.F., Shkaev A.P., Parshin V.V., Krupnov A.F., Tretyakov M.Yu. New frontiers in modern resonator spectroscopy, 2018;8(6):773–783. doi:10.1109/TTHZ.2018.2875450.

[Krupnov2009] Krupnov AF, Tretyakov MYu, Leforestier C. Possibilities of observation of discrete spectrum of water dimer at equilibrium in millimeter-wave band. J Quant Spectrosc Radiat Transfer 2009;110:427—434.

[Kuhn2002] Kuhn T, Bauer A, Godon M, Buehler S, Kuenzi K. Water vapor continuum: absorption measurements at 350 GHz and model calculations. J Quant Spectrosc Radiat Transf 2002;74:545–62. https://doi.org/10.1016/S0022-4073(01)00271-0.

[Kuyanov-Prozument2010] Kuyanov-Prozument K, Choi MY, Vilesov AF. Spectrum and infrared intensities of OH-stretching bands of water dimers. J Chem Phys 2010;132:014304. https://doi.org/10.1063/1.3276459.

[Kyuberis2017] Kyuberis AA, Zobov NF, Naumenko OV, Voronin BA, Polyansky OL, Lodi L, Liu A, Hu S-M, Tennyson J. Room temperature line lists for deuterated water. J Quant Spectrosc Radiat Transf 2017;203:175-85. https://doi.org/10.1016/j.jqsrt.2017.06.026.

L

[Lechevallier2018] Lechevallier L, Vasilchenko S, Grilli R, Mondelain D, Romanini D, Campargue A. The water vapor self-continuum absorption in the infrared atmospheric windows: new laser measurements near 3.3 and 2.0 μm. Atmos Meas Tech 2018;11:2159–71. doi:10.5194/amt-11-2159-2018.

[Lee2008] Lee MS, Baletto F, Kanhere DG, Scandolo S, Far-infrared absorption of water clusters by first-principles molecular dynamics, J. Chem. Phys. 128 (2008), 214506. https://doi.org/10.1063/1.2933248.

[Leforestier2012] Leforestier C, Szalewicz K, van der Avoird A, Spectra of water dimer from a new ab initio potential with flexible monomers, J. Chem. Phys. 137 (2012), 014305. https://doi.org/10.1063/1.4722338.

[Leforestier2014] Leforestier C, Water dimer equilibrium constant calculation: A quantum formulation including metastable states. J Chem Phys 140 (2014), 074106. https://doi.org/10.1063/1.4865339.

[Liebe1987] Liebe HJ, Layton DH. Millimeter-wave properties of the atmosphere: laboratory studies and propagation modeling. NTIA Report. No. 87-224; 1987.

[Liu2006] Liu A-W, Hu S-M, Camy-Peyret C, Mandin J-Y, Naumenko O, Voronin B. Fourier transform absorption spectra of $H_2{}^{17}O$ and $H_2{}^{18}O$ in the 8000 – 9400 cm^{-1} spectral region. J Mol Spectrosc 2006;237:53-62. https://doi.org/10.1016/j.jms.2006.02.008.

[Lodi2012] Lodi L, Tennyson J. Line lists for $H_2{}^{18}O$ and $H_2{}^{17}O$ based on empirical line positions and *ab initio* intensities. J Quant Spectrosc Radiat Transf 2012;113:850-8. https://doi.org/10.1016/j.jqsrt.2012.02.023.

M

[Ma2008] Ma Q, Tipping R, Leforestier C. Temperature dependences of mechanisms responsible for the water-vapor continuum absorption. I. Far wings of allowed lines. J Chem Phys 2008;128:124313. doi:10.1063/1.2839604.

[Ma2014] Ma Q, Boulet C, Tipping RH. Effects on calculated half-widths and shifts from the line coupling for asymmetric-top molecules. J Chem Phys 2014;140:244301. http://dx.doi.org/10.1063/1.4883058.

[Mandin1988] Mandin J-Y, Chevillard J-P, Flaud J-M, Camy-Peyret C. $H_2{}^{16}O$: line positions and intensities between 8000 and 9500 cm^{-1}: the second hexad of interacting vibrational states {(050), (130), (031), (210), (111), (012)}. Can J Phys1988;66:997-1011. https://doi.org/10.1139/p88-162.

[Matsushima1995] Matsushima F, Odashima H, Iwasaki T, Tsunekawa S, Takagi K. Frequency measurement of pure rotational transition of H_2O from 0.5 to 5 THz. J Mol Struct 1995;352:371–8. doi:10.1016/0022-2860(94)08531-L.

[Matsushima2006] Matsushima F, Tomatsu N, Nagai T, Moriwaki Y, Takagi K. Frequency measurement of pure rotational transitions in the v_2=1 state of H_2O. J Mol Spectrosc 2006;235:190–5. doi:10.1016/j.jms.2005.11.003.

[Mendonca2019] Mendonca J, Strong K, Wunch D, Toon GC, Long DA, Hodges JT, et al. Using a speed-dependent Voigt line shape to retrieve O2 from total carbon column observing network solar spectra to improve measurements of XCO2. Atmos Meas Tech 2019;12:35–50. https://doi.org/10.5194/amt-12-35-2019.

[Meshkov2007] Meshkov AI, De Lucia FC. Laboratory measurements of dry air atmospheric absorption with a millimeter wave cavity ringdown spectrometer. J Quant Spectrosc Radiative Transfer 2007;108:256–76. doi:10.1016/j.jqsrt.2007.04.001.

[Mikhailenko2009] Mikhailenko SN, Tashkun SA, Putilova TA, Starikova EN, Daumont L, Jenouvrier A, Fally S, Carleer M, Hermans C, Vandaele AC. Critical evaluation of rotation-vibration transitions and an experimental dataset of energy levels of $HD^{18}O$.J Quant Spectrosc Radiat Transf 2009;110:597-608. https://doi.org/10.1016/j.jqsrt.2009.01.012.

[Mikhailenko2010] Mikhailenko SN, Tashkun SA, Daumont L, Jenouvrier A, Carleer M, Fally S, Vandaele AC. Line positions and energy levels of the 18-O substitutions from the HDO/D_2O spectra between 5600 and 8800 cm^{-1}. J Quant Spectrosc Radiat Transf 2010;111:2185-96. https://doi.org/10.1016/j.jqsrt.2010.01.028

[Mikhailenko2011] Mikhailenko S, Kassi S, Le Wang, Campargue A. The absorption spectrum of water in the 1.25μm transparency window (7408–7920 cm−1). J Mol Spectrosc 2011;269:92–103. doi:10.1016/j.jms.2011.05.005.

[Mikhailenko2020] Mikhailenko SN. Kassi S, Mondelain D, Campargue A. Water vapor absorption between 5690 and 8340 cm^{-1}: Accurate empirical line centers and validation tests of calculated line intensities. J Quant Spectrosc Radiat Transf 2020;245:106840. https://doi.org/10.1016/j.jqsrt.2020.106840.

[Mikhailenko2020II] Mikhailenko SN, Béguier S, Odintsova TA, TretyakovMYu, Pirali O, CampargueA. The far-infrared spectrum of ^{18}O enriched water vapour (40 – 700 cm^{-1}).J Quant Spectrosc Radiat Transf 2020;253:107105. https://doi.org/10.1016/j.jqsrt.2020.107105.

[Mlawer2012] Mlawer EJ, Payne VH, Moncet JL, Delamere JS, Alvarado MJ, Tobin DC. Development and recent evaluation of the MT-CKD model of continuum absorption. Philos Trans R Soc A Math Phys Eng Sci 2012;370:2520–56. doi:10.1098/rsta.2011.0295.

[Mlawer2023] Mlawer EJ, Cady-Pereira KE, Mascio J, Gordon IE. The inclusion of the MT_CKD water vapor continuum model in the HITRAN molecular spectroscopic database, J Quant Spectrosc Radiat Transf 2023; 306 :108645. https://doi.org/10.1016/j.jqsrt.2023.108645.

[Mondelain2013] Mondelain D, Aradj, Kassi S, Campargue A. The water vapour self-continuum by CRDS at room temperature in the 1.6 mm transparency window. J Quant Spectrosc Radiat Transf 2013;113:381–391. http://dx.doi.org/10.1016/j.jqsrt.2013.07.006.

[Mondelain2014] Mondelain D, Manigand S, Kassi S, and Campargue A. Temperature dependence of the water vapour self-continuum by cavity ring-down spectroscopy in the 1.6 μm transparency window. J Geophys Res Atmos 2015;17 17,762–17,770. doi:10.1039/c5cp01238d.

[Mondelain2015] Mondelain D, Vasilchenko S, Cermák P, Kassi S, Campargue A. The self- and foreign-absorption continua of water vapor by cavity ring-down spectroscopy near 2.35 μm. Phys Chem Chem Phys 2015;17 17,762–17,770. doi:10.1039/c5cp01238d.

[Mondelain2018] Mondelain D, Kassi S, Campargue A. Accurate laboratory measurement of the O_2 collision-induced absorption band near 1.27 μm. J Geophys Res Atmos 2018;124(1):414–23. doi:10.1029/2018JD029317.

[Mondelain2020] Mondelain D, Vasilchenko S, Kassi S, Campargue A. The water vapor foreigncontinuum in the 1.6 μm window by CRDS at room temperature. J Quant Spectrosc Radiat Transfer 2020;246:106923. doi:10.1016/j.jqsrt.2020.106923.

N

[Naumenko2004] Naumenko OV, Voronina S, Hu S-M. High resolution Fourier transform spectrum of HDO in the 7500 – 8200 cm^{-1} region: revisited. J Mol Spectrosc 2004;227:151-7. https://doi.org/10.1016/j.jms.2004.06.002.

[Ngo2013] Ngo NH, Tran H, Gamache RR, Bermejo D, Domenech J-L. Influence of velocity effects on the shape of N_2 (and air) broadened H2O lines revisited with classical molecular dynamics simulations. J Chem Phys 2012;137(6):064302. doi:10.1063/1.4739467.

O

[Odintsova2013] Odintsova TA, Tretyakov MYu, Evidence of true bound and metastable dimers and trimers presence in high temperature water vapor spectra. J Quant Spectrosc Rad Transf 120 (2013) 134–137. https://doi.org/10.1016/j.jqsrt.2013.01.015.

[Odintsova2017] Odintsova TA, Tretyakov MYu, Pirali O, Roy P. Water vapor continuum in the range of rotational spectrum of H2O molecule: new experimental data and their comparative analysis. J Quant Spectrosc Radiat Transf 2017;187:116–23. http://dx.doi.org/10.1016/j.jqsrt.2016.09.009.

[Odintsova2019] Odintsova TA, TretyakovMYu, Zibarova AO, Pirali O, Roy P, Campargue A. Far-infrared self-continuum absorption of $H_2{}^{16}O$ and $H_2{}^{18}O$ (15-500 cm^{-1}).J Quant SpectroscRadiatTransf2019;227:190-200. https://doi.org/10.1016/j.jqsrt.2019.02.012.

[Odintsova2020] Odintsova TA, Tretyakov MYu, Simonova A, Ptashnik I, Pirali O, Campargue A. Measurement and temperature dependence of the water vapor self-continuum in the 70–700 cm^{-1} range. J Mol Structure 2020;1210:128046. https://doi.org/10.1016/j.molstruc.2020.128046.

[Odintsova2022] Odintsova TA, Koroleva AO, Simonova AA, Campargue A, Tretyakov MYu. The atmospheric continuum in the “terahertz gap” region (15–700 cm− 1): Review of experiments at SOLEIL synchrotron and modeling. J Mol Spectrosc 2022;386:111603. https://doi.org/10.1016/j.jms.2022.111603.

[Ovsyannikov2023] Ovsyannikov RI, Tretyakov MYu, Koshelev MA, Galanina TA. On the uncertainty of the calculated intensities of the water vapor lines in the sub-THz frequency range. Atmospheric and oceanic optics 2023;36(7):1. https://doi.org/10.15372/AOO20230701.

[Oudot2010] Oudot C, Wang Le, Thomas X, Von der Heyden P, Daumont L, Régalia L. Intensity measurements of $H_2{}^{16}O$ lines in the spectral region 8000 – 9350 cm^{-1}. J MolSpectrosc2010;262:22-9. https://doi.org/10.1016/j.jms.2010.04.011.

P

[Partridge1997] Partridge H, Schwenke DW. The determination of an accurate isotope dependent potential energy surface for water from extensive *ab initio* calculations and experimental data. J Chem Phys 1997;106:4618–39. doi:10.1063/1.473987.

[Paso1995] Paso R, Horneman VM. High-resolution rotational absorption spectra of $H_2{}^{16}O$, $HD^{16}O$, and $D_2{}^{16}O$ between 110 and 500 cm^{-1}. J Opt Soc Am B 1995;12:1813–38. doi:10.1364/JOSAB.12.001813.

[Paynter2007] Paynter D, Ptashnik I, Shine K, Smith K. Pure water vapor continuum measurements between 3100 and 4400 cm^{-1}: evidence for water dimer absorption in near atmospheric conditions. Geophys Res Lett 2007;34:L12808. doi:10.1029/2007GL029259.

[Paynter2009] Paynter DJ, Ptashnik IV, Shine KP, Smith KM, McPheat R, and Williams RG. Laboratory measurements of the water vapor continuum in the 1200–8000 cm^{-1} region between 293 K and 351 K. J Geophys Res 2009;114:D21301. doi:10.1029/2008JD011355.

[Podobedov2008] Podobedov VB, Plusquellic DF, Siegrist KE, Fraser GT, Ma Q. Tipping RH. New measurements of the water vapor continuum in the region from 0.3 to 2.7 THz. J Quant Spectrosc Radiat Transfer 2008;109:458–67. https://doi.org/10.1016/j.jqsrt.2007.07.005.

[Podobedov2008II] Podobedov VB, Plusquellic DF, Siegrist KE, Fraser GT, Ma Q. Tipping RH. Continuum and magnetic dipole absorption of the water vapor—oxygen mixtures from 0.3 to 3.6 THz. J Mol Spectrosc 2008;251:203-209. https://doi.org/10.1016/j.jms.2008.02.021.

[Polyansky1996] Polyansky OL, Busler JR, Guo B, Zhang K, Bernath PF. The emission spectrum of hot water in the region between 370 and 930 cm^{-1}. J Mol Spectrosc 1996;176:305–15. doi:10.1006/jmsp.1996.0091.

[Polyansky1997] Polyansky OL, Tennyson J, Bernath PF. The spectrum of hot water: rotational transitions and difference bands in the (020), (100), and (001) vibrational states. J Mol Spectrosc 1997;186:213–21. doi:10.1006/jmsp.1997.7443.

[Polyansky1997II] Polyansky OL, Zobov NF, Viti S, Tennyson J, Bernath PF, Wallace L. Hightemperature rotational transitions of water in sunspot and laboratory spectra. J Mol Spectrosc 1997;186:422–47. doi:10.1006/jmsp.1997.7449.

[Polansky2012] Polyansky OL, Zobov NF, Mizus II, Lodi L, Yurchenko SN, Tennyson J, Császár AG and Boyarkin OV. Global spectroscopy of the water monomer. Phil Trans R Soc Lond A 2012; 370:2728-2748. doi:10.1098/rsta.2011.0259.

[Polyansky2018] Polyansky OL, Kyuberis AA, Zobov NF, Tennyson J, Yurchenko SN, Lodi L. ExoMol molecular line lists XXX: a complete high-accuracy line list for water. Mon Not R Astron Soc 2018;480:2597-608. https://doi.org/10.1093/mnras/sty1877.

[Ptashnik2004] Ptashnik I, Smith K, Shine K, Newnham D. Laboratory measurements of water vapor continuum absorption in spectral region 5000 –5600 cm^{-1}: evidence for water dimers. Q J R Meteorol Soc 2004;130:2391–408. doi:10.1256/qj.03.178.

[Ptashnik2008] Ptashnik IV. Evidence for the contribution of water dimers to the near-IR water vapor self-continuum. J Quant Spectrosc Radiat Transf 2008;109:831–52. doi:10.1016/j.jqsrt.2007.09.004.

[Ptashnik2011] Ptashnik IV, McPheat RA, Shine KP, Smith KM, Williams RG. Water vapor self continuum absorption in near-infrared windows derived from laboratory measurements. J Geophys Res 2011;116:D16305. doi:10.1029/2011JD015603.

[Ptashnik2011II] Ptashnik I, Shine KP, Vigasin AA. Water vapor self-continuum and water dimers: 1. Analysis of recent work. J Quant Spectrosc Radiat Transf 2011;112:1286–303. doi:10.1016/j.jqsrt.2011.01.012.

[Ptashnik2012] Ptashnik IV, McPheat RA, Shine KP, Smith KM, Williams RG. Water vapour foreign-continuum absorption in near-infrared windows from laboratory measurements. Philos Trans R Soc A Math Phys. Eng Sci 2012:370;2557–2577. doi:10.1098/rsta.2011.0218.

[Ptashnik2013] Ptashnik IV, Petrova TM, Ponomarev YN, Shine KP, Solodov AA, Solodov AM. Near-infrared water vapor self-continuum at close to room temperature. J Quant Spectrosc Radiat Transf 2013;120:23–35. doi:10.1016/j.jqsrt.2013.02.016.

[Ptashnik2015] Ptashnik IV, Petrova TM, Ponomarev YN, Solodov AA, Solodov AM. Water vapour continuum absorption in near-IR atmospheric windows. Atmos Oceanic Opt 2015;28:115–20. doi:10.1134/S102485601502009.

Q

R

[Régalia2014] Régalia L, Oudot C, Mikhailenko S, Wang L, Thomas X, Jenouvrier A, Von der Heyden P. Water vapor line parameters from 6450 to 9400 cm^{-1}. J Quant SpectroscRadiatTransf2014;136:119-36. https://doi.org/10.1016/j.jqsrt.2013.11.019.

[Richard2017]Richard L, Vasilchenko S, Mondelain D, Ventrillard I, Romanini D, Campargue A. Water vapor self-continuum absorption measurements in the 4.0 and 2.1 μm transparency windows. J Quant Spectrosc Radiat Transf 2017;201:171–9. doi:10.1016/j.jqsrt.2017.06.037.

[Reichert2007] Reichert L, Andres-Hernandez MD, Burrows JP, Tikhominov AB, et al. First CRDS measurements of water vapor continuum in the 940 nm absorption band. J Quant Spectrosc Radiat Transf 2007;105:303. https://doi.org/10.1016/j.jqsrt.2006.10.010.

[Robinson2003] Robinson TW, Kjaergaard HG. High level ab initio studies of the low-lying excited states in the H_2O–O_2 complex. J Chem Phys 2003;119:3717—3720. https://doi.org/10.1063/1.1591733.

[Rocher-Casterline2011] Rocher-Casterline BE, Ch'ng LC, Mollner AK, Reisler H. Determination of the bond dissociation energy (D0) of the water dimer, $(H_2O)_2$, by velocity map imaging. J Chem Phys 2011;134:211101. doi:10.1063/1.3598339.

[Rocher-Casterline2011II] Rocher-Casterline BE, Mollner AK, Ch'ng LC, Reisler H. Imaging H_2O photofragments in the predissociation of the HCl-H_2O hydrogen-bonded dimer, J. Phys. Chem. A. 115 (25) (2011) 6903–6909. https://doi.org/10.1021/jp112024s.

[Rodimova2018] Rodimova OB. Carbon dioxide and water vapor continuum absorption in the infrared spectral region. Atmos Ocean Opt 2018;31:564–9. doi:10.1134/S1024856018060143.

[Romanini1997] Romanini D, Kachanov AA, Sadeghi N, Stoeckel F. CW cavity ring down spectroscopy. Chem Phys Lett 1997; 264: 316–322. doi:10.1016/S0009-2614(96)01351-6.

[Romanini2014] Romanini D, Ventrillard I, Méjean G, Morville J, Kerstel E. Introduction to Cavity Enhanced Absorption Spectroscopy. Springer Series in Optical Sciences 2014;179: 1–60. doi:10.1007/978-3-642-40003-2-1.

S

[Salmi2008] Salmi T, Hänninen V, Garden AL, Kjaergaard HG, Tennyson J, Halonen L. Calculation of the O - H stretching vibrational overtone spectrum of the water dimer. J Phys Chem A 2008;112:6305–12. doi:10.1021/jp800754y.

[Scribano2006] Scribano Y, Goldman N, Saykally RJ, Leforestier C. Water dimers in the atmosphere III : equilibrium constant from a flexible potential. J Phys Chem A 2006;110:5411–19. doi:10.1021/jp056759k.

[Scribano2007] Scribano Y, Leforestier C. Contribution of water dimer absorption to the millimeter and far infrared atmospheric water continuum. J Chem Phys 2007;126:1–12. doi:10.1063/1.2746038.

[Schwenke2000] Schwenke DW, Partridge H. Convergence testing of the analytic representation of an *ab initio* dipole moment function for water: improved fitting yields improved intensities. J Chem Phys 2000;113:6592–7. doi:10.1063/1.1311392.

[Shine2012] Shine KP, Ptashnik IV, Rädel G. The water vapour continuum: brief history and recent developments. Surv Geophys 2012;33:535–55. doi:10.1007/s10712-011-9170-y.

[Simonova2020] Simonova AA, Ptashnik IV, Water vapor self-continuum model in the rotational absorption band. Proc. SPIE. 1156002 (2020) 1–7. https://doi.org/10.1117/12.2574937.

[Simonova2022] Simonova AA, Ptashnik IV, Elsey J, McPheat RA, Shine KP, Smith KM. Water vapor self-continuum in near-visible IR absorption bands: measurements and semiempirical model of water dimer absorption. J Quant Spectrosc Radiat Transf 2022;277:107957. doi:10.1016/j.jqsrt.2021.107957.

[Sironneau2015] Sironneau V.T., Hodges J.T. Line shapes, positions and intensities of water transitions near 1.28μm. J Quant Spectrosc Radiat Transf 2015;152:1–15. https://doi.org/10.1016/j.jqsrt.2014.10.020.

[Serov2014] Serov EA, Koshelev MA, Odintsova TA, Parshin VV, Tretyakov MYu. Rotationally resolved water dimer spectra in atmospheric air and pure water vapor in the 188–258 GHz range. Phys Chem Chem Phys 2014;16:26221. http://doi.org/10.1039/c4cp03252g.

[Serov2017] Serov EA, Odintsova TA, Tretyakov MYu, Semenov VE. On the origin of the water vapor continuum absorption within rotational and fundamental vibrational bands. J Quant Spectrosc Rad Transf 2017;193:1. https://doi.org/10.1016/j.jqsrt.2017.02.011.

[Slocum2015] Slocum DM, Giles RH, Goyette TM. High-resolution water vapor spectrum and line shape analysis in the terahertz region. J Quant Spectros Radiat Transfer 2015;159:69–79. https://doi.org/10.1016/j.jqsrt.2015.03.006.

[Stogryn1959] Stogryn DE, Hirschfelder JO. Contribution of bound, metastable, and free folecules to the second virial coefficient and some properties of double molecules. J Chem Phys 1959;31:6

[Svishchev1998] Svishchev IM, Boyd RJ. Van der Waals complexes of water with oxygen and nitrogen: Infrared spectra and atmospheric implications. J Phys Chem A 1998;102:7294—7296.

T

[Tennyson2010] Tennyson J, Bernath PF, Brown LR, Campargue A, Császár AG, Daumont L, Gamache RR, Hodges JT, Naumenko OV, Polyansky OL, Rothman LS, Toth RA, Vandaele AC, Zobov NF, Fally S, Fazliev AZ, Furtenbacher T, Gordon IE, Hu S-M, Mikhailenko SN, Voronin BA. IUPAC critical evaluation of the rotational-vibrational spectra of water vapor. Part II. Energy levels and transition wavenumbers for $HD^{16}O$, $HD^{17}O$, and $HD^{18}O$. J Quant SpectroscRadiatTransf 2010;111:2160-84. https://doi.org/10.1016/j.jqsrt.2010.06.012.

[Tennyson2013] Tennyson J, Bernath PF, Brown LR, Campargue A, Császár AG, Daumont L, Gamache RR, Hodges JT, Naumenko OV, Polyansky OL, Rothman LS, Vandaele AC, Zobov NF, Al Derzi AR, Fábri C, Fazliev AZ, Furtenbacher T, Gordon IE, Lodi L, Mizus II. IUPAC critical evaluation of the rotational-vibrational spectra of water vapor. Part III: Energy levels and transition wavenumbers for $H_2{}^{16}O$. J Quant Spectrosc Radiat Transf 2013;117:29-58. https://doi.org/10.1016/j.jqsrt.2012.10.002.

[Thalman2014] Thalman R, Zarzana K, Tolbert MA, Volkamer R. Rayleigh scattering cross-section measurements of nitrogen, argon, oxygen and air. J Quant Spectrosc Radiat Transf 2014;147:171–7. doi:10.1016/j.jqsrt.2014.05.030.

[Tikhomirov2006] Tikhomirov AB, Ptashnik IV, Tikhomirov BA. Measurements of the continuum absorption coefficient of water vapour near 14400 cm^{-1} (0.694 μm). Opt Spectrosc 2006;101:80. https://doi.org/10.1134/S0030400X06070150.

[Tipping1995] Tipping RH, Ma Q. Theory of the water vapor continuum and validations. Atmos Res 1995;36:69–94. doi:10.1016/0169-8095(94)00028-C.

[Tolchenov2005] Tolchenov RN, Tennyson J. Water line parameters for weak lines in the range 7400 – 9600 cm^{-1}. J MolSpectrosc2005;231:23-7. https://doi.org/10.1016/j.jms.2004.12.001.

[Toth1998] Toth RA. Water vapor measurements between 590 and 2582 cm-1: line positions and strengths. J Mol Spectrosc 1998;190:379–96. doi:10.1006/jmsp.1998.7611.

[Toureille2022] Toureille M, Koroleva AO, Mikhailenko SN, Pirali O, Campargue A. Water vapor absorption spectroscopy in the far-infrared (50-720 cm^{-1}). Part 1: Natural water. J Quant Spectrosc Radiat Transf 2022;291:108326. https://doi.org/10.1016/j.jqsrt.2022.108326.

[Tretyakov2011] Tretyakov MYu, Serov EA, Odintsova TA Equilibrium Thermodynamic State of Water Vapor and the Collisional Interaction of Molecules. Radiophysics and Quantum Electronics 2011; 54(10):700-716. doi:10.1007/s11141-012-9332-x.

[Tretyakov2012] Tretyakov MYu, Serov EA, Odintsova TA, Equilibrium thermodynamic state of water vapor and the collisional interaction of molecules, Radiophys. Quantum Electron. 54 (10) (2012) 700–716. https://doi.org/10.1007/s11141-012-9332-x.

[Tretyakov2013] Tretyakov MYu, Serov EA, Koshelev MA, Parshin VV, Krupnov AF. Water dimer rotationally resolved millimeter-wave spectrum observation at room temperature. Phys Rev Let 2013;110:093001. http://doi.org/10.1103/PhysRevLett.110093001.

[Tretyakov2018] Tretyakov MYu, Zibarova AO. On the problem of high-accuracy modeling of the dry air absorption spectrum in the millimeter wavelength range. J Quant Spectrosc Radiat Transf. 2018;216:70—75. https://doi.org/10.1016/j.jqsrt.2018.05.008.

[Tretyakov2022] Tretyakov My. High Accuracy Resonator Spectroscopy of Atmospheric Gases at Millimetre and Submillimetre Waves. Cambridge Scholars Publishing, 2022.

[Tvorogov1976] Tvorogov SD, Nesmelova LI. Radiation processes in band wings of atmospheric gases. Izv Ros Akad Nauk SSSR, Fiz Atmos Okeana 1976;12:627–33

U

V

[Vaida2000] Vaida V, Headrick JE. Physicochemical properties of hydrated complexes in the Earth's atmosphere. J Phys Chem A 2000;104(23):5401—5412.

[Van Vleck1945] Van Vleck JH, Weisskopf VF. On the shape of collision-broadened lines. Revs Modern Phys 1945;17:227—236.

[Van Vleck1977] Van Wleck JH, Huber DL. Absorption, emission, and linebreadths: A semihistorical perspective. Rev Mod Phys 1977 ;49(4):939—959.

[Vasilchenko2016] Development of an ultrasensitive cavity ring down spectrometer in the 2.10-2.35 μm region : application to water vapor and carbon dioxide. Instrumentation and Detectors[physics.ins-det]. Université Grenoble Alpes, 2017. English. ffNNT : 2017GREAY037ff. fftel-01704680ff.

[Vasilchenko2019] Vasilchenko S, Campargue A, Kassi S, Mondelain D. The water vapor self- and foreign-continua in the 1.6 μm and 2.3 μm windows by CRDS at room temperature. J Quant Spectrosc Radiat Transf 2019;227:230–8. doi:10.1016/j.jqsrt.2019.02.01.

[Ventrillard2015] Ventrillard I, Romanini D, Mondelain D, Campargue A. Accurate measurements and temperature dependence of the water vapor self-continuum absorption in the 2.1 μm atmospheric window. J Chem Phys 2015;143:134304. doi:10.1063/1.4931811.

[Vigasin1991] Vigasin AA. Bound, metastable and free states of bimolecular complexes. Infrared Phys 1991; 32:461-470. https://doi.org/10.1016/0020-0891(91)90135-3.

[Vigasin2010] Vigasin AA. On the possibility to quantify contributions from true bound and metastable pairs to infrared absorption in pressurised water vapour. Mol Phys 2010;108(18):2309–2313. https://doi.org/10.1080/00268971003781563.

[Vigasin2014] Vigasin AA. Water vapor continuum: Whether collisioninduced absorption is involved? J Quant Spectrosc Radiat Transfer 2014;148:58—64. https://doi.org/10.1016/j.jqsrt.2014.06.019.

[Vispoel2019] Vispoel B, Cavalcanti JH, Gamache RR. Modified complex Robert-Bonamy calculations of line shape parameters and their temperature dependence for water vapour in collision with N2. J Quant Spectrosc Radiat Transf 2019;228:79–89. https://doi.org/10.1016/j.jqsrt.2019.02.023.

[Vispoel2020] Vispoel B, Cavalcanti JH, Paige ET, Gamache RR. Vibrational dependence, temperature dependence, and prediction of line shape parameters for the H2ON2 collision system. J Quant Spectrosc Radiat Transf 2020;253:107030. doi:10.1016/j.jqsrt.2020.107030.

W

[Whitmore1980] Whitmore MD, Goodings DA. Calculation of second virial coefficients for nitrogen and carbon monoxide. Canadian Journal of Physics 1980; 58(6):820-827. doi:10.1139/p80-112.

X

Y

[Yu2012] Yu SS, Pearson JC, Drouin BJ, Martin-Drumel M-A, Pirali O, Vervloet M, et al. Measurement and analysis of new terahertz and far-infrared spectra of high temperature water. J Mol Spectrosc 2012;279:16–25. doi:10.1016/j.jms.2012.07.011.

Z

[Zobov2008] Zobov NF, Shirin SV, Ovsyannikov RI, Polyansky OL, Barber RJ, Tennyson J, Bernath PF, Carleer M, Colin R, Coheur P-F. Spectrum of hot water in the 4750–13 000 cm^{-1} wavenumber range (0.769 –2.1μm). Mon Not R Astron Soc 2008;387:1093–8. doi:10.1111/j.1365-2966.2008.13234.x.